Russian Chemical Reviews **71** (10) 789 – 835 (2002) © 2002 Russian Academy of Sciences and Turpion Ltd

DOI 10.1070/RC2002v071n10ABEH000743

Applications of NMR tomography to mass transfer studies

I V Koptyug, R Z Sagdeev

Contents

I.	Introduction	789
II.	Sorption into porous materials	789
III.	Swelling of polymers and coal during sorption of solvents	792
IV.	Drying	795
V.	Diffusion	798
VI.	Application of magnetic resonance imaging to flow studies	805
VII.	Supplement	816

Abstract. Modern physicochemical applications of NMR tomography, or magnetic resonance imaging (MRI), to the investigation of mass transfer processes are described. The mass transfer involved in the sorption of gases, fluids and solutes, swelling of polymers and coal and drying of various materials is considered. Various methods of studying isotropic, anisotropic and restricted diffusion in porous media are discussed. The approaches to the investigation of filtration and the flow of fluids, gases and granulated materials are presented. The bibliography includes 373 references.

I. Introduction

This review concerns a number of the most widely used modern physicochemical applications of the method of NMR tomography, or magnetic resonance imaging (MRI), which mainly concern the studies in the field of the transfer (transport, flow) of fluids, gases and granulated materials. The studies devoted to the obtaining of spectral data and the NMR experiments carried out without spatial resolution are covered fragmentarily. The exception are the investigations involving the use of the pulsed magnetic field gradients for studies of the spatial molecular displacements due to diffusion, to the flow of fluids and other types of motion. These communications were covered in the review because of their great value and also for yet another reason, namely, because the corresponding experiments are often considered as the MRI studies in the molecular displacement space rather than in the conventional coordinate space. The title field of research is so broad that the published data are covered only partially. The salient features of the MRI techniques and their applications to studies of liquid-containing materials have been reported in a recent review.[1]

I V Koptyug, R Z Sagdeev International Tomography Centre, Siberian Branch of the Russian Academy of Sciences, ul. Institutskaya 3A, 630090 Novosibirsk, Russian Federation. Fax (7-383) 233 13 99.
Tel. (7-383) 233 35 61. E-mail: koptyug@tomo.nsc.ru (I V Koptyug)
Tel. (7-383) 233 14 48. E-mail:itc@tomo.nsc.ru (R Z Sagdeev)

Received 20 June 2002
Uspekhi Khimii **71** (10) 899 – 949 (2002); translated by A M Raevsky

II. Sorption into porous materials

1. General remarks

Sorption has found a very broad spectrum of technological applications including, in particular, the drying and separation of chemical substances. Transport of fluids and gases through porous materials also plays an important role in catalysis. Permeability of building materials is critical to the development and use of engineering protective structures and containers for nuclear waste. Water and brine ingress into building materials can cause their accelerated degradation following different mechanisms including freezing, uptake of ions and corrosion and affects the gas permeability and thermal conductivity of materials.

The problem of how the structure of the pore space influences the transport processes in porous media is also topical. Application of the MRI technique to studies of this interrelation offers considerable prospects, since the method allows investigation of both structural and transport features for the same sample under the same conditions. Mass transfer can be strongly affected by not only microscopic inhomogeneities with the characteristic sizes lying in the pore size length scale, but also by macroscopic structural inhomogeneities inside porous materials including those due to specific features of the preparation procedure; therefore, MRI is widely used in the studies of transport processes.

Most modern building materials, as well as soil and many catalysts contain large amounts of paramagnetic ions, predominantly, Fe ions, which are responsible for appreciable shortening of the spin relaxation times of the fluids confined within the pores of such materials and for the appearance of local inhomogeneities of the magnetic field due to different magnetic susceptibilities of the chemical substances at the interfaces (if the experiments are carried out in strong magnetic fields). For instance, the T_2 time of water present in the fired-clay red brick containing a large amount of iron was found to lie between 180 and 360 μs.[2–4] Correspondingly, the MRI studies are often carried out in relatively weak fields ($< 1-2$ T) using strong amplitudes of the applied field gradients and appropriate experimental techniques that provide a short effective echo time.[5,6]

Large variations of the fluid content in the sample usually cause substantial changes in the relaxation times (see Section IV.2 in Ref. 1). Short T_2 times make a complete elimination of the relaxation weighting of MRI images virtually impossible; therefore, variations of the signal amplitudes are not in proportion to variations of the fluid content in the sample. In addition, adsorption can be accompanied by pronounced variation of the temper-

ature, which also affects the relaxation time values. Therefore, quantitative measurements require the use of some references and calibration curves.

Sorption of water usually causes large variations of the dielectric losses in the sample, while the presence of paramagnetic ions affects the electrical conductivity of the sample. This can be responsible for substantial variations of the sensitivity of the NMR spectrometer as a result of detuning the resonant circuit, which additionally complicates the quantitative interpretation of experimental data and in some instances makes it ambiguous due to nonmonotonic variation in the signal amplitudes upon a monotonic change in the water content.[7,8] For this reason, a number of experiments were carried out on a tailor-made instrument designed to study the processes accompanied by substantial variations of the water content in the samples.[3]

2. Sorption studies

Investigations of one-dimensional (1D) capillary sorption of water into different building material bars showed [9] that transport of water can be described using a nonlinear 1D diffusion equation in which the effective capillary diffusion coefficient, $D(C)$, depends on the water concentration, C. For gypsum and mortar bars [9] and for some limestone rock bars [9,10] the D value exponentially increases with the local concentration of water. Sorption of water into cylindrical hardened mortar samples [11] is described by an analogous equation with exponential dependence of D on C. Transfer of water in the sample dried at 105 °C was found to occur much faster than in the sample dried under milder conditions by extraction in isopropyl alcohol followed by drying at 40 °C. This can be due to the formation of a system of interconnected larger pores in the high-temperature drying. Shortening of the T_2 time of the adsorbed water in the region behind the adsorption front with time indicates a gradual redistribution of water from capillary pores into smaller gel pores that are formed around the cement grains upon hardening of the mortar.[11] Capillary sorption of water into different materials is characterised by the presence of a sharp front of water. In the case of 1D diffusion the front moves in proportion to the square root of time and the amount of the adsorbed water behaves analogously.[5,9–11] Adsorption of D_2O into samples with large initial water content was studied using the ^{2}D NMR signals.[5]

Often, the results of the sorption dynamics studies are presented as the $C = C(x/t^{1/2})$ dependence using the Boltzmann coordinate transformation. In these coordinates, *e.g.*, the 1D water distribution profiles obtained [2–4] for water in the fired-clay red brick at different times that passed after the beginning of the adsorption process fall on the same curve.[4] Numerical simulation of adsorption using the 1D diffusion equation and exponential dependence of D on the water content

$$D = D_0\exp(\beta C),$$

where β is the fitting parameter, led to good agreement between the calculated and experimental data.

Absorption of aqueous NaCl solution into a cylindrical calcium silicate sample was studied by simultaneously recording the 1D water distribution profiles and sodium concentration profiles.[12] Similarly to the data obtained for water, the sodium concentration profiles fall on the same curve in the $C(x/t^{1/2})$ coordinates. However, the system exhibits no sharp sodium concentration front. Virtually no sodium is present in the vicinity of the water front; sodium falls far short of the water front, being adsorbed into the pore space. It was recognised that the profiles obtained using the ^{23}Na NMR signals correspond to the sodium ions present in solution, whereas the concentration of the adsorbed sodium can be found from the adsorption isotherm measured in that study. The results obtained for sodium cannot be described by the diffusion equation in the $C(x/t^{1/2})$ coordinates even assuming that the equilibrium local concentration of the adsorbed sodium (determined from the adsorption isotherm) is reached following an exponential dependence some time after the beginning of the process rather than instantaneously. All calculations predict the presence of a more or less sharp sodium concentration front, which contradicts the experimental results.[12] Good agreement between the calculated and experimental data for water was obtained using an exponential dependence of D on C.

To reduce the water permeability of building materials, they are impregnated with some agents based on hydrophobic polymers and other compounds. An impregnation study of a hardened mortar sample with 5% solution of alkyltrialkoxysilane in methanol showed [6] that the impregnating agent penetrates only a short distance (1.5 mm from the surface). After drying the sample water poured on its surface did not penetrate the material, in contrast to non-impregnated blank sample. Water uptake by hardened cement samples containing both clay (sodium aluminosilicate, 2%) and polyvinyl alcohol (4%) additives was much smaller as compared to the samples containing only one additive.[13] This behaviour was explained by the formation of a hydrophobic material (as a result of cross-linking of the aluminosilicate particles and alcohol molecules), which fills the pores, thus preventing water ingress.

MRI allows visualisation of the spatial distribution of water and hydrocarbons in rock samples, which is necessary for the development of efficient procedures for improved petroleum recovery from petroleum pools based on the results of numerical simulation of the fluid diffusion in rocks (see also Section V). In particular, adsorption of water vapour into sandstone cores of various compositions, porosities and permeabilities has been studied.[14] The 1D water distribution profiles recorded at relatively low saturations allowed visualisation of the ingress of water vapour into the core through its open end. Simulation of the results obtained was carried out based on the assumption of simultaneous diffusion transport of water vapour and the adsorbed water with inclusion of the local equilibrium between them and led to good agreement between the calculated and experimental data. Assuming an exponential dependence of the vapour pressure on the concentration of the adsorbed water, it was found that D exponentially increases with an increase in the water content in the sample until the vapour filtration threshold is reached at times longer than 100 h. At even longer times, the distribution of water along the core axis became relatively homogeneous and varied only slightly upon further keeping the sample over a water bath, which was due to blocking of narrow inter-pore channels with the liquid that prevented free diffusion of vapour. Carrying out a series of experiments at different temperatures allowed the determination of the activation energy for surface diffusion.[14]

Selective water sorbents (SWS) [15–17] represent porous matrices impregnated with hygroscopic salts. The ability of such materials to efficiently absorb water vapour and alcohol vapours and release a great deal of energy offers considerable prospects for versatile applications of these materials, in particular, for dehumidification of gases, in heat pumps and in chemical heat accumulators. Adsorption of water vapours by individual $CaCl_2$-impregnated silica gel granules exposed to a humid air stream leads to the appearance of a sharp front of the adsorbed water inside the granule [7,8,18] (Fig. 1). Therefore, the presence of salt inside the millimetre-size granules makes capillary transport inefficient. The limiting stage of the process is transport of the adsorbed water into the interior of the granule. The results of numerical simulation of the process using the diffusion equation are in satisfactory agreement with the experimental data if one assumes an exponential increase in D with an increase in the water content.[8,18,19] The use of $CuCl_2$ allows one to follow the salt redistribution as a result of successive sorption – drying cycles for the granules prepared with inhomogeneous salt distribution.[7,18] Granules with large initial water content were characterised by the absence of a sharp water front during the adsorption process.[18]

Sorption of water vapour by a cylindrical pack of SWS granules exposed to a humid air stream has been studied.[7,8]

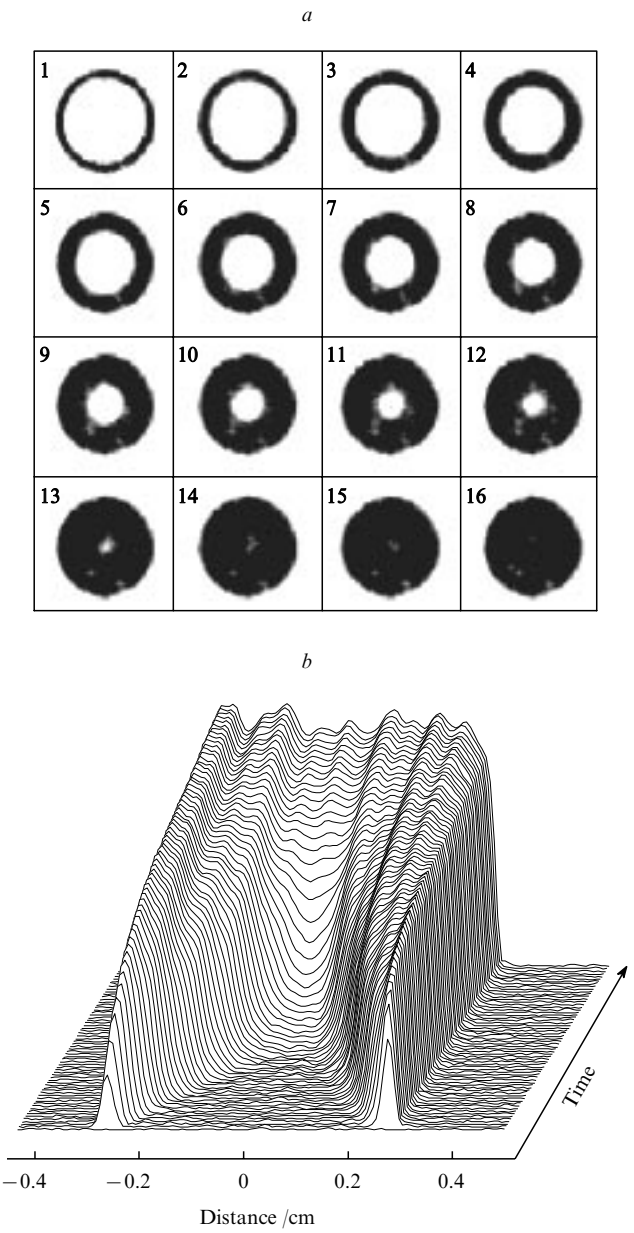


Figure 1. Visualisation of the adsorption of water vapours into a cylindrical silica gel granule impregnated with $CaCl_2$ (granule diameter: 6 mm).
Sixteen successively recorded two-dimensional images (acquisition time: ~15 min per image; the dark ring corresponds to the region containing the adsorbed water) (*a*); one-dimensional water distribution profiles along the diameter of the granule (acquisition time: 34 s per profile, the time taken to complete the experiment: nearly 5 h) (*b*).

Mention has been made that numerical simulation of the longitudinal movement of the sorbed water front requires the inclusion of (i) the effect of intragranular transport on the adsorption efficiency, (ii) flow dispersion effects in the porous medium and (iii) the character of the adsorption isotherm. Adsorption of water vapours by individual SWS granules and pellets and by SWS packs under vacuum has also been reported.[8,20] It was found that transport of adsorbed water under vacuum is, by and large, much more efficient; however, it is to a great extent determined by the granule (pellet) composition and morphology.

Interest in mass transfer in zeolites is due to the wide use of these materials in separation processes, drying and catalytic reactions. MRI was used for studying adsorption of different gases and vapours by zeolites. The movement of the adsorbed water front into the interior of the adsorbent (small crystals of zeolite 4A) has been studied in detail.[21,22] The shape of the front and the character of its movement were found to be strongly dependent on the relative efficiency of transport in the intercrystalline space and intracrystalline transport within the adsorbent layer. For tiny crystals (several micrometres in size) one can expect that the limiting stage of transport process is the diffusion of water vapour in the intercrystalline space, while the equilibrium between the adsorbate concentration in the crystal and the vapour pressure above the surface of the crystal is described by the adsorption isotherm. In this case the process can be described using one nonlinear diffusion equation while the diffusion coefficient, D, depends on the amount of the adsorbed water and is expressed by a combination of constant diffusion coefficients of the water vapour and adsorbate inside individual crystals. When exponential adsorption isotherm is used, the D value increases as the water content increases and can be represented as the sum of a constant and an exponential term.[21,23] Analogous experiments were carried out at different temperatures for two contacting layers comprised of 3 μm zeolite 4A granules with different initial water content.[23] Simulation of the results obtained showed that a decrease in the water content and an increase in temperature make the role of intragranular transport more significant. Equilibration of two contacting layers saturated with the light and heavy water occurs at a high vapour pressure and much faster, while the apparent (constant) diffusion coefficients of the adsorbed water and water vapour are somewhat higher than the corresponding values obtained in the equilibration experiments with a water-saturated layer contacting a dry layer. This difference becomes significant at higher temperatures and is probably due to the drawbacks of the mathematical model employed to describe the transport process. In particular, the intracrystalline vapour diffusion coefficient can also be strongly dependent on the vapour concentration. For instance, adsorption of n-hexane by a NaX zeolite layer is accompanied by a decrease in the intracrystalline diffusion coefficient with an increase in the adsorbed n-hexane.[24]

In the beginning of adsorption process the concentration of adsorbate in the surface layer rapidly reaches a maximum value, which is followed by the movement of the sharp concentration front into the interior of the adsorbent.[22] The concentration front is likely to move proportionally to the square root of time. In the later stages of the process the concentration front becomes somewhat diffuse and a wing appears in the region of low adsorbate concentration. The T_1 times obtained for water in the vicinity of and behind the adsorption front are different, which was associated with the changes in the mobility of water molecules that cannot be instantaneously located inside zeolite cavities.[22] The gradual movement of a sharp adsorption front was also observed in studies of the adsorption of water or butane vapours by a layer comprised of tiny crystals (4 μm in diameter) of zeolite NaX (Ref. 25) and of the adsorption of n-hexane vapours by zeolite NaX layer.[24,26] In contrast to this, experiments with zeolite NaX crystals 40 μm in diameter showed that intercrystalline transport is no longer the limiting factor and that butane remains uniformly distributed within the layer, whereas the overall amount of the adsorbed butane gradually increases.[25]

The MRI technique can be used for studies of adsorption from solutions. For instance, the chemical shift of 1,3,5-tri-*tert*-butylbenzene adsorbed on γ-Al_2O_3 differs from that of the bulk phase of 1,3,5-tri-*tert*-butylbenzene. This allowed the determination of the variation of the adsorbate concentration with time and estimation of the effective diffusion coefficient for a $CDCl_3$-filled granule from the NMR signal intensities.[27] Moreover, the chemical shift of the adsorbate can be pore size dependent. For instance, NMR studies of the samples of a carbon adsorbent characterised by a broad multimodal pore size distribution (from micropores to macropores) and saturated with solutions of acetonitrile, dichloromethane or benzene in CCl_4 revealed that the NMR spectra exhibit a superposition of several broad lines, each of them corresponding to the fluid confined inside pores of

different size. The chemical shift difference between the pore-confined and bulk-phase fluids varied from 1.4 ppm (large pores) to 9.6 ppm (small pores) for the three compounds studied. This indicates that the difference in the chemical shifts of the molecules inside pores of different size is due to different diamagnetic susceptibilities in the vicinity of the interfaces rather than donor–acceptor interactions. The 'dips' in the pore size distribution plot and slow inter-pore molecular exchange are two prerequisites for this conclusion. The linewidth is determined by intra-pore processes and is temperature independent in the range between 20 and 60 °C. From the surface areas of the signals in the NMR spectrum one can determine the fraction of the adsorbate inside the pores of different size (determination of absolute values requires the use of other measuring techniques). The method allows investigations of the role played by the pores of different size in the course of adsorption. As the adsorbate concentration increases from 0.2 to 1.2 mol litre^{-1}, the total amount of the adsorbate inside the micro- and mesopores is 'saturated', whereas the amount of the adsorbate in the large pores increases. Hence, preferred adsorption in micropores occurs initially. The T_1 and T_2 relaxation times of the peaks corresponding to different chemical shifts are also different. The T_2 times of the fluids confined in micropores remain constant as the adsorbate concentration varies, since the micropores are completely filled at a concentration of 0.2 mol litre^{-1}. At the same time, the T_2 times of the fluids confined in larger pores are lengthened as the concentration of adsorbate increases, since the fraction of the adsorbed molecules in these pores decreases. The amount of adsorbate in meso- and macropores increases with time, which is accompanied by displacement of the solvent molecules from the pores. The results obtained allowed construction of the isotherms of acetonitrile and benzene adsorption from CCl_4 separately for large, small and intermediate pores in the sample. Variation of the adsorbate concentration is accompanied by some variation of the chemical shifts of the NMR signals, which is consistent with their assignment to pores of different size.[28]

Transport of fluids in soil is critical to soil contamination studies. Equilibration of soil and water after placing a sample of dried soil (humus) in water has been studied over a period of 50 days.[27] 2D spin density maps and the T_2 time maps of water were obtained. The sample was found to be inhomogeneous and characterised by a bimodal T_2 distribution and by the shift of the short-T_2 mode towards the short-time region. This is probably due to either a gradual filling of micropores with water or to gelation.

III. Swelling of polymers and coal during sorption of solvents

1. General remarks

The interactions between polymers and fluids or gases accompanied by swelling and dissolution of the polymers are of great practical value for fabrication, processing and use of polymeric materials as well as in the physical chemistry of coal. Swelling of polymers is often accompanied by gelation.

The polymer–solvent systems can exhibit various types of mass transfer. If the rate of solvent diffusion into the polymer is much lower than the segmental relaxation rate of the polymer, the diffusive transport of the solvent is usually observed, which obeys Fick's laws (the so-called Case I transport). This type of transport is characterised by a gradual change in the solvent concentration along the direction of the solvent diffusion, movement of a diffuse solvent concentration front in proportion to the square root of time ($t^{1/2}$) and by nearly constant spin–spin relaxation time, T_2, of the solvent in the solvent-filled regions of the polymer. A quite different behaviour is characteristic of Case II transport, which occurs if the solvent diffusion rate is higher than the segmental relaxation rate of the polymer. In this case, a clearly visible front of the solvent permeating into the polymer is observed, the solvent concentration front moves linearly with time, the solvent concentration behind the front is constant and the T_2 time is shortened with the distance from the polymer surface contacting the solvent. The contour of the solvent front in 2D images matches that of the outer surface of the sample, through which the solvent ingress occurs, whereas in the case of Fickian transport the solvent contour acquires a circular shape after passage of a short time.

Fickian transport is usually observed in amorphous polymers characterised by the glass transition temperature lying below the temperature of the experiments. In contrast to this, realisation of Case II transport requires that the polymer be (initially) in the glassy state. Swelling of a polymer is usually accompanied by a decrease in the glass transition temperature, T_g, which can lead to transition of the polymer to the rubbery state. In addition to the two limiting cases, an intermediate type of transport (Case III transport) occurs. Often, the character of transport and its features can be revealed only using spatially resolved measurements.

Solvent transport into the interior of the polymer is often accompanied by cleavage of hydrogen bonds, weakening of other intermolecular interactions and by disentangling and moving apart the polymer chains. Infinite swelling leads to dissolution of the polymer.

Impregnation of polymeric materials with various solvents can be studied either by periodically interrupting the process to acquire MRI images or using real-time monitoring. The use of conventional techniques employed in the liquid-phase NMR allows selective monitoring of solvent transport,[29] whereas the signal of the solid matrix is often not observed due to short T_2 relaxation times. However, sometimes the mobility of the macromolecules becomes so high due to swelling that MRI imaging of the polymer is possible without using solid-state NMR techniques.[30,31] It should be noted that MRI allows one to obtain separate images of the solvent and the polymer, as well as the images of individual solvents if their mixtures are used in the experiments (see Section III.1 in Ref. 1). Swelling of polymers and coal in solvents occurs at relatively low rates; therefore, corresponding experiments may take times from tens of minutes to tens of days.

2. Swelling of polymers and coal

Periodic recording of the 1D acetone distributiion profiles in a vulcanised rubber sheet revealed[32] a Fickian transport of the liquid. The acetone front moves from the surface into the interior of the sample in proportion to the square root of time ($t^{1/2}$), since the glass transition temperature of the polymer under study is below the room temperature (the experiment was carried out at room temperature). Nevertheless, no substantial dispersion of the acetone front was observed, which indicated an (exponential) increase in the diffusion coefficient with an increase in the acetone concentration (C) in the polymer. Transport of boiling water in a nylon-6,6 block also obeys Fick's laws (the results obtained were described using an exponentially increasing dependence of D on C).[33] More recently,[34] transport of water in nylon-6,6 was studied at different temperatures between 20 and 100 °C; in this case, a linear dependence of D on C was used. The activation energy, E_a, for water diffusion in the polymer, extracted from the experimental data, was found to be 15 kcal mol^{-1}. This value is only slightly dependent on the water content. The temporal evolution of both the water distribution profiles and the spin relaxation times of water was described by the two-phase model, which implies the presence of two types of water molecules differing in degree of binding to the polymer. An increase in pressure caused an increase in both the diffusion coefficient and the maximum content of water in the polymer.[34]

Analysis of the 2D MRI images of radial transport of 1,4-dioxane in a poly(vinyl chloride) rod showed[35] that the system is characterised by Case II transport and the movement of the 1,4-dioxane front into the interior of the rod is proportional to $t^{0.91}$. At the same time, the swelling-induced variation of the rod diameter was proportional to $t^{1/2}$, since the increase in the volume occurs in the polymer region that is behind the liquid front and is

in the rubbery state for which transport of liquids obeys Fick's laws.[35] The solvent region behind the front is characterised by a constant spin density and by lengthening of the T_2 time with the distance from the surface. A more complex picture was observed for swelling of a bisphenol A polycarbonate rod in acetone. The movement of the solvent front was proportional to $t^{1/2}$, thus indicating Fickian transport. The solvent concentration decreased from the surface towards the core of the rod, while the T_2 time was nearly constant. At the same time, the 2D images exhibited a contracting, high-intensity ring-shaped zone of the NMR signal around the core; the concentration and the T_2 time (mobility) of the solvent inside this zone were higher than outside.[35] This was associated with crystallisation of the polymer, accompanied by the displacement of the solvent into the interior of the sample, which causes the solvent front to move in proportion to the square root of time. Crystallisation of the sample leads to the appearance of wedge-like cracks oriented from the surface into the interior of the cylinder; on further swelling, stress cracking is developed and the cracks become larger.

The butadiene rubber – toluene,[36] isobutyl rubber – toluene [37] and methylsiloxane rubber – hexafluorobenzene [36] systems exhibit Fickian transport while the poly(ethyl methacrylate) – methanol and bituminous coal – pyridine systems are characterised by Case II transport (a sharp solvent front is clearly visible in the corresponding 2D MRI images and moves at a constant velocity).[36, 37] It was found that, due to attenuation of the signals characterised by short T_2 times, the solvent front in the MRI images can appear to be sharper than that which actually exists.[36] A relatively simple model proposed for the description of the kinetics of the process couples the solvent diffusion and the polymer network relaxation upon transition from the glassy state to the rubbery state.[36] The experimentally measured solvent front velocities were used for calculations of the constant solvent diffusion coefficient in the glassy polymer and the polymer relaxation rate constant. The poly(methyl methacrylate) – methanol system exhibits Case II transport, which is probably due to the presence of the initial Fickian induction period.[38] The 2D images of poly(methyl methacrylate) rods partially saturated with deuteromethanol (CH_3OD) or acetone and the 2D maps of both the spin relaxation time distribution and the diffusion coefficient of the solvent were also obtained using the NMR signal of the solvent.[39] The presence of a sharp solvent front and a constant solvent concentration in the region behind the front are indicative of Case II transport. When moving from the glassy core into the interior of the swollen region, the T_1 and T_2 times and the diffusion coefficients of both solvents increase and then reach a plateau. This behaviour can be due to gradual increase in the polymer mobility along the polymer chain that is fastened at one end (in the glassy domain of the sample) and to the effect of the polymer mobility on the mobility of the solvent molecules. In practice, the behaviour of the system can strongly depend on the presence of residual amounts of the monomer or water in the polymer. For instance, an increase in the initial water content in poly(methyl methacrylate) increased the diffusion rate of methanol during the absorption process. If the water content exceeds 1 mass %, a passage from the Case II transport to Fickian transport of methanol occurs.[40] The absorption – desorption cycling of water and methanol followed by drying of the polymer also accelerate the diffusion of methanol in poly(methyl methacrylate) and the diffusion kinetics alters from Case II diffusion to Fickian diffusion. In all cases the initial period of absorption was characterised by a specific type of methanol diffusion, intermediate between the Fickian diffusion and Case II diffusion.[40]

Studies of the swelling of a poly(vinyl chloride) rod in toluene for 15 – 50 h revealed [41, 42] a sharp solvent front characteristic of Case II diffusion. The solvent front contour matched the cross-sectional shape (round or square) of the sample. When toluene penetrated into the rectangular rod through two oppositely lying surfaces, two parallel solvent fronts moved to meet each other.[42] At the same time the high-density polyethylene – n-pentane system exhibited a diffuse circular n-pentane front [41] typical of Fickian diffusion. The sample of stretched poly(vinyl chloride) used in yet another study [41] was prepared as follows. A poly(vinyl chloride) pipe was heated above the glass transition temperature of the polymer and expanded in a radial fashion. Then, slices were cut from the pipe, parallel to the pipe symmetry axis. Investigation [41] revealed strong anisotropy of solvent diffusion during the swelling process. In this case, the diffusion of toluene or trichloroethylene in the polymer occurred only in the direction corresponding to the radial direction for the initial pipe and was accompanied by elongation of the sample in the same direction and by contraction of the sample along the axis orthogonal to the direction of solvent diffusion. The anisotropy of the properties of the polymer was found to be hard to detect by high-resolution solid-state NMR techniques irrespective of the presence or absence of solvent in the sample.

Swelling of a copolymer of 2-hydroxyethyl methacrylate (HEMA) and tetrahydrofurfuryl methacrylate (THFMA) in water has been studied.[29] The diffusion coefficient of water (D_{H_2O}) in polyHEMA is $(1.5-2)\times10^{-7}$ cm^2 s^{-1}; in the copolymer the D_{H_2O} value decreases with an increase in the THFMA content due to the lower polarity of THFMA. The NMR images obtained revealed a Fickian diffusion and the peaks corresponding to increased content of water in the region between the diffusion front and the glassy core of the sample at the mole fractions of HEMA greater than 0.6. The peaks are thought to be due to the formation of small cracks appeared in peripheral regions of the glassy core owing to stress induced by swelling of the outer part of the sample; the cracks are filled with water. Further swelling of the polymer leads to closure of the cracks, while the region with the increased water content moves through the sample along with the diffusion front. As the diffusion front reaches the core of the sample, the peaks in the MRI images disappear along with the glassy core.

The character of diffusion for the same polymer – solvent pair can change appreciably with temperature. For instance, the diffusion of methanol in poly(methyl methacrylate) is Fickian at temperatures above 60 °C and Case II diffusion at temperature below 30 °C, whereas in the temperature range between 30 and 60 °C one can expect a combination of the two diffusion mechanisms.[43, 44] The character of diffusion can also strongly depend on the degree of cross-linking of the polymer. For instance, the diffusion of dioxane in a material prepared by polymerisation of styrene with divinylbenzene (DVB) additives can obey Fick's law (5% DVB), be Case II diffusion (1% DVB) or exhibit an intermediate diffusion type (2.5% DVB).[45] An increase in the degree of cross-linking of the polymer chains is accompanied by substantial reduction of the velocity of the movement of the dioxane front into the interior of the polymer sample.

Ageing of polymers strongly affects the diffusion processes. This was shown,[46] in particular, in the study of swelling of natural rubber exposed to high-temperature ageing at 170 °C in C_6D_6. At the ageing times of the order of 50 – 100 min, the diffusion and swelling rates in the surface layer, in which the ageing occurs most intensely, increase. At prolonged ageing, radical polymerisation in the presence of oxygen induces cross-linking of the polymer chains, which precludes the changes in the size of the sample due to swelling, but has no effect on diffusion. The anisotropy of the polymer structure strongly affects its swelling behaviour, *e.g.*, the change in the size of the sample.

Swelling of a polymer proceeds differently when a mixture of two or more liquids is used instead of the individual liquids. Swelling of a bisphenol A polycarbonate rod in a mixture of acetone and methanol (a good and a poor solvent for the rod material, respectively) has been studied using the difference between the chemical shifts of the solvents.[35] It was shown that the presence of methanol reduces the rate of acetone diffusion in the polymer, whereas the diffusion coefficient of methanol increases in the presence of acetone. Analogous studies of the diffusion of individual components of acetone – methanol mix-

tures with different component ratios were carried out using deuterated compounds.[47] A square-root-of-time dependence of the movement of the solvent front and a constant T_2 time of acetone in the region behind the solvent front were interpreted as manifestations of Fickian diffusion. In mixtures with the mole fraction of acetone being less than 50% both solvents diffuse with the same rate, whereas diffusion of acetone in the mixtures with higher content of this component occurs faster. Swelling of a cylindrical vulcanised rubber sample in an acetone–methanol mixture has been studied based on large difference between the chemical shifts of the mixture components.[48] It was found that both liquids diffuse in the mixture with the same rate equal to 80% and 250% of the diffusion rates of benzene and acetone, respectively, in the case of single-component impregnation. The creation and recording double-quantum coherence of the nuclear spins allowed one to follow isooctane diffusion in identical cylindrical sample impregnated with cyclohexane.[48] Swelling studies of cross-linked polystyrene in C_6F_6 revealed the presence of the absorption front. However, no clearly visible absorption front was observed for polystyrene initially saturated with C_6H_6; structural inhomogeneities favoured diffusion transport of liquid.[49]

A polymer gel based on poly(*N*-isopropylacrylamide) and H_2O/D_2O with CH_3OD additive, in which cross-linking of the polymer chains occurs in the presence of different amounts of *N*,*N*′-methylenebisacrylamide, is known to have the lower critical solution temperature.[46] As the temperature exceeds the critical value or as the concentration of the organic component of the solvent increases, the gel undergoes a transition from the swollen to the 'compressed' state. This behaviour can be used for fabrication of automatic chemomechanical valves. The 2D NMR images of a cylindrical sample revealed a decrease in the diameter of the sample with an increase in the temperature of water. The process was accompanied by the change in the T_2-contrast due to the variation of the mobility of the polymer and water molecules. Experiments with a D_2O-CH_3OD mixture showed that the initial stage of CH_3OD diffusion in the polymer gel obeyed Fick's laws. Since the degree of swelling of the polymer gel depends on the local component ratio in the solvent, this causes some changes in the polymer gel structure, followed by deviation of the diffusion mechanism from Fickian diffusion. Sometimes the formation of a surface layer was observed, which slowed down or precluded further ingress of the solvent into the polymer gel.

Not only the solvent behaviour, but also the changes in the properties of polymers have been studied. In particular, a study of the swelling of the peroxide vulcanised natural rubber in decane [21, 50] revealed a correlation between the T_2 time of the polymer and the local concentration of decane in the sample. An empirical relationship was suggested to describe the correlation. It was also found that the diffusion coefficient of decane exponentially increases as its local concentration increases. The study [51] of swelling of poly(ethylene oxide) in water showed that both diffusion of water in the swollen hydrogel and the swelling process are diffusion controlled and not accompanied by the change in the overall volume of the polymer and water. It was also found that monitoring simultaneous ingress of H_2O and D_2O into the polymer from the opposite ends of the sample allows one to observe the redistribution of the light and heavy water in the sample even after the two solvent fronts meet. The use of CD_2Cl_2 as solvent permitted the observation of the ^1H NMR signal of the polymer prepared by cross-linking the liquid-crystalline nematic prepolymer chains.[46] The ^1H NMR signal of the polymer was shown to increase with the degree of swelling of the sample. In this case, solvent diffusion along the polymer chains occurs much faster than lateral diffusion, the latter being jumpwise.

Sodium polyacrylate is a hydrophilic polymer capable of absorbing large amounts of water (several hundred times its own mass).[52] The 1D H_2O profiles obtained in the course of swelling of the polymer in water indicate a Fickian diffusion of water. Swelling was accompanied by shortening of the T_2 time of water due to gelation. By recording the NMR signal of the polymer it was shown that the swelling of the polymer followed by gelation occurred nearly two times faster than the movement of the water front into the interior of the polymer. It was found that distilled water diffuses faster than water containing salts and other impurities due to different chemical potential gradients.

Swelling of polymers occurs not only when the polymers contact liquids, but also when they are exposed to vapours. For instance, the ionic conductivity of polymer electrolytes $(Pb,Zn)(CF_3SO_3)_2(PEO)_n$ [PEO is poly(ethylene oxide)] is enhanced by several orders of magnitude upon adsorption of water vapours.[53] The 1D spin density and T_2 profiles for the adsorbed water and for the water-soaked polymer were obtained. In a number of experiments the contributions of water and polymer were separated using D_2O. The experiments confirmed that the adsorbed water exhibits a Fickian diffusion despite the presence of a sharp front. At the same time, the results obtained using the NMR signal of the polymer are quite different, namely, the signal amplitude is constant in the region behind the water front, while the T_2 time is shortened along the direction from the adsorbing face into the interior of the sample. The apparent velocity of the H_2O front movement was much higher than in the case of D_2O; this was explained by different dynamic properties of water and the polymer. An amorphous film with high content of poly(ethylene oxide) contained crystalline domains of the pure polymer with characteristic sizes from 500 to 800 μm. The 2D NMR images of the films totally exposed to water vapours showed that adsorption of water by the sample occurred due to the amorphous phase and caused a transition of the crystalline domains to the amorphous state.[53]

Similar discrepancies between the results obtained using the NMR signals of the solvent and polymer were also observed during adsorption of acetone vapours by poly(vinyl chloride) samples.[54] In this case, the solvent exhibited a Case II diffusion with a constant acetone concentration behind the liquid front; however, a 'Fickian precursor', that is, a long wing of low intensity and substantial extension into the interior of the polymer, was observed ahead of the solvent front. Variation of the signal behind the liquid front was rationalised by gradual softening of the swollen polymer. Another possible explanation is low segmental mobility of the polymer chain in the glassy region of the sample and gradual increase in this parameter with an increase in the depth of penetration into the rubbery swollen region.[39] The acetone and polymer signals were distinguished [54] using both deuterated acetone and the difference in the T_2 times. Despite the fact that the samples studied were synthesised in the United Kingdom while studied in Germany, it was stated that no errors were introduced. The charge carrier distribution in the polyelectrolyte-based electrochemical cells has been studied.[55]

Analysis of the profiles acquired using the NMR signals of polymers characterised by high segmental mobility [experiments on adsorption of the deuterochloroform or carbon tetrachloride vapours by poly(methyl methacrylate) or polystyrene bars] revealed [56] a Fickian diffusion in these systems. This conclusion is based on the assumption of proportionality of the local concentration of the mobile polymer to the local concentration of the adsorbed solvent. However, the T_1 profiles showed that the T_1 time of the polymer varies along the length of the sample even after establishment of homogeneous swelling after long-term impregnation with the liquid. This was interpreted as a consequence of the polymer mobility gradient.

Water diffusion is of great importance for food polymers since the presence of water affects the quality and the shelf life of food products. Studies of amylose pellets prepared from corn starch revealed [57] a Fickian diffusion of water in the sample exposed to water vapours and a Case II diffusion of water in the polymer sample contacting liquid water; in addition, polymer swelling in the latter case occurred much faster than in the former. The signal amplitudes were converted into actual water content using an empirical calibration relationship.

The 2D NMR images obtained in the course of swelling of bituminous coal in deuterated solvents (pyridine, acetone) exhibited [58] a gradual increase in the concentration of proton-containing substances in solution, which was attributed to the removal of loosely bound solvent molecules from coal. The NMR signal of protons inside the coal sample was detected only after 48 h monitoring, thus reflecting the appearance of mobile proton-containing components. A sample of another type of coal exhibited conventional swelling; however, only the NMR signal of the surrounding liquid was observed.[58]

In a number of studies the NMR images of polymers and coals partially saturated with a certain solvent were presented 'as is' without reporting the swelling dynamics data. Rod-like samples of bisphenol–acetone epoxy resin reinforced with a glass fibre swell in water at 93 °C in different manners depending on the character of the curing agent used in the sample preparation.[59] The difference is first of all due to the character of the microcracking of the sample. The distribution of water in the samples remains inhomogeneous even after swelling over a period of 90 days. The surface swelling occurs mainly in the vicinity of the glass fibre bundles.[59] The 2D images of the signal intensity and T_2 time distributions obtained for a rod-like sample of polybutadiene rubber completely saturated with 1,4-dioxane [60] revealed inhomogeneity of the polymer structure, which is due to, *e.g.*, poor mixing of the components or nonuniform heating in the course of the preparation and vulcanisation of the polymer. Saturation of a sample of natural rubber with hot water allowed visualisation of pores connected to the outer surface while the NMR images of a sample of vulcanised rubber completely saturated with cyclohexane allowed one to find the regions characterised by increased degree of cross-linking of the macromolecular chains.[61]

In spite of very broad NMR signals (300–800 Hz), the B_1-imaging technique [1] was successfully employed to acquire the 2D images of cellulose exposed to acetic acid vapours for 48 h and polystyrene swollen in liquid n-pentane for 72 h.[42] The images of coal samples swollen in acetone, DMSO or pyridine over a period of several hours allowed studies of the coal morphology and its changes caused by swelling.[62] It was found that permeation of solvents into coal was essentially inhomogeneous. The presence and arrangement of microcracks, cavities, mineral inclusions and other coal structure peculiarities was found using pyridine and pyridine-d_6.[63]

Studies of solvent desorption from a polymer are also of interest. If swelling of a polymer exhibits a Case II diffusion, one can expect a transition of the polymer from the rubbery state to the glassy state in the course of desorption, which must affect the efficiency of solvent transport. The dynamics of changes in the NMR images of a poly(methyl methacrylate) rod in cyclohexane-d_{12} at 30 °C (the sample was preliminarily kept in CH_3OD at the same temperature) has been studied.[64] During the first 60 min period the concentration of methanol in the surface layer of the sample substantially decreased and then varied only slightly over a period of 100 h. The results obtained suggested that the near-surface layer of the polymer undergoes a glass transition faster than other regions of the sample, which strongly hampers transport of the desorbing methanol.

Studies of infinite swelling resulting in dissolution of polymers are of interest from the standpoint of, *e.g.*, the development of controlled drug release systems based on dissolution of polymeric supports. For instance, water diffusion in a polyvinyl alcohol pellet (the molecular mass of the polymer lies between 35 740 and 133 000) causes a transition of the polymer to the rubbery state under normal conditions.[65] The 1D water content profiles exhibit a steep liquid front, thus indicating a relaxation-controlled (Case II) transport. For the rubbery domain, the water distribution profiles have a plateau and suggest a low diffusion resistance. As the molecular mass of the polymer increases, the diffusion rate decreases. Numerical simulation showed that the diffusion coefficient of water decreases with the distance from the pellet surface, since restricted mobility of the polymer chains in the vicinity of the glassy core hampers transport of water. As time passes, the diffusion coefficient in the vicinity of the pellet surface contacting the solid surface increases while remains constant near the free surface contacting the solvent.

A gel layer surrounding the pellet reduces the rates of dissolution and outward diffusion of drugs.[66, 67] Swelling of a hydroxypropylmethylcellulose (HPMC) pellet in water was characterised [66] by gradual permeation of water into the pellet and by swelling-induced movement of the interface. The penetration depth of water is a function of the square root of time, $t^{1/2}$. The T_2 relaxation times of water were converted into the 1D polymer concentration profiles along the direction of swelling using the results of NMR calibration experiments. After swelling for 37 h the pellets became four-fold thicker. The regions with the HPMC content greater than 30% remained solid; reduction of the HPMS fraction to 10%–30% was accompanied by gelation, while in the regions with the HPMC content less than 10% the polymer slowly dissolved and diffused into the bulk water phase.

Osmosis-based substance release mechanisms were found to act for water in a silicon matrix containing NH_4F.[68] In the presence of salt the T_1 and T_2 times of water are shortened and the ability of the cylindrical polymer sample to absorb water is enhanced considerably. Water diffusion in the matrix was accompanied by the formation of concentrated brine droplets that grew under the action of osmotic pressure. The process was monitored over a period of three months. The spatial distribution of water in a cylindrical sample containing 1% NH_4F was more or less homogeneous during the observation time. At 5% NH_4F, after swelling for seven days the content of water in the inner region of the sample was lower than in the outer region. After swelling for 35 days at the same concentration of NH_4F the content of water in the outer region of the sample decreased. This is due to the development of stress cracking in the matrix and to release of the content of brine 'pools'. Cracking of the sample was initiated at the surface and gradually moved into the interior.

Poly(hydroxyalkanoates) form a family of semicrystalline biopolymers. They are of interest because of biocompatibility and the ability to undergo biodegradation under the action of enzymes released by microorganisms. Enzymatic degradation of thin polymer films (0.2 mm) has been studied.[69] Since the crystalline domains do not contribute to the NMR signal, the signals observed in the experiments carried out at 50–60 °C after washing and drying the sample corresponded to the spin density in the amorphous domains. At the beginning of the process the content of amorphous polymer exponentially decreased and after some time became a linear function of time. In the deeper stages of the process enzymatic degradation of both the amorphous and the crystalline polymer occurred, which was confirmed by comparing the results of NMR imaging experiments and mass loss measurements.

IV. Drying

1. General remarks

Drying has found numerous technological applications. For instance, quality of cement and concrete articles depends on the water content in set and dried materials. Drying is used in film technologies (adhesives, binders, paints, coatings, *etc.*), synthesis of catalysts and treatment of food products and vegetable materials.

Violation of the drying regimes is often accompanied by deformation and cracking of articles and coatings. Because of this, the development of methods for controlling the water content in the samples in the course of the drying process is of great importance. MRI allows one to obtain necessary information and real-time monitoring makes it reliable.

The spin relaxation times of water in many porous materials are short due to the presence of paramagnetic impurities, reduction of molecular mobility owing to binding H_2O molecules and to the interactions of water molecules with the developed surface of

solids. This situation occurs, in particular, in the studies of cement and concrete. For instance, the relaxation times of hydrated white Portland cement are as follows: $T_2 = 320$ μs, $T_2^* = 170$ μs and $T_1 = 1.2$ ms.[70] Therefore, quantitative studies require the use of solid-state NMR techniques.[71–77] For instance, the use of strong gradients of the stray fields of a superconducting magnet in the STRAFI technique[1] allows the recording of the proton signals even for the hydrated and gel phases during hydration of cement.[78] The single-point imaging (SPI) technique is also promising,[1,70] though these methods do not allow the imaging of the whole amount of water in hydrates[78,79] [this water has a T_2^* time of 20 μs (Ref. 79)]. Samples tens or hundreds of micrometres thick are studied using the GARField device, which produces a homogeneous magnetic field in the plane of the sample and a strong static gradient in an orthogonal direction.[80,81] The advantage of the design is that the sample is placed on the surface of the probe rather than inside it.

It should be noted that the relaxation times are usually shortened as the water content decreases; therefore, the signal amplitude is not proportional to the actual water content in the sample. Often, the signal amplitudes are corrected using some calibrations obtained by independent methods of water content determination.[82] This allows one to exclude, in particular, the influence of other factors on the amplitude of the NMR signal. For instance, large variations of the water content in the sample cause detuning of the resonant circuit and change the sensitivity of the NMR probe.

2. Drying of materials and films

As mentioned above, MRI allows one to monitor the processes associated with the presence of water in cement, mortar and concrete. Hydration of cement during the first 48 h after the preparation of the cement paste has been studied by periodically recording the 1D water content profiles along the axis of the sample placed in a glass ampoule.[78] The experiments showed that water displaced from the bulk of the sample is present above the cement surface and the linear dimensions of the sample are reduced owing to shrinkage. The appearance of hydrates caused appreciable shortening of the T_2 time of a fraction of the H_2O molecules; therefore, even with an echo time of 30 μs the signal amplitude is attenuated and does not correspond to the actual content of water. Gypsum and lime additives cause a decrease in the degree of shrinkage of the samples and a faster attenuation of the signal amplitude.

The drying of cement[70,79,83] and concrete[79,83,84] after long-term moist curing has been studied. The samples were of different compositions and had different initial water content, the drying time being also different. During the first 24 h of drying, the water content in the sample decreased appreciably in the region near the open surface and to a lesser extent along the full length of the sample up to its closed end (due to capillary flow).[70] Capillary transport plays a more important role in the samples with high initial water content, since in this case the amount of hydrate formed is insufficient for filling the volume that was initially filled with water.[83] As the water-to-cement mass ratio decreased to 0.3–0.4, almost the whole amount of water was involved in the hydrate formation. For longer moist curing periods the porosity and permeability of the samples decreased, thus substantially reducing the efficiency of capillary transport of water in the course of drying.[79,83] In the deeper stages of the drying process, capillary transport of water changed to diffusion transport, which was accompanied by the movement of the drying front into the interior of the sample.[83,84] Compared to cement, the loss of water in concrete occurred faster in the early stages of the drying process, while in deeper stages the loss of water occurred more slowly. The presence of large aggregate particles in concrete prevented the material from cracking under the action of the surface tension forces due to the presence of the residual water in the pores of size 2.5 to 50 nm.

Interpretation and quantitative analysis of the data on the drying of cement and concrete first of all require detailed analysis of the relaxation behaviour of water in order to elucidate the correspondence between the NMR data and the actual water content in the sample. Probably, sometimes the signal amplitude reflects the distribution of only that fraction of water, which can be removed by drying,[79] and does not reflect the water in the gel pores.[84] For concrete samples moist cured for a long time (28 and 90 days), variation of the amplitude of the MRI profile was proportional to the change in the water content, whereas for the samples moist cured for no longer than 24 h this proportionality was observed only after drying over a period of a week.[79] This is probably due to the presence of at least three types of water molecules characterised by different (and variable) T_1 and T_2 times and, hence, by different (and variable) relative contributions. At the same time, in some instances the T_2^* time is independent of the water content, *i.e.*, the amplitude of the MRI profile is proportional to the water content.[70] When the T_1 times are analysed using the stretched exponent

$$M_z(t) = M_0\left\{1 - 2\exp\left[-\left(\frac{t}{T_1}\right)^{\alpha}\right]\right\} \quad (1)$$

(M_z is the longitudinal magnetisation of the nuclear spin system), the parameter α characterises the size distribution of the filled pores, which allowed the detection of the onset of microcracking 28–90 days after the beginning of the drying process.[83] The T_1, T_2 and T_2^* maps for mortar and partially dried concrete were obtained.[85]

Analysis of the 2D images and relaxation parameters of water in cylindrical samples of cement at low temperatures showed that the addition of superplastifier favours a decrease in porosity, reduction of the pore sizes and precludes the formation of macropores in which water freezes at relatively high temperatures.[86] The variation of T_1 [determined according to Eqn (1)] during the hydration process revealed that the addition of the superplastifier causes an increase in the setting time of cement and the rate of subsequent hydration. The fact that the parameter α reaches the maximum value at long times is thought to be associated with the formation of microcracks.

Drying of fired clay brick, lime-and-sand brick and gypsum by blowing air with a relative humidity of 45% (at 20 °C) over the open end of cylindrical samples has been studied by periodically recording the 1D water distribution profiles along the axis of the samples.[3,87] In all cases, a relatively homogeneous decrease in the water content along the full length of the sample was initially observed. As time passed (7 to 20 h), the drying front moving into the interior of the sample was observed. The gypsum and lime-and-sand brick samples exhibited a nonzero residual water content in the region behind the drying front. Transport processes were simulated using the diffusion equation, which allowed one to obtain the dependence of the effective diffusion coefficient on the water content for the materials under study. Namely, for all the samples the D value decreased with decreasing C (for C lying in the range from 5% to 20%), was minimum at $C = 2\%-5\%$ and increased again on further decreasing the water content. The last-named feature is associated with increasing importance of the diffusion transport of water vapour at low water content and with the presence of a plateau in the adsorption isotherm.[87] To obtain a more reliable $D(C)$ dependence in this range of water contents, the movement of the drying front was simulated using a constant velocity model. The velocity of the front movement was strongly dependent on the type of the material and inversely proportional to the length of the sample.

Drying of a cubic limestone block at 105 °C was studied by periodically interrupting the drying process to acquire the NMR images.[88] It was found that the completely dried block exhibits an NMR signal of unknown nature, which is characterised by rather long relaxation times ($T_1 = 300$ ms, $T_2 = 30$ ms). If the water content exceeds 15% of the maximum value, drying is accompa-

nied by a relatively homogeneous decrease in the water content in the entire block; at lower water content, the drying front moving into the interior of the sample was observed. In this stage, the water present in the sample was confined in a spherical 'pool' contracting in the course of the drying process.[88]

Drying of liquid-saturated porous cylindrical granules (Al_2O_3, SiO_2, TiO_2) by blowing dry air has been studied.[7,8,89,90] Due to the fact that the acquisition time of the 2D images was much longer than the complete drying time of the sample (< 1 h), attempts at obtaining time-resolved profiles for quantitative data analysis failed.[89] Recording the 1D water content profiles along the diameter of a cylindrical granule allowed substantial reduction of the time taken to complete a single experiment (0.5–1 min), thus providing a way of studying radial transport of liquid inside the granules in the course of the drying process.[7,90,91] A special series of experiments was carried out to plot a calibration curve relating the amplitude of the experimental profile to the actual water content. The results obtained and their numerical simulation[91,92] showed that in the early stages the drying process proceeds at a constant rate, the slow drying regime being maintained due to efficient capillary transport of the liquid inside the granule. This was confirmed by nearly homogeneous dehumidification of the sample. Only after removal of nearly the whole amount of water the drying rate decreases, which is accompanied by creation of strong water content gradients within the sample. The effective 'capillary diffusion' coefficient, D, depends on the concentration, C, of water in the sample and much exceeds the self-diffusion coefficient of water at high C. The $D(C)$ dependence is closely related to the pore size distribution and can exhibit local extrema against the trend towards decreasing D with a decrease in the water content for the samples with complex pore size distribution patterns (*e.g.*, bimodal). Experimentally, this manifests itself in nonmonotonic variation of the curvature of the water content profile during the drying process. The character of the profile transformations is related to the degree of homogeneity of the granules.[7] In particular, the granules having small pores in the near-surface region are characterised by higher water content near the surface in the course of the drying process compared to the interior of the granules, though evaporation of water occurs from the surface. Inhomogeneities inside the granules cause significant distortion of the shape of the profiles. Experiments with organic liquids (acetone, cyclohexane or benzene) showed that redistribution of the liquid due to capillary flow is much less efficient and the liquid content profiles acquired during the drying process have a clearly visible dome-like shape.[7,90]

Drying of the monolithic alumina catalysts saturated with water by passing a stream of dry air through their transport channels has been studied. The apparent uniform decrease in the water content along the length of the monolith is due to redistribution of water owing to the action of capillary forces.[7,8,93] A modified catalyst sample of identical shape, in which longitudinal transport of water in the transport channel walls was impossible, exhibited a decrease in the drying rate with the distance from the inlet flat wall of the monolith.[8,20] Slow drying of the monolithic catalyst in the absence of air circulation and adsorption-contact drying of a monolithic catalyst using fine-grained alumina or zeolite powders has also been studied.

A number of studies have been concerned with the drying of various water-saturated granular packs, such as glass bead packs (bead size: 0.3–1 mm),[94,95] sand packs (grain size: 50–100 μm), potato starch packs (granule size: 20–50 μm), silica gel packs (granule size: 40–60 μm)[95] by blowing the pack surface with dry air. The NMR images obtained exhibit inhomogeneous patterns of drying inside the packs.[94] Investigations of the effect of surface tension on the drying process were carried out with an aqueous detergent (sodium dodecylsulfate) solution.[95] The experimental results were discussed using a model, which included the diffusion transport of water and the influence of the capillary and gravity forces that play a significant role in the case of packs of larger particles.[95] Drying of (i) packs comprised of water-saturated

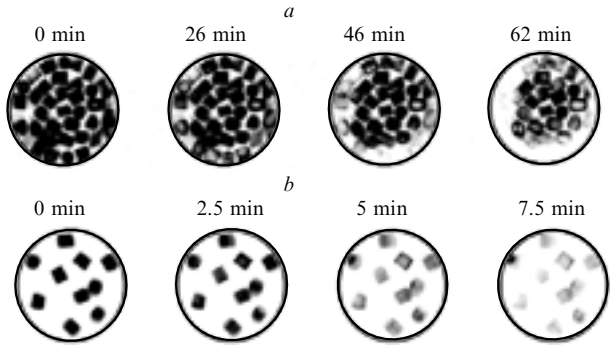


Figure 2. Two-dimensional MRI images obtained in the course of drying water-saturated alumina granules by blowing dry air through a cylindrical pack.
A pack of alumina granules 2.8 mm in diameter and 3.2 mm long (slice selective imaging technique; a slice 5 mm thick) (*a*); a pack comprising non-porous glass granules 2.4 mm in diameter and 2.2 mm long (invisible in the images) and a total of ten alumina granules (imaged without slice selection) (*b*).

porous alumina granules and (ii) mixed packs of non-porous and liquid-saturated porous granules[7,8] (Fig. 2) has been studied. These experiments allow studies of the details of mass transfer processes for grains located at different distances from the reactor walls.

A sample comprising a number of parallel, constant-diameter capillaries closed at one end is characterised by inefficient capillary transport. Exposure of the open end of a water-saturated sample to air stream led to establishment of fast drying regime, which was characterised by the movement of the sharp evaporation front along the capillaries towards the closed end.[7,96] The propagation of the evaporation front was proportional to the square root of time, while the estimate of the diffusion coefficient ($D = 0.24$ cm^2 s^{-1}) coincided with the diffusion coefficient of water vapour in air.

Evaporation of water from sodium silicate based films was studied by recording the 1D water content profiles in the direction normal to the film surface.[82] Experiments on drying of the films at 22–62 °C showed that water is faster removed from the near-surface region and that strong humidity gradients appear inside the films. Analysis of the T_2 distribution suggested a decrease in the molecular mobility in the course of the drying process, the molecular mobility at a particular water content being independent of the drying regime. Despite the introduction of corrections for short relaxation time, the hydration values calculated for the most dry films were found to be nearly twofold underestimated. Therefore, quantisation was performed using a calibration obtained by weighing the samples with homogeneous water content. The spatial resolution of the technique (100 μm) was determined by the accuracy of orientation of the film plane normal to the direction of the (static) magnetic field gradient and by the magnitude of stepwise displacement of the sample in the course of the measurements.

The deposition of solid colloidal particles onto a surface *via* the drying of waterborne dispersions is an important process in nature and in many technologies. Recently, this process has attracted increased interest due to ecological problems. The drying of thin colloidal films occurs in the horizontal direction. Changes in the water distribution in the films are accompanied by transport of the solute molecules. Horizontal drying of the dispersions of acrylic latex and polystyrene latex with systematic variation of the particle size, film thickness and evaporation rate has been studied.[97] For relatively large particles, low evaporation rates and small film thickness the film edges are not completely dried over a rather long time and the central region of the film remains more wet than the peripheral zones. Then, the drying

front comes into play, moving inward from periphery, the interface between the dry and wet regions being diffuse. Ahead of the drying front, a clearly visible particle-packing front moves. In the second limiting case, the drying and particle-packing fronts overlay and move inward from the periphery just after the beginning of the drying process.[97] If a droplet of aqueous dispersion of acrylic latex is dried by exposing to air stream, a 'skin' is formed on its surface.[98] The formation of a film upon simultaneous drying and photo-induced cross-linking of the aqueous dispersion of (vinyl acetate)-*co*-ethylene copolymer based latex indicates a complex picture of changes in the concentrations and molecular mobility with the thickness of the sample. This is due to different processes, such as diffusion of water, oxygen and cross-linking agent, transmission of light and free-radical polymerisation.[99]

Alkyd polymers prepared from natural substances (*e.g.*, fatty acids and oil) have found increasing use as paints. Unlike solid particles of colloidal dispersions, alkyd droplets are readily deformable in emulsion, which can affect the drying process. Therefore, drying of aqueous emulsions of an alkyd resin has been studied.[81,98] The difference between the chemical shifts of oil and water is sufficiently large to obtain separate NMR images.[1] It was shown that drying of a droplet deposited onto a solid surface and exposed to either stationary air or air stream was accompanied by a decrease in the size and thickness of the droplet.[98] The water loss rate was minimum at the edge and maximum at the centre of the droplet due to horizontal outward transport of water. The total amount of water decreased linearly with time over the whole observation time.[81,97] No increase in the alkyd resin concentration at the edge of the droplet was observed. The experimental data were compared with the results of model calculations. When the film was dried in stationary air, the film thickness linearly decreased with time during the fisrt 13 min.[81] The 1D T_2 distribution profiles obtained after 18 min exhibit a clearly visible near-surface layer, or a 'skin', characterised by much shorter T_2 time and by an increase in the thickness with time, while the underlying region of the film remains wet. The presence of a sharp interface indicates a strong dependence of the diffusion coefficient on the water content. After 190 min, the 'skin' extends throughout the full thickness of the film and the sample is characterised by one T_2 value.[81] In auto-oxidative cross-linking of an alkyd resin film in the presence of a cobalt catalyst, a decrease in the amount of solvent is accompanied by shortening of the T_2 time as a result of cross-linking.[80]

Drying of composite liquid packaging cardboard by exposing both surfaces to air flow (20.5 – 60 °C) has been studied.[100] The air flows were of different rates and humidities. The 1D water content, T_1 and T_2 profiles were acquired. Initially, the concentration of water in the two outer layers was higher than in the middle layer. During drying the profiles became narrower due to shrinkage of the cardboard sheet. Under faster drying conditions the water loss was predominantly from the near-surface regions, while with slower drying conditions the water loss occurred uniformly throughout all layers. Initially, the drying rate was nearly constant, and then decreased.

Knowledge of water distribution in wood is of great importance for wood-working industry. Drying of white oak lumber samples has been studied by periodically recording the cross-sectional 2D NMR images over a period of two weeks.[101] The drying rate was found to be strongly dependent on the thickness of the sample and on the orientation of the wood rays and the growth rings with respect to the outer surface. Water loss from the surface of the wood was accompanied by the formation of a more dry near-surface region and more wet inner region, while outward transport of water could occur through wood rays.[101] Polyexponential analysis of the spin relaxation times in different stages of the drying of cedar and fir samples allowed one to distinguish and follow the behaviour of different types of water molecules (water on the walls and inside the walls of the earlywood tracheids, latewood tracheids and wood rays) for the sap-wood and heartwood regions.[102] The T_2 time is determined by exchange of water molecules between the surface and the bulk water phase, and the experimental values were consistent with the cavity sizes typical of tracheids and wood rays. Acoustic drying of wood has also been studied.[103,104] The acoustic field was shown to induce a substantial redistribution of water in the sample, which favours water recession.

Drying of food products and vegetable materials has been studied. For instance, the cross-sectional 2D NMR images of a corn spadix exposed to air flow at 60 °C exhibited a decrease in the water content inside the corn grains and reduction of the grain sizes.[105] A drying study of individual grains has been reported.[106] Drying of textile articles provides an example of drying of synthetic fabrics.[107]

V. Diffusion

1. General remarks

NMR diffusion studies have been carried out for more than five decades.[108,109] One of the modern NMR applications, the multidimensional DOSY (diffusion ordered spectroscopy) technique, provides a tool for the analysis of the NMR spectra of complex mixtures based on the differences between the diffusion coefficients of different molecules, for estimation of the molecular sizes and for detection of molecular aggregates.[110–114] MRI also allows spatially resolved diffusion studies.

Recently, considerable attention has been given to investigations of restricted diffusion of fluids and gases in porous materials (in this case, the presence of some obstructions/barriers imposes restrictions on the molecular displacements and, in particular, diffusion transfer).[115,116] Observation of the diffusive motion of the molecules in a porous medium permits extraction of information on the structure of the pore space. Generally, the apparent diffusion coefficient of the molecules in the pore space, $D(\Delta)$, depends on the observation time, Δ. At short Δ, the $D(\Delta)$ value is independent of the morphology of the porous structure and is defined as follows[117–119]

$$\frac{D(\Delta)}{D_0} = 1 - \frac{4}{9\sqrt{\pi}} \frac{S}{V} \sqrt{D_0 \Delta} + O(D_0 \Delta) \,. \tag{2}$$

Thus, diffusion studies at short Δ allow the determination of the pore surface-to-volume ratio, S/V. In addition, in the limiting case ($\Delta \to 0$) the molecules have no time to 'sense' the presence of barriers (see below) and the measurements give the self-diffusion coefficients of fluids.

In the long-time limit ($\Delta \to \infty$), one gets

$$\lim_{\Delta \to \infty} \left[\frac{D(\Delta)}{D_0} \right] = \frac{1}{T} \,, \tag{3}$$

where T is the tortuosity factor of the pore space.[117,118] There are also some interpolation formulae,[117,120] which make it possible to calculate the $D(\Delta)/D_0$ ratio at intermediate Δ values in the range between ~ 0 and $\sim \infty$.

Determination of the tortuosity factor of the pore space from the asymptotic behaviour of the diffusion coefficient requires that the molecule migrate over a distance of the order of the characteristic inhomogeneity size in the sample during the observation time. At the same time, pore size distribution measurements based on the results of analysis of the spin relaxation behaviour of a fluid assume an insignificant role of the inter-pore migration of the molecules. As can be seen, the two types of measurements are in some sense mutually exclusive.[121] Gases usually diffuse much faster than fluids. Therefore, the short-time limit is hard to study for gases; however, the long-time limit can be investigated with ease.[122–124] This can be of use in, *e.g.*, the studies of the samples with extended structural inhomogeneities.

In studies of the properties of the pore space considerable advances can be achieved using an analogy between diffusion and hydrodynamic (or gasodynamic) dispersion of flow through a

porous medium (see Section VI.4), since the dispersion coefficient can be much larger than the effective diffusion coefficient.[125]

For the molecules in voids (in contrast to the interconnected pore space) the maximum migration length is limited to the void size and the product $D(\Delta)\Delta$ reaches a plateau while the $D(\Delta)$ coefficient tends to zero as Δ increases.[117, 126] This can be used for the determination of the characteristic volume of droplets, cells, *etc*., which imposes restrictions on the diffusion. At the same time, in contrast to relaxation porosimetry data (this technique is sensitive to the smallest characteristic size of essentially non-spherical pores, such as long cylinders and slits), the results of diffusion coefficient measurements obtained in the long-time limit depend on all characteristic pore sizes; therefore, it is not necessarily true that the asymptotic limit for $D(\Delta)$ is reached over the observation time [$\Delta < (3-5)T_1$].[127]

Multiple-quantum coherence (MQC) technique with $n > 1$ is known to be more sensitive to inhomogeneities of the magnetic field than the NMR signal ($n = 1$).[128, 129] This can be useful in measuring small diffusion coefficients. Intramolecular MQC can be created for both single quadrupolar nuclei[130] and for the system of interacting spins within the same molecule.[131] If the samples have strong NMR signals, the intermolecular MQC can be created using the nonlinear echo technique[132] based on the long-range intermolecular dipolar interaction between the nuclear spins, or the dipolar demagnetising field (DDF) technique. Experiments with a number of fluids showed[133] that for intermolecular multiple-quantum coherence one gets $D_{ap} \approx nD$, where D_{ap} is the apparent value (*cf*. $D_{ap} = n^2D$ for intramolecular n-quantum coherence).

The methods described below allow one to obtain information on the molecular diffusion over distances of the order of 0.1 μm, which is much better than the spatial resolution of the MRI technique. Thus, by considering the 'displacement space' it is possible to substantially improve the spatial resolution of the NMR experiments.[134]

2. Methods of diffusion studies

One approach to the investigation of diffusion processes with the NMR technique involves the use of the concentration gradient of tracers or labelled compounds. In the presence of stable radicals and paramagnetic metal ions the relaxation times of the fluid or gas molecules contacting the unpaired electron spin are shortened. Diamagnetic compounds containing different nuclei and their isotopes, including mixtures of proton-containing compounds and their deuterated analogues, are also used. These experiments are most often carried out using the spatially resolved NMR imaging techniques in order to follow the temporal and spatial redistribution of tracers and then to determine the diffusion coefficient using numerical simulation methods.

A simple 'null-point' technique[135, 136] proposed for the studies of diffusion of paramagnetic substances involves the observation of the displacement of the concentration front of the paramagnetic tracer over relatively short distances, with the concentration variation being small compared to the average tracer concentration in solution. This allows reduction of the time taken to measure the diffusion coefficients to tens of minutes instead of much longer time (*e.g*., several days) required when using the methods based on the recording of variations of the total concentration profiles with time. Experimentally, the 1D concentration profile is acquired some time after inversion of the equilibrium magnetisation. The delay time is chosen in such a way that the desired concentration of the paramagnetic tracer corresponded to the passage of the magnetisation through zero when the signal is acquired. After calculations of the absolute values of the signal the profile exhibits a clearly seen, sharp minimum corresponding to the position of a given concentration of the diffusing paramagnetic tracer. A 2D version of the technique was also proposed.[137]

MRI also allows diffusion studies without creating the gradient of the diffusing substance. In this case, selective inversion or saturation of the signal from a certain region of the sample can be used as 'marker'. If no convection occurs, the 'dip' in the signal amplitude curve is recovered as a result of diffusion and spin–lattice relaxation.

Diffusion displacements of various molecules can be studied using the well-known[109] pulsed magnetic field gradient NMR techniques (pulsed field gradient, or PFG, and pulsed gradient spin echo, or PGSE). By modifying the conventional echo pulse sequence and by using strong pulsed field gradient amplitudes (up to 2500–5000 G cm^{-1})[138, 139] one can measure the diffusion coefficients of the order of 10^{-10} cm^2 s^{-1}. The measurement error is usually 5% to 10% of the measured values and depends on many factors[140, 141] including finite duration of the gradient pulses[142–144] and gradient-induced eddy currents,[112, 145–147] local field gradients due to the presence of interfaces between materials with different magnetic susceptibilities,[148–151] convection,[147] temperature errors and radiation damping effects.[148] Thorough consideration of these factors allows[140] the experimental error to be reduced to less than 1%. Diffusion studies can also be carried out using (quasi-)static field gradients.

The PFG technique is based on analysis of the dependence of the spin-echo signal amplitude on the magnitude of the applied field gradient. For a system of immobile spins the dephasing of precession of the nuclear spins experiencing different magnetic fields is reversible. However, random molecular displacements in inhomogeneous magnetic fields lead to incomplete rephasing of the NMR signal when the spin echo signal is created. Currently, the pulse sequences employed in PFG experiments utilise a pair of gradient pulses applied to the spin system after the transverse magnetisation is created. The gradient pulses have the effective amplitudes $-g_i$ and g_i ($i = x, y, z$), the same duration δ and are delayed by the time Δ [if a 180°-radiofrequency (RF) pulse is applied between the gradient pulses in order to rephase the transverse magnetisation, the gradient pulses must be of the same sign]. In this case, the expression for the spin-echo signal amplitude derived in the short gradient pulse approximation assuming unrestricted diffusion has the form[109]

$$E(b) = \exp(-Db), \tag{4}$$

where

$$b = \gamma^2 g^2 \delta^2 \Delta_{ef} \tag{5}$$

(γ is the gyromagnetic ratio for the nuclei under study).

For the normal distribution of diffusive displacements one gets

$$\Delta_{ef} = \Delta - \frac{\delta}{3}. \tag{6}$$

Thus, the plot of the $-\ln[E(b)]$ dependence is a straight line with the slope D (see Ref. 109)

$$-\ln[E(b)] = Db. \tag{7}$$

Since varying the durations of the gradient pulses and delay times in the pulse sequence can affect the signal amplitude due to relaxation effects, the experiments usually involve variation of the gradient amplitudes g_i by using multiple repetition of the pulse sequence. Often, these measurements take a long time (see Section II.2 in Ref. 1); therefore, a number of fast techniques for diffusion studies have been developed.[123, 152] In the case of multicomponent solutions or mixtures the measurements can be performed for each component.

The experiment in question involves measurements of the projections of the molecular displacements on the direction of the field gradient. Often, diffusion is spatially anisotropic. The diffusion anisotropy can be detected by projecting the diffusion displacements on different spatial coordinates, which can be achieved by judicious choice of the direction of the field gradient. However, obtaining more detailed information on the diffusion anisotropy requires the determination of the 3×3-diffusion tensor rather than scalar D_i values ($i = x, y, z$). Different elements of the diffusion tensor (including off-diagonal elements) can be deter-

mined from a special-purpose experiment in which the gradient pulses are applied along different directions (i, j) and the scalars b_i are replaced by a tensor with the elements

$$b_{ij} = \gamma^2 g_i g_j \delta^2 \Delta_{ef}, \quad (8)$$

which determine the contribution of each element of the diffusion tensor D_{ij} to the signal attenuation.[152, 153] In principle, carrying out a total of six experiments with different orientations of the gradient vectors and one experiment without diffusion weighting (at $g = 0$) is sufficient for the determination of the elements of symmetrical diffusion tensor.

Sometimes, it is sufficient to know, *e.g.*, the spur of the anisotropic diffusion tensor, which is equivalent to the orientation average of the diffusion coefficient tensor. This can be achieved by performing one experiment with non-zero gradients (and one experiment with $g = 0$), in which the spin echo signal amplitude is proportional to the spur of the diffusion tensor.[154] However, the obtaining of an NMR image, in which the signal amplitude is proportional to any characteristic of the anisotropy of the diffusion tensor, *e.g.*, the dispersion and asymmetry coefficients (the second and the third moments, respectively), requires the same number of measurements (6 + 1) as that needed for the determination of all elements of the symmetrical diffusion tensor.[154]

Diffusion is strongly affected by the presence of impermeable barriers (pore walls) to molecular motions. In this case, the $E(b)$ dependence cannot be described by the simple expression (4) and can also be nonmonotonic. This makes it possible to use the NMR technique in studies of the morphology of the materials in which restricted diffusion occurs.

The effects accompanying diffusion between two impermeable barriers were described [155] using three characteristic sizes [characteristic diffusion length l_d, pore size l_p and the parameter $l_g = (D_0/\gamma g)^{1/3}$]. Three limiting cases were considered, where one size was much smaller than the other two sizes. Since at $l_d \ll l_p$ most of the molecules do not 'sense' the barriers, one can expect that the corresponding experiments must give a correct value of the self-diffusion coefficient of the fluid, D_0. However, the unrestricted diffusion regime can be attained only if the condition $l_d \ll l_g$ is simultaneously met. Then the spin-echo signal amplitude is given by expression (4). If $l_g \ll l_p$, l_d, a 'localised' diffusion regime is realised. In this case, the largest contribution to the observed NMR signal comes from the spins located in the near-wall region. In MRI, this leads to the so-called 'edge enhancement' effect and to a decrease in the observed D value. The third regime (at $l_p \ll l_g$, l_d) corresponds in MRI to the collapse of an image to a single-peak. Experimentally, the three regimes can be distinguished based on the shape of the $E(b)$ dependence. The first and second regimes were demonstrated taking the diffusion of water in a slit 160 μm wide between parallel glass plates (the slit is too wide to allow realisation of the third regime). The geometry of the experiment permits comparison of the results obtained for unrestricted and restricted diffusion by applying the field gradient parallel or normal to the plates.[155]

Consideration of molecular diffusion in a regular system of voids or in an interconnected pore system exhibits an analogy between the PFG NMR and diffraction in optics.[116, 134, 156, 157] As the observation time (Δ) passes, the diffusion-'diffraction' effects cause the appearance of extrema on the $E(q)$ dependence ($q = \gamma g \delta/2\pi$) for a void of diameter a. Positions of the minima are close to the integer values of the product aq, which can be used for estimating the pore size. The situation becomes more complicated in the case of non-spherical pores. Numerical experiments on the diffusion in a cylindrical pore at arbitrary orientation of the axis of the cylinder with respect to the direction of the field gradient show the presence of two systems of minima on the plot of the dependence of the echo amplitude on q. These minima correspond to the motion along and normal to the axis of the cylinder, their amplitudes increasing with the increase in the $D\Delta$ product.[158] In one limiting case (large molecular displacements and small q values) the effective diffusion coefficient, $D = D_{ef}$, equals $L^2/12\Delta$ and $R^2/4\Delta$ if the field gradient is applied along and normal to the axis of the cylinder, respectively (L is the length and R is the radius of the cylinder). In the small-displacement limit, the $E(q)$ dependence in the form

$$E(\mathbf{q},\Delta) = E_\Delta(\mathbf{q}) = \exp(-4\pi^2 q^2 D \Delta_{ef}) \quad (9)$$

is observed only at small q; at large q, the $E(q)$ dependence obeys a power law. An ensemble of randomly oriented non-spherical pores and the system of aligned pores are characterised by different functions $E(q)$. However, the pore orientation distribution and the pore size distribution can be distinguished only using a special-purpose experiment involving two successive 'scattering' acts, as was used in studies of the shape of the yeast cells.[159]

The effect of the pore space geometry is of particular interest when following the spin motion in interconnected pore systems.[125, 134, 160] For a regular system of pores interconnected by narrow channels the coherence effects are also manifested as extrema on the $E(q)$ plot in the $\Delta \to \infty$ limit. If the regularity of the pore space is not perfect, the $E(q)$ plot will exhibit a diffuse peak at $q \approx 1/b$ corresponding to the nearest environment, similarly to X-ray diffraction in liquids (b is the distance between the adjacent pores). The coherence effects are also substantially weakened due to orientational disordering of the pore necks; however, the effect of the structure of the pore system on the $E(q)$ dependence is still retained. Meeting the condition $2D_{ef}\Delta \approx b^2$ is optimal for obtaining information on the structure of the pore space. At $D_{ef}\Delta \gg a^2$ (a is the pore diameter) one can distinguish three regimes, *viz.*, $q \ll 1/b$, $q \sim 1/b$ and $q \sim 1/a$. The case $q \ll 1/b$ [initial portion of the $E(q)$ dependence] corresponds to large molecular displacements and allows the determination of the D_{ef} value, the D_{ef}/D_0 ratio tending to $1/T$ at $\Delta \to \infty$ (T is the tortuosity factor of the pore space). At $q \sim 1/b$, the $E(q)$ dependence for a regular pore structure exhibits a peak. This is true assuming equilibration of the situation inside the pore, when the characteristic time of migration over a distance of the order of the pore size is shorter than the characteristic time of inter-pore migration. At $q \sim 1/a$, the $E(q)$ dependence passes through a minimum, as in the case of isolated pores. At short diffusion times, Δ, the D value is independent of the morphology of the pore space, being determined by the S/V ratio for the pore space [see formula (2)].

Integration of the $E(q)$ dependence over q gives the probability for a particle to return to (or remain in) the vicinity of its initial position after a given diffusion time Δ.[144, 161] This parameter can be used in studies of the pore space in materials with the broad size distributions of pores and solid grains constituting the material. For instance, the studies of rock cores revealed a correlation between the above-mentioned probability and hydraulic permeability of the samples.

NMR imaging in the displacement space (q-space, in contrast to NMR imaging in the k-space, or coordinate space) allows one to obtain not only the averaged diffusion characteristics (*e.g.*, the diffusion coefficient), but also complete information on the molecular displacement distribution over the observation time. Diffusion displacements can be characterised by the function $P(\mathbf{r}|\mathbf{r}',\Delta)$, which represents the probability density for a molecule initially located at the point $\mathbf{r}$ to appear at the point $\mathbf{r}'$ after time Δ.[116, 141] The quantities measured in the NMR experiments are inevitably averaged over a large molecular ensemble present in the entire sample or in its macroscopic region. In addition, the $P(\mathbf{r}|\mathbf{r}',\Delta)$ parameter can vary in the microscopic length scale. Averaging of $P(\mathbf{r}|\mathbf{r}',\Delta)$ allows passage to the formalism of the averaged propagator $P(\mathbf{R},\Delta)$, which gives the probability density for a molecule to migrate (or to be displaced) over the distance $\mathbf{R} = \mathbf{r}' - \mathbf{r}$ over time Δ irrespective of its initial position $\mathbf{r}$. At long observation times, Δ, the propagator can be considered as the autocorrelation function of the molecular displacements [143, 156] or

as the autocorrelation function of the pore shape in the direction of the applied field gradient;[159, 162] this allows the determination of the pore size as the half-width of the $P(\mathbf{R},\Delta)$ peak, which describes the shape of the propagator as a function of $\mathbf{R}$.

The averaged propagator $P(\mathbf{R},\Delta)$ is often measured using the above-mentioned pulse sequence with two pulsed gradients. In this case, the spin-echo signal amplitude is represented as a function of the following parameter

$$\mathbf{q} = \frac{\gamma \mathbf{g}\delta}{2\pi}. \tag{10}$$

The vector $\mathbf{q}$ is analogous to the wave vector $\mathbf{k}$; however, the $\mathbf{q}$ space is the reciprocal of the displacement space $\mathbf{R}$ rather than the coordinate space $\mathbf{r}$. If the gradient pulses are short, the spin-echo amplitude $E(\mathbf{q},\Delta)$ and the averaged propagator are mutually conjugate:[116, 141, 163]

$$E(\mathbf{q},\Delta) = \int P(\mathbf{R},\Delta)\exp(i\,2\pi\mathbf{qR})\mathrm{d}\mathbf{R}, \tag{11}$$

$$P(\mathbf{R},\Delta) = \int E(\mathbf{q},\Delta)\exp(-i\,2\pi\mathbf{qR})\mathrm{d}\mathbf{q}. \tag{12}$$

In the new notations, expression (4), which holds for unrestricted diffusion, takes the form of Eqn (9). The corresponding propagator describes a Gaussian distribution of diffusive molecular displacements centred at $\mathbf{R} = 0$:

$$P(\mathbf{R},\Delta) = \frac{1}{\sqrt{4\pi D\Delta_{\mathrm{ef}}}}\exp\left(-\frac{R^2}{4D\Delta_{\mathrm{ef}}}\right). \tag{13}$$

q-Spectroscopy experiments involve multiple repetitions of the pulse sequence upon stepwise variation of the q parameter (as a rule, using a constant increment of the gradient amplitude). Some advanced techniques with variable q increment (in particular, this permits shortening of the measurement time) have also been developed.[164, 165]

Dynamic q-space NMR imaging allows the determination of the spatially resolved averaged propagator $P(\mathbf{r},\mathbf{R},\Delta)$ and extraction of information on the displacements $\mathbf{R}$ that can be much smaller than the spatial resolution of the imaging experiments. In dynamic NMR imaging the signal amplitude, $S(\mathbf{k},\mathbf{q})$, is experimentally measured as function of the $\mathbf{k}$ and $\mathbf{q}$ vectors at fixed Δ values

$$S(\mathbf{k},\mathbf{q},\Delta) = \int\int \rho(\mathbf{r})P(\mathbf{r},\mathbf{R},\Delta)\exp 2\pi i(\mathbf{kr} + \mathbf{qR})\mathrm{d}\mathbf{R}\mathrm{d}\mathbf{r}, \tag{14}$$

where $\rho(\mathbf{r})$ is the spatial distribution of the spin density.

The multidimensional Fourier transformation technique makes it possible to derive the averaged propagator $P(\mathbf{r},\mathbf{R},\Delta)$ as a function of the coordinate $\mathbf{r}$ and to separately measure the propagator for each pixel of the NMR image using the formula [116, 141]

$$\rho(\mathbf{r})P(\mathbf{r},\mathbf{R},\Delta) = \int\int S(\mathbf{k},\mathbf{q},\Delta)\exp(-2\pi i)(\mathbf{kr} + \mathbf{qR})\mathrm{d}\mathbf{q}\mathrm{d}\mathbf{k}. \tag{15}$$

Like usually, in this case the direction of the measured molecular displacement component is determined by the applied field gradient, *i.e.*, the $P(\mathbf{R}_i,\Delta)$ value is measured experimentally, where $\mathbf{R}_i$ is the projection of the displacement vector on the direction of the applied field gradient. However, independent stepwise variation of two or three orthogonal field gradients allows the determination of the probability $P(\mathbf{R},\Delta)$, where $\mathbf{R}$ is the displacement vector in the 2D or 3D space, though these experiments are time-consuming and, hence, rare.

The averaged propagator formalism is applicable to the description of the experiments with short gradient pulses. Experiments with the gradient pulses of arbitrary duration and shape can be described using the formalism which is not based on the averaged propagator and thus can also be applied to the description of non-Marcovian processes.[166]

The maximum observation time in the PFG NMR experiments is determined by the T_2 time or by a combination of the T_1 and T_2 times of the diffusing molecules. To increase the observation time, the stimulated echo sequence is often employed instead of the spin echo sequence, which makes it possible to extend the time Δ up to the times of the order of T_1 rather than T_2 or T_2^*. Experiments with inert gases can also be useful, since their spin relaxation times are much longer than those of fluids. However, the relaxation times can be substantially shortened upon pore filling with a fluid or a gas. The relaxation times also impose restrictions on the observation time in the experiments with the diffusion recovery of the NMR signal after local disturbance by the RF pulses. In the tracer concentration gradient experiments the observation time is limited to the time taken to equilibrate the tracer concentration over the sample. It should be noted that these types of experiments are inequivalent in the sense that the corresponding diffusion coefficients can be different since different measuring techniques are sensitive to the structure of the pore space in different length scales.[167]

Another approach to the description of displacements of molecules is to use the velocity autocorrelation function.[163] The frequency analysis of this function can be performed by judicious choice of the frequency spectrum for the time integral of the effective field gradient. A study of the gradient sequences that allow one to determine the spectral densities of the velocity autocorrelation function in the frequency range (ω) from10 Hz to 100 kHz has been reported.[163] The $D(\omega)$ coefficient of bulk water was shown to be constant in the frequency range studied (210 – 1670 Hz).

Due to a finite switch on – switch off time of the pulsed field gradients the molecular displacements are hard to measure at times of the order of 100 μs. In this case, the oscillating field gradients are sometimes employed.[168] A single field gradient pulse diffusion study technique based on the effects of long-range dipolar interaction in liquids has been proposed.[169] Diffusion and relaxation time studies (including spatially resolved ones) can also be carried out with the gradients of the radiofrequency field B_1 instead of the gradients of the static magnetic field B_0.[129, 170, 171]

As mentioned above, a feature of porous materials placed in a magnetic field is the appearance of internal field gradients due to the presence of interfaces with different magnetic susceptibilities. Diffusion in the presence of local field gradients also causes attenuation of the NMR signal; however, an increase in the observation time causes the signal amplitude to reach some constant level rather than to decrease down to zero. The characteristic time taken to reach the asymptotic limit is determined by the time of diffusive displacement of a molecule over a distance of the order of the pore size.[172] If the pore system exhibits a pore size distribution, the decay of the signal is characterised by a set of characteristic times. The inverse Laplace transform allows the determination of the characteristic decay times and the pore size distribution for the sample under study.[173]

3. Use of tracer concentration gradients

Diffusion in a cylindrical zirconia granule pre-saturated with water and placed in an ampoule with D_2O was studied [174] using the ^{1}H NMR signal of the 1D projections of the sample on the direction normal to the axis of the cylinder. The radial distribution of water was reconstructed using the Abel transform. The use of the 1D technique allowed the recording of a large number of profiles over the complete diffusion mixing time of two liquids. The effective diffusion coefficient and the tortuosity factor of the pore space ($T = 1.98$), which appeared to be close to the reciprocal of the sample porosity, were determined using numerical simulation of diffusion in a cylinder.

Diffusion of water in Laponite gel (synthetic smectic clay) was studied by recording the 1D profiles along the same axes of two cylindrical samples placed in contact through the flat walls to

initiate diffusion.[175] One of the two samples was prepared using heavy water (D_2O). Fitting of the experimental profiles was performed with inclusion of fast H/D exchange and corrected for the dependence of the NMR signal amplitude on the local light/heavy water ratio, which causes appreciable changes in the T_2-weighting degree of the NMR signal. The (macro)diffusion coefficient of light water (1.50×10^{-9} m^2 s^{-1}) was found to be close to the (micro)diffusion coefficient obtained using the PFG technique (1.75×10^{-9} m^2 s^{-1}); both values are only slightly smaller than the self-diffusion coefficient of bulk water (2.1×10^{-9} m^2 s^{-1}) under these conditions. This is thought to be due to the 'open' structure of the gel consisting of platelets.[175]

Fractal systems exhibit anomalous self-diffusion and the mean square of molecular displacements is time dependent

$$\langle r^2 \rangle \sim t^{2/d}. \quad (16)$$

For unrestricted diffusion, $d = 2$; visualisation of light water diffusion in the pores of a percolation model object pre-saturated with D_2O gave a d value of 2.6.[176]

Low-temperature conservation of *in vitro* grown living tissues requires the use of cryoprotective agents. Cryoprotective solutions are usually introduced at a low temperature to prevent the development of osmotic stress and to reduce the toxic action on the tissues. A study[177] of DMSO/D_2O mixture ingress into artificial dermal replacement saturated with H_2O revealed a decrease in the rate of water diffusion with an increase in the DMSO concentration due to the strong interaction between the DMSO and water molecules, which leads to higher ultimate (equilibrium) concentrations of H_2O. Analysis of the behaviour of two samples (one of them was freeze dried) showed that the presence of living cells causes acceleration of water diffusion due to osmosis effects. As the temperature decreases below room temperature, diffusion slows down. Permeation of aqueous solutions of three cryoprotective agents into a dechorionated fish embryo has also been studied.[178] Methanol was found in the embryo after 15 min, whereas no DMSO and propylene glycol were detected even after 2.5 h. It was concluded that the syncytial layer of yolk is impermeable for DMSO and propylene glycol and prevents them from being transferred into the interior of the embryo.

Measurements of the diffusion coefficients of copper ions or 4-amino-TEMPO† nitroxyl radical from aqueous solution into various gels along the axis of cylindrical samples have been reported.[135] Due to the more 'open' gel structure with larger pores, diffusion of copper ions in agarose gel ($D = 4.8 \times 10^{-10}$ m^2 s^{-1}) occurs faster than in acrylamide gel ($D = 3.3 \times 10^{-10}$ m^2 s^{-1}) and silica gel ($D = 3.5 \times 10^{-10}$ m^2 s^{-1}). The diffusion coefficients of nitroxyl radical in gels were found to be nearly 80% of the corresponding values for the copper ion due to the larger size of 4-amino-TEMPO. Diffusion of Fe(II) and Fe(III) ions in a cylindrical sample of agarose gel has been studied by simulating the 1D diffusion process and led to $D = 2.7 \times 10^{-10}$ m^2 s^{-1} for Fe(III) and $D = 3.3 \times 10^{-10}$ m^2 s^{-1} for Fe(II) at room temperature.[136] Radial diffusion of copper ions in a hollow cylinder made of polyacrylamide gel, whose cavity was filled with an aqueous $CuSO_4$ solution ($D = 3.5 \times 10^{-10}$ m^2 s^{-1}), has also been studied.[137] The acquisition time was less than 3 min per 2D NMR image, which is shorter than the time taken to move the diffusion front over a distance of the order of the characteristic spatial resolution achieved in the experiment (0.15–0.5 mm). Diffusion of Mn^{2+} ions from aqueous solution into agarose gel has been reported.[179] The radical 4-hydroxy-TEMPO was used[180] to investigate diffusion from aqueous solution into silk fibroin gel ($D = 8.1 \times 10^{-11}$ m^2 s^{-1}). The NMR images obtained were both T_1- and T_2-weighted;[1] because of this, an increase in the local concentration of the radical in gel initially caused an increase and then a decrease in the water signal amplitude.

Diffusion of paramagnetic tracers in liquid-saturated porous media has been studied[181] using a tailor-made cell with an impermeable horizontal barrier between two sand layers (grain size: 250 μm). In the first experiment the upper layer was saturated with an aqueous NaCl solution while the lower layer was saturated with the same solution to which $NiCl_2$ (5 mmol litre^{-1}) was added. The experiment started with removal of the partition and the 2D images were obtained by acquiring the NMR signal of water, which was directly proportional to the concentration of the Ni^{2+} ions in the concentration range studied (0–5 mmol litre^{-1}) due to judicious choice of the experimental parameters. In the second experiment the upper (lower) sand layer was saturated with aqueous KCl (NaCl) solution and the 1D fluid distribution profiles were obtained by directly acquiring the ^{23}Na NMR signal. The diffusion coefficients obtained after fitting the experimental data were 2.7×10^{-10} m^2 s^{-1} for Ni^{2+} and 1.04×10^{-9} m^2 s^{-1} for Na^+. The difference between these and actual values can be due to the effect of the Cl^- ions present in solution on the diffusion process. Despite the thin barrier (200 μm), the apparent diffusion coefficients for the lower layer were found to be substantially (by a factor of 3.5) overestimated due to a non-ideal contact between two sand layers.[181]

4. Diffusion studies without use of tracers

As mentioned above, an extensive literature has evolved, concerning the studies of fluid diffusion in various materials. Measurements of the D and S/V values for water diffusion in a glass bead pack,[160] of the D value and the pore space tortuosity factor for porous granules and catalyst powders[182–184] and of the temperature dependence of D for anions and cations diffusing in concentrated electrolyte solutions[185] can serve as examples of these studies. The diffusion coefficients of hexadecane in silica and of MgO/n-octanol paste have been measured.[186] The experiments aimed at investigating the effects of the local field gradients were carried out using a Fe_2O_3 powder additive to MgO/n-octanol paste. Studies of water and brine diffusion in carbonate and sandstone rock cores have been reported.[117, 121, 187] It was shown[117] that in the short-time limit ($\Delta \to 0$) the D value tends to the self-diffusion coefficient, D_0, of the bulk fluid. Measurements carried out at short Δ allowed the determination of the S/V ratio [formula (2)] and the surface relaxivity. At long Δ, the D/D_0 ratio decreases[117, 187] and tends to $1/T$; however, this limit was reached for none of the samples studied.[117] In some experiments, the expected monotonic decrease in D/D_0 with an increase in Δ was not observed at all.[121] Analysis of the relaxation data showed that the samples exhibiting an anomalous behaviour were characterised by a complex pore size distribution pattern. Macroscopic structural heterogeneities of the porous medium can strongly affect transport of fluids and, in particular, be responsible for an increase in the apparent tortuosity factor.[183]

For water in kraft cellulose[162] at short Δ the propagator has a Gaussian shape and allows the determination of the S/V ratio. For cellulose with a reduced water content the distance between the diffusion barriers estimated from the propagator peak width at long Δ was 7 μm. The possibility of separating the contributions of free diffusing water in the inter-fibre space and of restricted water diffusing inside the fibres was recognised. Experiments showed that intra-fibre diffusion of water is anisotropic. In particular, the D values of water in a three-layer composite cardboard sheet were found to be the same for all layers at different water contents; however, the diffusion coefficient along the direction parallel to the surface of the cardboard sheet is larger than in the cross fibre direction due to the corresponding fibre orientation.[100] Drying of cardboard is accompanied by demonstrated shrinkage (a decrease in the pore size) and the D value also decreases. Numerical simulation was based on the model which included an exchange between two ensembles of water molecules with different D. Experiments[147] with a celery stalk also demon-

† TEMPO — 2,2,6,6,-tetramethylpiperidine-1-oxyl, stable nitroxyl radical.

strated the anisotropy of water diffusion, especially in the vascular tissues. The measured D values were found to be 1.6×10^{-5} for longitudinal and 8.3×10^{-6} cm^2 s^{-1} for lateral diffusion. The experimental diffusion coefficient of water in a developing wheat grain is 8.3×10^{-6} cm^2 s^{-1}.[188]

The orientation of fibres in living tissues can be determined by, *e.g.*, measuring the diffusion tensor. Functional disorders are often accompanied by changes in the tissue structure, which is intimately related to the diffusion tensor.[189] For instance, a MRI evaluation of post-stroke patients by constructing the 3D diffusion tensor maps showed that the greatest changes in the diffusion tensor are observed for the white matter of human brain.

Measurements of the diffusion coefficient in voids can be used for sizing the droplets of the dispersed phase in emulsions.[190, 191] Though the inverse problem (reconstruction of the size distribution from the NMR data) belongs to the class of ill-posed problems, the use of regularisation methods provides a tool for solving this problem in the absence of *a priori* information on the type of the size distribution. By employing flow-compensated PFG NMR techniques one can determine the size of emulsion droplets under flow. Measuring the $E(q)$ dependence also permits calculations of the diffusion coefficients and size distribution of molecular aggregates (*e.g.*, micelles and phospholipid vesicles).[114] The contributions of the entire molecular aggregates, individual molecules in them and individual molecules in solution to the NMR signal can be separated based on the difference between their diffusion coefficients.

For a number of systems the $E(q)$ dependence exhibits extrema due to diffraction-like diffusion effects in the quasi-periodic porous systems. In particular, a coherent peak was observed for water in a polystyrene bead pack.[161, 192] The $E(q)$ curves obtained for suspensions of human erythrocytes with different hematocrit exhibited some features (extrema and shoulders) due to both intra- and intercellular diffraction-like diffusion effects.[193] Cell death during the freeze – thaw cycles leads to disappearance of these features. Position of the 'intracellular' peak depends on the rate of transmembrane water exchange between the cell and its environment, which was confirmed experimentally by varying the temperature and by adding a transmembrane exchange inhibitor. Application of the pulsed field gradients parallel or perpendicular to the external magnetic field led to observation of different $E(q)$ dependences. This suggested that the diffusion anisotropy in the samples, which were in equilibrium with dioxygen, is a result of alignment of erythrocytes in the magnetic field (7 T) due to the difference between the diamagnetic susceptibilities of the suspension and the erythrocytes bearing oxygen-containing hemoglobin. In this case, a disk-shaped erythrocyte is aligned in such a way that the axis of the disk is directed normal to the external magnetic field. The addition of $NaNO_2$ to the suspension is accompanied by transition of hemoglobin to the paramagnetic state, which causes alignment of the axis of erythrocyte along the magnetic field. This was indirectly confirmed by the change in the shape of the $E(q)$ dependence. This mechanism was assumed to be responsible for the effect of the magnetic field on the blood flow in living organisms. (The experiments were carried out at 25 °C.)

When studying diffusion in porous media, spin relaxation induced variations of the NMR signal cannot be correctly included by simply multiplying the signal amplitude by the corresponding coefficient because of the effects of coupled restricted diffusion and surface relaxation.[183, 194] In this case carrying out relaxation measurements allows a correct determination of the diffusion coefficients, relaxation times and the contributions of the components experiencing different environments.[195, 196] Such experiments have been performed for water in a glass bead pack [194] and other fluids, for plants [195, 196] and for the cat brain *in vivo*.[195] The authors of the last-mentioned study succeeded in separating the contributions of brain tissues and cerebrospinal fluid and in observing a decrease in the D value in an artificially created ischemic region.

Gas diffusion measurements have also been reported. For instance, the diffusion coefficient of a xenon – dioxygen mixture was determined by recording a time profile of the changes in the 1D signal projections after inversion of the magnetisation in a slice 12 – 24 mm thick oriented normal to the spatial coordinate of the 1D NMR image.[197] The diffusion coefficient of ^{3}He in a porous slice at a pressure of several atmospheres was determined in analogous experiments involving inversion or saturation of the signal followed by simulation of the results.[198, 199] The spin – lattice relaxation time, T_1, of the gas was calculated from the changes in the area under the curve of the 1D NMR signal profile.[198]

Diffusion of xenon from the bulk gas phase into an aerogel sample causes attenuation of the NMR signal from peripheral regions of the sample after selective inversion of the signal of the bulk Xe phase.[200] If the amplitude of the field gradients employed to obtain the image is increased, the signal of the bulk gas phase becomes weaker which allows the selective visualisation of the occluded xenon phase characterised by a relatively low diffusion rate.[201] The D values for the mixture of thermally polarised xenon with oxygen [202] and for hyperpolarised xenon [123, 202] were determined using the $E(q)$ dependences. Diffusion of thermally polarised xenon in a glass bead pack has been studied.[202] The diffusion coefficient of xenon decreases with the observation time (12.5 – 1000 ms) and reaches the asymptotic limit. Measurements of the asymptotic behaviour of D values in the long-time limit in the experiments with fluorinated gases permitted the determination of the tortuosity factor of the pore space for partially sintered Y-stabilised tetragonal zirconia polycrystals.[122]

Considerable attention has been given to diffusion of adsorbates in zeolites (*e.g.*, diffusion of water, acetone, isopropyl alcohol, propane and propene in the NaX and CsNaX zeolites,[203] diffusion of alkanes in NaCaA zeolites [139]) under different conditions.[115] Since zeolites are most often used in the form of fine crystalline powders, transport of adsorbate is affected by both intracrystallite molecular diffusion and diffusion in the intercrystallite space.

Diffusion of ethane adsorbed into NaX and NaCaA zeolite powders at different observation times, temperatures, average crystallite sizes and adsorbate concentrations has been studied.[204] The experimental conditions were chosen in such a way that the fraction, p, of the ethane molecules in the intercrystallite space was small. Therefore, at short observation times the diffusion (average) propagator had a Gaussian shape. At long observation times, when the average molecular displacement exceeds the crystallite size, the shape of the propagator depends on the ratio of D_1 and pD_2, where D_1 is the intracrystallite diffusion coefficient of ethane and D_2 is the diffusion coefficient of ethane in the intercrystallite space. A feature of the ethane – NaCaA zeolite system is equality of the D_1 and pD_2 values at 173 K. Since the parameter p exhibits the most pronounced temperature dependence, at lower temperatures the propagator is mainly determined by intracrystallite diffusion even at long observation times; in addition, the smaller the crystallite size, the narrower the propagator peak. At higher temperatures, the propagator exhibits a wing extended towards large molecular displacements (**R**), since a fraction of molecules has time to diffuse out of the crystallites. Therefore, the smaller the crystallite size, the broader the propagator peak. The average propagator observed on further extension of the observation time is due to exchange of the gas molecules between the inter- and intracrystallite space.

A study [205] of ethane diffusion in H-ZSM-5 zeolite powder and of methane and butane diffusion in silicalite crystals and ZSM-5 zeolite at 123 – 383 K (see Ref. 206) revealed a decrease in D with an increase in the observation time Δ.[205] The effect becomes less pronounced on raising the temperature and is virtually independent of the displacement **R** for methane at high temperatures. Variations of D on changes in the root-mean-square molecular displacements are due to the presence of intracrystallite barriers to diffusion (*e.g.*, intergrowth). The results obtained were

simulated using the Monte Carlo technique.[206] The limiting stage of diffusion of benzene adsorbed into loose or compressed zeolite H-ZSM-5 is intraparticle diffusion.[207] The D value was found to be 10^{-10} cm^2 s^{-1}. The effect of coke formation in zeolite on the diffusion process was also studied.

Nitrogen ($^{15}N_2$) diffusion in CaNaA and NaX zeolites at different pressures and temperatures has been reported.[124] Small crystallite sizes and large diffusion coefficient of the gas permit only the D value for large molecular displacements to be experimentally determined, thus allowing calculations of the D_2 value.

Many technological applications of zeolites involve multicomponent adsorption, which gives an impetus to research in the field of simultaneous diffusion of several adsorbates. For instance, diffusion of ethane–ethene mixture in zeolite NaX has been studied.[208] Compared to the single-component systems, the diffusion coefficient of ethane in the binary system becomes much smaller and approaches the diffusion coefficient of ethene, which was found to be nearly constant in the single-component and binary systems.

Reagent and product diffusion during catalytic conversion of cyclopropane into propene on zeolite NaX has been investigated.[209] In the binary system the diffusion coefficients of the two compounds were found to be equal and constant throughout the process, being coincided with the value obtained by extrapolating the results obtained when no reaction occurred. Catalytic conversion of ethene on silicalite or zeolite H-ZSM-5 was studied with CF_4 as an inert probe.[210] A three-fold decrease in the diffusion coefficient of CF_4 was observed after 240 min from the beginning of the reaction. No further decrease in D was detected; however, regions with different mobility of the probe molecules appeared in the sample. In was found that 'short' alkanes are mainly formed at 370 K, whereas aromatic compounds are mainly formed at 575 K. After conducting the reaction under the abovementioned conditions the D value of CF_4 changed by an order of magnitude. The same differences were also observed for the CF_4–hexane and CF_4–benzene systems in the same zeolites without carrying out the reaction.

Experiments with zeolite single crystals allow one to reveal correlations between different components of the diffusion tensor, associated with the structure of the zeolite cavities and transport channels. To this end, water diffusion in natural chabazite has been investigated.[138] Diffusion anisotropy studies can also be performed with powders; however, this requires simulation of the $E(q)$ dependence.

MRI allows the determination of the dimension of the space in which diffusion occurs. For instance, one-dimensional diffusion can be established even for a sample comprising randomly oriented crystallites. A diffusion study of ethane in large crystals of $AlPO_4$-5 molecular sieves has been reported.[211] The $AlPO_4$-5 crystals have a system of parallel cylindrical channels 7.3 Å in diameter and no interconnections. The mean square displacements depends on the square root of the observation time ($t^{1/2}$), which indicates a 'single-file' diffusion when the molecules cannot 'bypass' one another. At the same time, both 'single-file'[212] and unidirectional (rather than 'single-file') diffusion of methane in $AlPO_4$-5 were observed.[211] A continuous-flow generation system of hyperpolarised gas was employed in studies of xenon diffusion in the 1D channels of porous nanocrystallites.[213] The amplitude of the NMR signal acquired using the saturation–recovery technique was used as a direct measure of the average penetration depth of the xenon atoms in the interior of the crystallites. The time dependence of the NMR signal corresponded to 'single-file' diffusion. The advantage of the technique is the possibility of studying molecular displacements at times from hundreds of milliseconds to tens of seconds.

5. 'Edge enhancement' effect

One interesting and useful consequence of the attenuation of the NMR signal in the case of diffusion in inhomogeneous magnetic field is the so-called 'edge enhancement' effect. The molecules located in the vicinity of impermeable barriers migrate over shorter distances compared to the molecules present far from the barriers; therefore, they are less sensitive to signal attenuation, which is equivalent to extension of the decay time, T_2^* of the transverse magnetisation. As a result, the signal from the near-wall region will be more intense in the images. Indeed, reconstruction of the 2D diffusion coefficient maps of water and octanol in glass capillaries provided an experimental proof of the reduction of the diffusion coefficient of water in the near-wall layer up to 150 μm thick at an observation time of 0.8 s.[214] Often, reduced signal attenuation in the near-wall region compared to the bulk of the sample was experimentally observed in the diffusion-weighted NMR images of different dimension, *e.g.*, in the 1D and 2D images of water in glass capillaries 600 and 190 μm in diameter (see Ref. 215) and in the 1D images of water in a slit 2.6–2.8 mm wide.[216] The effect of the amplitude and duration of the gradient pulses[215] and of the observation time[216] on the 'edge enhancement' effect has been investigated. The characteristic range of the molecular displacements over the observation time under the experimental conditions was found to be 12–22 μm.[216]

Rather large diffusion coefficients of gases can cause significant distortions of the NMR images. The character of these distortions strongly depends on the sample size, the field gradient amplitude and the diffusion coefficient. The possibility of attenuation of the signal from the bulk gas phase compared to the signal of gas in the near-wall region was demonstrated in experiments with xenon.[217, 218] As the relative efficiency of diffusion increases due to decrease in the field gradient or reduction of the sample size, the near-boundary peaks are broadened, approach each other and then coalesce into one peak.[218] In this case, the MRI 'image' does not correspond to the spatial structure of the object under study. The experimental mean diffusive displacement of gas molecules in a rectangular ampoule differs from zero at the sample boundaries and is of different sign near the oppositely lying boundaries, while the root-mean-square diffusive displacement near the boundaries is smaller than inside the ampoule. Combining these effects and diffusion weighting provides a tool for implementation of selective edge imaging; however, a drawback of this technique is a substantial reduction of the signal-to-noise ratio. The edge distortion of the 1D NMR images of gas confined between impermeable parallel walls of a rectangular ampoule has also been observed in the experiments with hyperpolarised ^{3}He.[199, 219] Possible reasons for distortion of the NMR images include the 'edge enhancement' effect and the magnetic field disturbance near the tube walls due to different diamagnetic susceptibilities of materials. In the case of hyperpolarised gas, the long-range dipolar demagnetising field produced by the spin ensemble at the location of an individual spin also causes the 'edge enhancement' effect.[219] Helium also exhibits a lower diffusion coefficient in the vicinity of the tube walls;[199] however, this was thought to be unrelated to the restricted diffusion mechanism, since the diffusive displacement over the measuring time (0.1 mm) is much smaller than the spatial resolution achieved in the experiment (0.8 mm).

On the one hand, the 'edge enhancement' effect can find some useful applications in, *e.g.*, the experiments involving selective NMR spectroscopy of the near-wall regions,[215] enhancing the NMR signal in the regions of impermeable boundaries and revealing partitions that would be invisible otherwise.[220] On the other hand, this effect can cause significant distortions of the NMR images of microscopic objects. Broadening of spectral lines due to fast near-wall relaxation and partial penetrability of the barriers can suppress this effect.[220]

The 'edge enhancement' effect on the 1D, 2D and 3D images in linear and spherical geometries has also been the subject of theoretical studies.[220] Calculations for objects with a characteristic size of 40 μm showed that an increase in the diffusion coefficient causes averaging of the 'edge enhancement' effect due to faster molecular motions and leads to the appearance of a single peak with the maximum at the centre of the model object.

Calculations for two hollow spheres filled with water (one sphere was placed inside the other) showed that the 'edge enhancement' is observed only inside each sphere but not at the outer surface of the smaller sphere.[220]

An expression for the description of the 'edge enhancement' at an arbitrary shape and duration of the pulsed field gradients has been derived.[216] The echo amplitude was expressed through the molecular motion correlation function while the inhomogeneous spatial distribution of the magnetisation phase was expanded into a plane-wave series. In this approach incoherent molecular displacements cause a discord of plane waves, thus leading to improvement of the signal-to-noise ratio in the near-wall region. The maximum signal amplitude (or minimal root-mean-square molecular displacement) is observed at some distance from the walls rather than in the immediate vicinity of the walls. This distance, as well as the width of the peak, is independent of the amplitude of the applied field gradient but increases with the observation time. The Monte Carlo simulations lead to 'sharper' near-wall peaks compared to those observed in the experiments.[215]

VI. Application of magnetic resonance imaging to flow studies

1. General remarks

This Section concerns flow studies including filtration; however, one should keep in mind that the experimental methods considered here also allow investigation of other types of motion, *e.g.*, a translational or rotational motion of the entire body, deformation, *etc.* Therefore, we use the term 'flow' in a wider sense.[221] In addition to studies of the motion of individual molecules and molecular aggregates (by measuring the nuclear spin relaxation times and magnetisation transfer processes) and diffusion, MRI allows investigations of the transport of macroscopic mass quantities of, *e.g.*, liquids, gases and solids.[116, 222, 223] The technique does not require introduction of tracers into the flow, imposes no limitations on the refraction indices of the media under study and provides a tool for studying optically opaque flows, *e.g.*, multiphase flow and flow of granulated solid materials through the entire volume of the flowing substance. Usually, the results of MRI studies are in good agreement with those obtained using other flow investigation techniques including optical methods.[221, 224, 225] In contrast to many conventional methods, MRI also allows reliable visualisation of unstable flow regimes [226] and investigation of transverse velocity dispersion.

The minimum flow velocity measured in the experiments is limited to diffusive molecular displacements (nearly 10 μm s^{-1} for unbound water and 1 μm s^{-1} for macromolecules [227]). The maximum velocity is determined by the outflow of the sample from the RF coil during the measuring time. The relative accuracy of the velocity measurements is usually several per cent. Knowledge of the velocity field allows, in particular, mapping the deformation rates of the medium and calculations of the volumetric flow of the fluid, which can be compared with the experimental results.[228] It should be noted that the quantities measured by the MRI technique are statistically averaged over space and time and that the averaging scale can be varied; this provides a way for comparing the experimental data with the predictions of the theoreties based on the averaged quantities.[221] For instance, in most cases the experimental data were found to be in satisfactory agreement with the results of hydrodynamic calculations for different fluids and flow geometries.[224, 229–240]

In studies of, *e.g.*, the flow of fluids the results are often represented as the spatial velocity distribution maps; however, the experimental techniques discussed below involve measurements of the molecular displacements over the observation time. These measurements are equivalent to the velocity measurements provided that the velocity remains constant over the observation time. This should be kept in mind, in particular, in the molecular diffusion or hydrodynamic dispersion studies.

This review concerns only a few applications of the MRI technique to flow studies in biology and medicine. At the same time, there is a wealth of such applications and a number of problems can be solved using the NMR imaging techniques employed in medical MRI evaluation. For instance, MRI has long and successfully been used in transport studies of blood and other fluids in living organisms.[241–243] For instance, it was established that the arterial blood flow velocity can be as high as 150 cm s^{-1} (see Ref. 244) at the Reynolds numbers of up to 12 000. It should be noted that the demand to study the pulsatory flows in elastic branching vessels in the presence of spiral, vortex and reversible (in particular, valvular regurgitation induced) flows led to the development of special techniques.[228, 245–248]

2. Methods of flow studies

The method of spatial tagging is based on the creation of tags (magnetic stripes) by changing the NMR signal in a particular region of the sample followed by tracing the movement and change in the shape of the markers in the NMR images.[221, 249] A tag can be created using, *e.g.*, inversion or saturation of the NMR signal. In particular, the use of selective pulses and field gradients allows local manipulation of the signal in the specified slice. If the tag plane is not parallel to the image plane, the tag looks like a contrast stripe in the NMR image (Fig. 3 *a*). With an increase in the delay time between the instant at which the tag is created and the instant at which the image is acquired the relative and absolute displacements of different parts (regions) of the sample will be followed by displacement and change in the shape of the tag (Fig. 3 *b*,*c*). The lifetime of the tag is determined by the longitudinal relaxation time, T_1, of the nuclear spins.

Creation of a single tag is usually sufficient to study low-dimensional flows. For instance, creation of a tag in the plane orthogonal to the developed flow in a straight tube and imaging the tag shape after some time immediately gives the flow velocity field (see Fig. 3 *b*,*c*). Studies of more complex flow patterns involve creation of many tags. One can, *e.g.*, simultaneously create a number of parallel stripe-like (or planar) tags and then to create the second set of perpendicular tags.[226, 237, 250–254] In this case the displacement of the tag cells in the NMR image permits the determination of the local flow velocity while distortion of the cell shape is related to the shear deformation.[221]

The time-of-flight technique is also based on disturbance of the NMR signal in a particular region of the sample by the RF pulses using the signal inversion or saturation techniques. However, this approach usually involves observation of subsequent changes in the NMR signal amplitude due to displacements of the disturbed and undisturbed spins in the sample. NMR signal

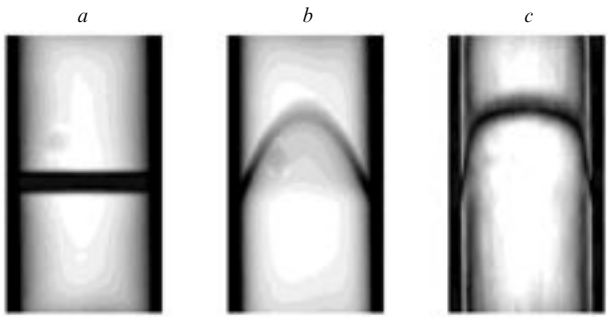


Figure 3. MRI images of water in a tube of 7.6 mm i.d.
Stagnant water, Re = 0, the delay between the tag creation and image acquisition is 4.1 ms (*a*); laminar flow, Re = 250, the delay is 83.1 ms (*b*); and turbulent flow, Re ≈ 8300, the delay is 7.1 ms (*c*). The tag was created using the spin saturation technique in the slice 1.4 mm thick and perpendicular to the plane of the two-dimensional image obtained without slice selection. Image size: 1 cm (horizontal dimension) × 3.1 cm (vertical dimension).

recovery in the disturbed region occurs due to inflow of the spins with equilibrium polarisation from undisturbed upstream regions. Simultaneously, the signal amplitude in the undisturbed downstream regions will decrease due to replacement of the undisturbed spins by the disturbed ones. In this case, variation of the signal amplitude will depend on the flow velocity (the time of flight) in a given region of the sample.

The time-of-flight technique can also be implemented without disturbance of the NMR signal by the RF pulses, since the initial magnetisation of a fluid inflowing into the magnet is close to zero and the spin relaxation rate of the fluid will depend on the time of flight taken to reach the RF detection coil, *i.e.*, it will be different for the spins experiencing different flow velocities.[255] Signal inversion can be achieved by adiabatic passage through resonance if the fluid flows along the direction of the field gradient. The use of time-of-flight technique without spatial resolution gives the average flow velocities.[242] The spin disturbance and signal acquisition regions can be different. For instance, one RF coil can be used for signal disturbance while the second (detection) coil can be placed downstream.[242, 255] It should be noted that in the literature the names of the two methods considered above are often used as synonyms since they involve creation of a spin disturbance in a particular region of the sample followed by observation of variations of the NMR signal.

Quantification of the molecular velocities and mapping the fluid velocity fields are often carried out using the phase (phase contrast) technique.[253, 254, 256–258] In this case the pulse sequence is designed in such a way that the phase of the signal to be acquired be proportional to the spin motion velocity. For instance, if the pulse sequence includes two field gradients with the effective amplitudes $-g_i$ and g_i, duration δ and the time delay Δ between them, the phase of the transverse magnetisation will change by

$$\phi = \gamma v_i \mathrm{M}_1 = \gamma v_i \int t g_i(t) \mathrm{d}t = \gamma v_i \mathrm{g_i} \Delta \delta, \qquad (17)$$

where M_1 is the first moment of the gradient sequence. As can be seen, variation of the signal phase is independent of the spin location and proportional to the velocity component (v_i) parallel to the applied gradient g_i.

Flow velocity induced variation of the magnetisation phase must lie between $-\pi$ and π to exclude ambiguity of the dependence between the phase and velocity.[259] However, sometimes this limitation is deliberately violated. If the signal-to-noise ratio and the spatial resolution of the experiment are sufficiently high, this ambiguity can be corrected for by adding a value of $\pm 2\pi n$ to the measured phase to eliminate the phase discontinuities ($\pm 2\pi$) between the signals from adjacent pixels.[260] At the same time, if the maximum phase variation is much larger than π, the NMR image represents a map of isovelocity lines.[261]

Since the phase of the NMR signal depends on many factors, measuring the molecular velocities requires separation of the flow-related contribution, which can be done in a number of ways.[256] Often, an experiment is repeated twice and thus , and in one of the repetitions expression (17) is set to zero by either turning off the flow ($v_i = 0$) or by setting M_1 equal to zero (by *e.g.*, setting $g_i = 0$). Mapping the projection of the velocity vector on the direction of the applied gradient is achieved by calculating the phase difference for each pixel followed by calculating the velocity using expression (17). Phase modulation of the NMR signal can be readily converted into amplitude modulation using the RF pulses; therefore, the NMR signal amplitude is sometimes used as a measure of the velocity.[261–263] In this case, the Fourier transformation of the experimental data immediately gives the velocity map without performing additional calculations.[262] Imaging techniques with the signal amplitude depending on, *e.g.*, flow velocity gradient have been reported.[264]

Partial outflow of the fluid from the detection coil in the phase contrast experiments does not disturb the observed flow pattern since the phase rather than amplitude of the NMR signal is measured. At the same time, if a substantial fraction of the fluid leaves the RF coil over the acquisition time, this can lead to loss of the signal against the noise background, thus preventing the determination of the signal phase and, hence, of the flow velocity for a given image pixel.

It should be noted that NMR imaging of a moving object or its parts faces some difficulties, *e.g.*, image distortions due to variation of the spin precession frequency caused by the spin motions in the presence of the field gradient. In addition, dephasing of the magnetisation within the same pixel due to different spin velocities leads to loss of the signal in the NMR image. To avoid these undesired effects, the so-called flow-compensating technique is employed. Namely, the gradient sequence is designed in such a way that the first moment of the sequence, M_1 [see expression (17)], be zero; in this case, the phase of the signal to be acquired is the same for particles moving with different velocities, thus precluding image distortions. The condition $M_1 = 0$ is realised, in particular, for even echo signals at multiple refocussing of the transverse magnetisation in the constant field gradient. Therefore, the even echo partially prevents the loss of the signal intensity even in the case of turbulent flow.[265]

The phase encoding technique can also be used for measuring higher derivatives of the molecular coordinates with respect to time. For instance, setting M_1 to zero allows the molecular acceleration to be determined. In this case, the phase of the transverse magnetisation is proportional to the product of the projection of the acceleration vector on the direction of the field gradient by the second moment of the gradient sequence

$$M_2 = \int t^2 \mathrm{G}(t) \mathrm{d}t.$$

The sources of possible difficulties and errors in the phase encoding of flow have been analysed.[228]

An image of a fluid flow can be obtained by visualisation of streamlines by creating multiple tags. For steady-state flows the tags in the form of stripes parallel to the streamlines remain unchanged. The tags are created in the form of stripes parallel to streamlines in the upstream regions with respect to the flow region under study. Curved streamlines (if, *e.g.*, a fluid flow in a tube with a diaphragm is studied) inside the flow region under study initially are not in parallel to the straight tag stripes. However, after some time the tags adopt the shape of the streamlines as a result of replacement of the fluid in this region by the fluid from the upstream region.[266] Streamline images can also be calculated using information on the three spatial fluid velocity components.[267]

For non-steady-state flows (*e.g.*, pulsatile intracardiac blood flow), realistic flow patterns can be obtained by visualising the trajectories of the movement of an ensemble of phantom particles that were mentally 'introduced' into the flow at some instant.[267] Combining trajectory visualisation technique with animation and with overlay of the trajectory images [267] or a colour velocity map [246] on the 2D images of anatomic sections gives a complete image of such a flow.

NMR angiography is widely used [241, 268, 269] in medical evaluation to provide a maximum contrast between the vasculature and surrounding tissues (usually, images of bright vessels against dark background are obtained). This is achieved using various versions of the time-of-flight technique. The most widely used approach involves predominant saturation of immobile spins by imaging at fast repetitions of the gradient echo sequence. The phase techniques and some magnetisation transfer based approaches are also employed in angiography. The quality of angiograms can be improved using some contrast agents that are introduced into blood to shorten the spin relaxation times.[241, 242] NMR angiography allows studies and characterisation of blood flow and, in particular, establishment of the presence of obstacles and the determination of conditions under which the blood flow favours the appearance of plaque depositions.[234, 244]

As mentioned above, diffusive molecular displacements can be studied by q-spectroscopy. This method is also widely used in the flow studies. For instance, if isotropic molecular diffusion with the diffusion coefficient D is superimposed on the flow characterised by the velocity $\mathbf{u}$, the expression for the echo amplitude, $E(\mathbf{q},\Delta)$, has the form

$$E(\mathbf{q},\Delta) = \exp(-4\pi^2 q^2 D\Delta_{\text{ef}} + i\,2\pi\mathbf{q}\mathbf{u}\Delta). \tag{18}$$

As can be seen, diffusion leads to attenuation while flow causes modulation of the NMR signal. By applying the Fourier transformation of the signal one gets

$$P(\mathbf{R},\Delta) = \frac{1}{\sqrt{4\pi D\Delta_{\text{ef}}}}\exp\left(-\frac{R^2}{4D\Delta_{\text{ef}}}\right)\otimes\delta(\mathbf{R}-\mathbf{u}\Delta) = \tag{19}$$

$$= A\exp\left[-\frac{(R-u\Delta)^2}{4D\Delta_{\text{ef}}}\right].$$

Here δ is the delta function, the symbol $\otimes$ denotes convolution and A is a constant. As in the case of diffusion [see expression (13)], the propagator (19) has a Gaussian shape; however, in the presence of a flow the maximum of the propagator is shifted from the point $\mathbf{R} = 0$ to $\mathbf{R} = \mathbf{u}\Delta$.[270] If the diffusive molecular displacements over time Δ are small, the propagator $P(\mathbf{R},\Delta)$ characterises the flow velocity distribution (histogram).[271,272] The direction of the displacement component to be measured, $\mathbf{R}_i$, is determined by the direction of the field gradient g_i.

Since measurements of the average propagator are based on measurements of the NMR signal amplitude, outflow of the fluid from the RF coil can lead to underestimation of the measured $P(\mathbf{R},\Delta)$ value. This underestimation usually increases with an increase in $\mathbf{R}$, since higher flow velocity corresponds to a larger number of spins that have time to escape from the RF coil during the observation time Δ. Partial suppression of this effect can be achieved by measuring the propagator using the slice-selective normal to the direction of the net flow rather than for the entire sample placed in the RF coil. Obtaining reliable results requires detailed analysis of artifacts and measurement errors.[141]

Similarly to diffusion studies, the use of an extra module in the pulse sequence to encode the spatial information (the so-called dynamic MRI) allows spatially resolved measurements of the average propagator $P(\mathbf{r},\mathbf{R},\Delta)$ [see formulae (14) and (15)]. The use of the dynamic MRI is of crucial importance in the presence of a velocity distribution within the same pixel (low spatial resolution, thin capillaries, *etc.*).[270,273,274] In this case other methods for obtaining the flow velocity map only allow the effective velocity for each pixel to be determined, whereas measurements of the spatially resolved propagator make it possible to avoid this undesired averaging. Dynamic MRI with high spatial resolution can be useful in, *e.g.*, obtaining rheological information on non-Newtonian fluids, in studies of dynamic processes in plants and for the determination of the diffusion coefficient and average flow velocity for each image pixel.[141]

The above-mentioned methods can be used for imaging of the motions characterised by coherence in the measuring time scale, *e.g.*, in studies of steady-state flows. Diffusion, hydrodynamic dispersion and turbulence cause the loss of coherence and attenuation of the NMR signal.[275] These processes can be best studied by the methods based on recording the signal amplitude variations (in particular, by measuring the propagator). Nevertheless, in the case of a developed turbulent flow both the phase encoding and the tagging technique can be used to study the average molecular displacements over the measuring time. In principle, the amplitude of the signal in the NMR images allows one to extract information on the incoherent component of the motion (turbulent or periodic pulsations, diffusion, dispersion);[251,252,276] however, this problem is hard to solve. Non-steady-state processes (including aperiodic, transient and turbulent flows) can be studied by fast (10–100 ms) imaging techniques. In the case of periodic flows the use of synchronisation of the pulsatory flow and the NMR signal acquisition allows relatively slow imaging techniques to be employed to determine the flow pattern at different instants of the pulsation period. Medical experiments concerning blood flow in organisms usually involve synchronisation of the NMR measurements with the electrocardiogram signal.

By measuring the spin echo amplitude with varied pulse sequence parameters one can determine the quantities employed in the statistical description of a random fluid motion[265,275,277–279] including the correlation time of velocity fluctuations, τ:

$$\tau = \int_0^\infty \frac{R_u(t)\mathrm{d}t}{R_u(0)}. \tag{20}$$

Here, $R_{\text{u}}(t)$ is the velocity autocorrelation function

$$R_u(\tau) = \langle u(t)u(t+\tau)\rangle, \tag{21}$$

while the particle velocity, $v(t)$, is represented by the sum of the average velocity, U, and the fluctuating component, $u(t)$

$$v(t) = U + u(t). \tag{22}$$

If τ is much longer than the duration of the pulsed field gradients and the time delay between them, a turbulent flow can be correctly described in terms of the mean square of velocity fluctuations, $\langle u^2\rangle$, or turbulence intensity, I

$$I = \frac{\sqrt{\langle u^2\rangle}}{U}. \tag{23}$$

Otherwise, in the short correlation time limit, a turbulent flow can be characterised by the eddy diffusivity, D_{e}

$$D_{\text{e}} = \langle u^2\rangle\tau. \tag{24}$$

MRI allows measurements of both quantities, I and D_{e}, as well as studies of spin exchange processes in the coordinate and velocity space.[280–282] In particular, by independently varying the amplitudes of two gradient pulses one can obtain a 2D NMR spectrum with the axes corresponding to the spatial coordinate of the spin at the instants t and $t + \Delta$ (x_1 and x_2), while the signal amplitude is proportional to the probability density of the spin displacement from x_1 to x_2 over time Δ (position exchange spectroscopy, or POXSY). The 1D sections of such a 2D spectrum characterise the probability distribution of spin migrations over different distances over a specified time. At small spin displacements (*e.g.*, at short times Δ), the 2D POXSY spectrum exhibits a signal (ridge) along its diagonal. As the spin displacements increase, the diagonal ridge is broadened until complete loss of correlation between the initial and final coordinates. It is noteworthy that the diagonals of such a 2D spectrum correspond to the average coordinate ($\langle x\rangle$) and the average velocity ($\langle v\rangle$); therefore, the same 2D spectrum rotated by -45° characterises the correlation between the average particle coordinate and average particle velocity (the probability density for a particle located at position $\langle x\rangle$ to have the velocity $\langle v\rangle$).

Analogously, independent variation of two pairs of gradients in the four-gradient experiments allows exchange studies in the velocity space,[238,280,281] *i.e.*, the probability density for the spin velocity to change from v_1 to v_2 over time Δ irrespective of the spin position (velocity exchange spectroscopy, or VEXSY). The same VEXSY spectrum rotated by -45° characterises the correlation between the average velocity and average acceleration of particles. For unrestricted diffusion the correlation spectrum has a shape of a 2D Gaussian with the standard deviation $\sigma = (2D\Delta)^{0.5}$, where D is the self-diffusion coefficient of water.[238] The SERPENT (sequential rephasing by pulsed field gradients encoding N time intervals) experimental technique[283,284] allows studies of the spin velocity or spin displacement correlations for two time intervals measured from a common initial time instant.

3. Fluid flow in various geometries

A developed laminar flow of a Newtonian fluid in a circular cross-section tube or capillary is characterised by a parabolic longitudinal velocity distribution along the tube diameter with a maximum at the tube axis and a zero flow velocity at the tube wall

$$\upsilon = \upsilon_{\max}\left[1 - \left(\frac{r}{R}\right)^{\beta}\right], \tag{25}$$

where R is the tube radius, r is the distance from the tube axis to the observation point and $\beta = 2$. These distributions were obtained by both MRI tagging technique (see Fig. 3 *b*) and using the maps of longitudinal velocity.[93, 141, 227, 261, 272, 285–288]

The motion of water flowing through a narrow tube into a cell containing a fragment of a monolithic catalyst with transport channels of different shape and cross section dimensions have been studied.[8, 20, 93] Mapping the three velocity components at different distances from the inlet edge of the monolith allowed detailed visualisation of a complex flow pattern and a transition to the fully developed flow in the inlet portion of each transport channel. Experiments revealed the presence of counterflows both inside and upstream of the monolith as well as jets flowing out of the transport channels and a vortex motion of water in the immediate vicinity downstream the block.[93] A film flow through the channels of a monolithic catalyst at different fluid flow rates has been investigated.[289] The flow of a silicon oil film ~ 1 mm thick on the surface of a vertical plate made of poly(methyl methacrylate) has been studied by mapping the velocity and spin density distributions.[290] The flow velocity was found to be higher near the plate edges, where the film was thicker due to wetting effects. This velocity increases quadratically with the distance from the plate surface. An increase in the Reynolds number causes the appearance of surface waves on the film surface. The appearance of standing waves was observed with pulsatile supply of silicon oil when the system was isolated fron the atmosphere.

Spatially resolved MRI was employed in studies of a developed turbulent flow of water in a tube. The experiments revealed a large average velocity gradient near the tube walls and a nearly planar velocity distribution profile for the rest of the tube cross-section [272] (see Fig. 3 *c*).

However, sometimes measuring the velocity for each image pixel is insufficient. Even in the studies with high spatial resolution the molecules within the same image pixel are characterised by different displacements due to, *e.g.*, molecular diffusion. Dynamic NMR microimaging provides a tool for measuring the displacement distribution within each image pixel.[287, 291] At high spatial resolution, the average propagator for an image pixel is a Gaussian curve [see expression (19)]. The width of the propagator peak is determined by the diffusive molecular displacements while the shift of the maximum position is determined by the average molecular displacement due to the fluid flow.[141, 270] At small diffusion coefficients (*e.g.*, for polymer solutions), the distribution of the molecular velocities within the same image pixel leads to overestimation of the apparent D value. In the case of a laminar flow this can be avoided by using flow-compensating technique. A feature of flows in thin capillaries is the possibility of overestimating the apparent D values for the near-wall region due to the presence of small air bubbles on the capillary walls, which disturb the flow pattern.

If the spatial resolution is low, the molecular velocity distribution within the same pixel can be rather broad.[292] Moreover, for thin capillaries surrounded with a stagnant fluid each image pixel can reflect both the flowing and the stagnant fluid, which leads to incorrect measurement of the average velocity and fluid flow rate in the capillary.[293] In this case, measurements of the propagator for each image pixel allow one to obtain complete information on the fluid flow and to separate the contribution of the stagnant fluid to the NMR signal.[270, 273]

Fluid flow in a tube can also be studied by measuring the propagator without spatial resolution.[93, 272, 280] In the case of a laminar flow of a Newtonian fluid in a cylindrical tube the propagator considered as a flow velocity function is nearly constant in the υ range from zero to $\upsilon_{\max}$ and equals zero at $\upsilon > \upsilon_{\max}$ (Fig. 4 *a*). If we go to a turbulent flow at Re > 2300, the probability density becomes an increasing function of the flow velocity up to $\upsilon = \upsilon_{\max}$. Noteworthy is that an analogous propagator can also be observed in the case of a laminar, but not completely developed, flow [93] or a laminar flow of non-Newtonian fluid (*e.g.*, blood).[272] Studies of spin exchange in the coordinate and velocity space for a laminar [281] and turbulent [280] flow of water in a tube and for a water flow in a converging tube [281] were carried out using the POXSY and VEXSY techniques.

A feature of a model of a real dialysis cell (artificial kidney) is counterflow of water inside hollow cellulose fibre membranes ('blood') and in the outer jacket ('dialysis solution').[73, 287] An increase in the cell packing density due to the use of textile fibres leads to a more homogeneous flow distribution of the 'dialysis solution'. The regions near the ends of the dialysis cell are characterised by increased maximum water flow velocity (by a factor of 1.4) compared to the velocity in the bulk of the cell due to swelling of the membranes surrounded by rigid polyurethane shell used for cell hermetisation.[287] Unfortunately, the 2D VEXSY spectra revealed no cross-peaks that could be indicative of the reversal of the direction of the molecular motion.[280]

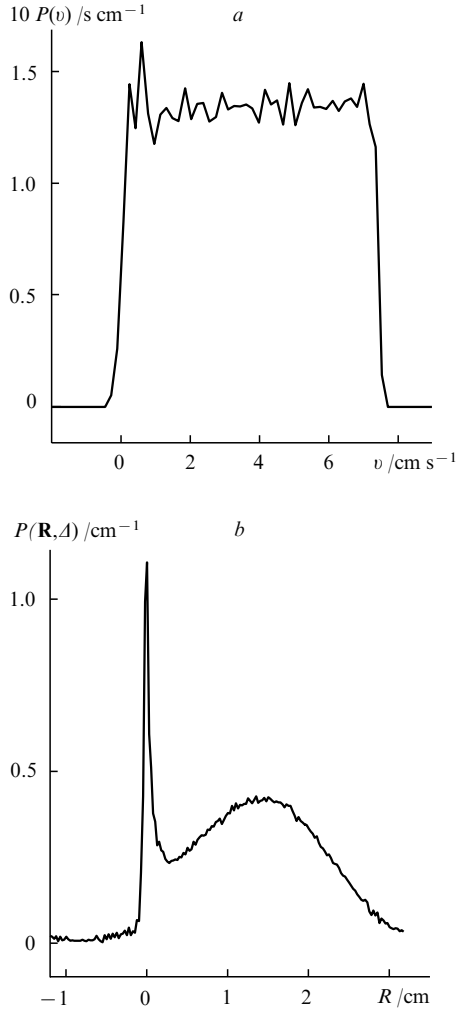


Figure 4. Averaged propagator for axial molecular displacements in flowing water.
Laminar flow (Re = 285) in a tube with circular cross-section (*a*); flow in a cylindrical glass bead pack (*b*). Bead diameter: 3.2 mm; bead pack diameter: 21 mm; observation time: $\Delta = 306$ ms.

Considerable attention has been given to the NMR studies of convective motion of various nature. Fluid flow inside a porous hollow-fibre membrane is known to induce slow convective flows in the surrounding fluid. For instance, an NMR imaging study of a reactor with 40 parallel membranes revealed an increased flow velocity in the narrow gaps between adjacent membranes.[231]

Convection can arise even at relatively small temperature gradients (*e.g.*, 0.05 K cm^{-1} for convection in chloroform). In particular, the temperature gradient in the bore of a magnet of an NMR spectrometer is sufficient to induce a convective flow of water with a velocity of up to 0.5 mm s^{-1} (see Ref. 261). Such a flow in a liquid-containing ampoule 5 mm in diameter was also induced by temperature gradients during thermal regulation or as a result of absorption of the RF radiation. The flow velocity was $\sim$0.5 mm s^{-1} for water or DMSO and reached up to 5 mm s^{-1} for chloroform.[262, 294] The 2D NMR images exhibited the presence of numerous convection cells and 'twisting' of the nodal plane in the ampoule.[262]

Rayleigh convection with velocities of up to 600 μm s^{-1} was observed in a bottom-heated silicon oil layer 1 cm thick.[295] The study revealed the presence of four convection cells whose pattern and relative sizes were in agreement with the results of visual observations. A 5% polystyrene solution in cyclohexane in a bottom-heated ampoule exhibited the presence of a convection cell and a steady-state character of convection.[296]

A convective fluid flow in a freely falling droplet has been studied as a model system with two interacting phases.[297] Because of the short residence time of the droplet inside the RF coil recording a 3D NMR image required a total of 33 800 droplets to fall. The droplet size reproducibility was better than 99%. Large-scale water circulation in droplets was mapped and it was shown that the addition of surfactants causes reduction of the droplet diameter, improves reproducibility of the droplet size and shape and shifts the convection pattern towards much smaller length scale.

If a fluid has some regions with locally different concentrations of oppositely charged particles, application of an external electric field induces electro-osmotic transport. For instance, placing a closed capillary with charged walls filled with aqueous KCl solution (1 mmol $litre^{-1}$) in an axial electric field causes the fluid in the near-wall region to move, which is due to the increased concentration of the counterions in the near-wall layer.[298] This induces a neutral fluid flow with parabolic velocity distribution along the tube diameter; however, in contrast to conventional flow in the tube, the flow velocity on the walls differs from zero and is reversed with respect to the flow velocity direction at the capillary axis.[235, 298] The characteristic flow velocity was found to be 0.1 mm s^{-1} while the settling time of the steady-state flow with pulsed switching on the electric field was of the order of 100 ms.[298] The use of coatings neutralising the surface charge reduces the electro-osmosis effect.[235]

A nitrobenzene–C_6D_6 mixture also exhibited electroconvection, which can be due to the appearance of the space charge as a result of association of the polar molecules around the ions.[282] In this case, the expression for the effective diffusion coefficient at room temperature has the form

$$D = 1.08 \times 10^{-5}\ \mathrm{cm^2\ s^{-1}} + (3.33 \times 10^{-5}\ \mathrm{cm^4\ kV^{-2}\ s^{-1}})\, E^2,$$

where E is the strength of the applied electric field.

The flow of fluids in curved channels is strongly different from the flow in straight tubes. The pressure gradients directed normal to the net flow are responsible for the appearance of complex secondary flows, which lead to significant changes in the flow pattern. A laminar flow of water in a tube with abrupt contraction and/or expansion exhibits large deviations from the parabolic longitudinal velocity distribution and rather high radial velocities. It was found that the flow velocity increases (decreases) as water flows in (flows out of) the narrow region of the tube. Recirculation flow has also been observed in the immediate vicinity downstream the expansion.[232, 233] The flow of water in branching tubes has been studied.[256]

Fluid flow in a tube with an U-shaped bend exhibited parabolic longitudinal velocity profiles before the bend[299] and an acceleration of the flow near the inner wall of the tube just after the curved section, which induced a displacement of the rapidly moving molecules and the maximum flow velocity towards the outer wall.[236, 239, 263, 299] Rather fast flow produced rotating, spiral Dean vortices that were clearly seen in the transverse velocity maps.[299]

To obtain the velocity distribution maps at different instants of the pulsation period, studies of pulsatile flow in straight[240] and U-shaped tubes[236, 239] were carried out with synchronisation of the pulse sequence with flow pulsations.

Studies of aperiodic flows require the use of fast NMR signal acquisition techniques. For instance, imaging over a period of 20 to 50 ms allowed one to obtain an 'instantaneous' velocity distribution map for a turbulent flow of water in a tube.[251, 264, 300] In particular, a transition to turbulence with alternation of turbulent and laminar flow regions in the flow pattern was detected in the Re range between 1500 and 3000. The 1D temporal autocorrelation function of the signal amplitude and the 2D spatial autocorrelation function of the signal amplitude corresponding to the transition to turbulent flow were calculated.[264] It was found that the correlation time is maximum (0.45 s on the tube wall and 0.8 s at the tube centre) at Re = 2000 and decreases with an increase in the Re value due to the appearance of progressively faster and smaller vortices. The correlation length was maximum (4 mm) at Re = 3000 and also decreased as the Reynolds number increased. Transition to a turbulent flow and recirculation flows in a tube with a contraction have been studied at different Reynolds numbers[244, 301] and the appearance of a Karman vortex street behind the rod placed in the tube normal to the direction of the net flow (Re = 39–200) has been explored.[244] At Re $\geqslant$ 82, the vortices rotating in the opposite direction alternately separated from different sides of the rod at a frequency of 1.7 Hz. The use of fast NMR imaging techniques also allows studies of transient flows, *e.g.*, establishment of a steady-state regime in the system after starting the flow.[233]

Statistical characteristics of a flow at long correlation times, τ, of velocity fluctuations have been measured for a turbulent flow of water in a tube and for grid-generated turbulence using grids of different cell size.[277] For the flow in a tube at Re > 2000 the mean square velocity fluctuation rapidly increases as the Re value increases, whereas the flow turbulence intensity remains nearly constant. Measurements in the opposite, short τ limit allowed one to obtain the spatial τ distribution maps and the eddy diffusivity (D_e) distribution maps for the fluid flowing in the region behind the tube contraction/expansion[278] and for a jet flowing through a tube into the flat wall of a right liquid-filled cylinder.[302] In the last-mentioned experiments the D_e values reached 0.7 $cm^2\ s^{-1}$.

The Taylor–Couette flow, *i.e.*, the flow of a viscous fluid in the gap between two coaxial cylinders rotating at different rates, is of great practical value. Mapping the spatial velocity distribution using the NMR imaging technique allows characterisation of the flow of the fluid in the gap.[226, 303] At low rotation rates, a cylindrical fluid flow occurs, which is employed, in particular, in conventional Couette viscometers. As a critical combination of the cylinder rotation frequencies is reached, a flow instability appears, leading to the appearance of Taylor vortices in the form of toroidal cells in the longitudinal direction.[226] This effect is used in separators and mass transfer reactors. The size and behaviour of the Taylor cells for the spiral Poiseuille flow (a combination of the Couette flow and longitudinal fluid flow) has been studied.[226]

Rotational motion including the Couette flow can be studied using the oscillating (rotating) field gradients. Varying the rotation frequency of the field gradient allows selective observation of the signal of a cylindrical fluid volume element for which the rotation frequency coincides with the gradient rotation frequency.[304] The 2D correlation spectra of the Couette flow

obtained using the VEXSY exchange spectroscopy exhibit a complex 'ridge' pattern, which is to some extent similar to the Pake structure in the 2D dipolar correlation spectroscopy.[238]

Information on the flow of fluids in extruders is useful for optimisation of extrusion process. The velocity distribution maps of a 1.5% aqueous carboxymethylcellulose solution in an extruder with open or closed discharge with immobile cylinder and a rotating straight or tapered screw, obtained using the MRI technique were compared with the results of model calculations.[230]

MRI is also widely used in the investigations of multicomponent flow systems; the technique allows studies of the flow of individual components of complex mixtures. The contributions of different components can be separated in a variety of ways.[1, 288] Application of the chemical shift selective NMR imaging was demonstrated taking the oil-in-water emulsions as examples. This type of emulsions is of great importance for food and petrochemical industries.[288, 305] It was found that the radial distribution profiles of the longitudinal velocity [288] and the maximum velocity [305] for water and oil are identical. At the same time, profile-shape analysis showed that the emulsion viscosity decreases as the shear rate increases.[288] Partial separation of the emulsion due to shear-induced migration of the dispersed phase allowed one to observe the flow of neat oil, water and emulsion as well as a recirculation flow in front of the tube contraction.[288]

Complex fluids, such as polymer solutions and melts, emulsions, suspensions, gels and micellar solutions exhibit viscoelastic properties under mechanical stress. Rheology studies the mechanical properties of such viscoelastic fluids, usually under conditions of a steady-state flow accompanied by shear deformation. The rheological properties of non-Newtonian fluids should be taken into account in the design of various technological processes. Online measurements of the rheological properties of materials in the course of a technological process are of importance for control purposes. MRI can be used as a technique for fast contactless determination of the rheological properties of materials.

In contrast to conventional methods, a single NMR flow imaging experiment with a viscoelastic fluid can provide information on the fluid viscosity over a broad range of shear rates. Information on the shear rate is extracted from the spatial flow velocity distribution maps.[306, 307] For instance, for a laminar fluid flow in a capillary [expression (25)] the shear rate,

$$\dot{\gamma}(r) = \left| \frac{\mathrm{d}V(r)}{\mathrm{d}r} \right|, \tag{26}$$

continuously changes from zero at the centre of the capillary to the maximum value on the capillary walls. Given the pressure drop, the expression for the shear stress has the form

$$\sigma(r) = -\frac{\Delta P}{2L} r, \tag{27}$$

where r is the current radius and $\Delta P/L$ is the pressure gradient. Shear viscosity can be found as

$$\eta(\dot{\gamma}) = \frac{\sigma(\dot{\gamma})}{\dot{\gamma}}, \tag{28}$$

which allows extraction of information on the shear viscosity for a range of shear rates from one map.[306]

A number of rheometer designs and features have been reported.[308, 309] These devices can be placed inside the probe of an NMR microimager to perform rheo-NMR microimaging studies of the properties of various fluids. The flow velocity distribution maps of water and polydimethylsiloxane in such rheometers have been obtained.[308] Rheometers are small devices and require small amounts of fluids to be studied; hence, one can produce high shear rates.[308, 309] It was found [308] that combining rheo-NMR microimaging and NMR spectroscopy allows one to relate the mechanical properties of fluids to their molecular properties. For instance, the ^{2}H NMR spectrum of a CTAB/D_2O micellar solution (CTAB is cetyltrimethylammonium bromide) was studied as function of the radial coordinate in the gap between two cylinders in the Couette geometry. Line splitting in the NMR spectrum measured in the region of the maximum mechanical stress near the internal cylinder walls indicated the formation of a nematic phase in this region of the sample. In a study of polyacrylamide in D_2O it was found that the shear rate correlates with the spin relaxation times of the polymer.

The rheological behaviour of polymer melts, including the shear viscosity, is of great importance in many technological processes. For instance, the molecular mass distribution of linear polymers correlates with the dependence of their shear viscosity on the shear rate.[306] Velocity profile measurements for a low density polyethylene melt flowing at 232 °C along a cylindrical tube showed that the fluid exhibits a nearly Newtonian behaviour; a slight decrease in viscosity was observed only at shear rates higher than 1 s^{-1}.[307]

A markedly decreasing dependence of the shear viscosity on the shear rate (the minimum and maximum values differ by two orders of magnitude) was obtained for the flow of a 1% carboxymethylcellulose solution in a tube.[306] This dependence is in agreement with the results of conventional measurements performed at shear rates exceeding 10 s^{-1}.

A feature of the motion of suspensions and pastes under conditions of inhomogeneous shear distribution is particle migration towards the region of low shear rate,[310] which results in strong concentration gradients in the initially well-mixed suspensions and has a negative effect on their heat exchange properties. Simultaneously, this causes essential changes in the rheological properties, since the effective viscosity is strongly dependent on the particle concentration.

A number of studies has been devoted to the investigations of particle migration and its influence on the velocity distribution and concentration profiles for suspensions of microspheres immersed in viscous fluids in different flow geometries. For instance, a suspension of monodispersed spherical particles in a Newtonian fluid of the same density was plunger pumped [311] along a cylindrical tube with abrupt contraction and expansion. The velocity distribution along the diameter was described by the function (25) with $\beta = 2.8$. Analogous experiments were carried out for a suspension of poly(methyl methacrylate) microspheres in polyalkylene glycol in the Couette flow and in a single-screw extruder with a closed outlet.[237]

Separation into phases with substantially different viscosities was observed for an aqueous micellar solution and tomato sauce in a plate-and-cone rheometer. Tomato sauce was found to separate into two phases with different rheological properties in Couette geometry.[308]

Blood can be considered as a complex heterogeneous suspension. Probably, a nonlinear relationship between the mechanical stress, σ, and the shear rate $\dot{\gamma}$

$$\sqrt{\sigma} = 0.33 + 0.16\sqrt{\dot{\gamma}} \tag{29}$$

can be explained by blood erythrocyte migration towards the region with minimum shear stress at the centre of the tube.[272] 'Stacking' of erythrocytes at low shear rates equalises the flow velocity along the cross-section of the capillary, thus flattening the maximum of the velocity distribution profile even at small Reynolds numbers (10 – 50); in addition, some indications of flow disturbance and the presence of the transverse velocity components have been reported. After transition to a turbulent flow (at Re $\approx$ 2300) the experimental blood velocity profile was less flattened than the velocity profile of a water – glycerol mixture of the same viscosity, which can be associated with the elastic properties of erythrocytes.[272]

Water flow at the centre of a developing wheat grain [188] and a rising water flow in plant stems [227, 270] (from 45 μm s^{-1} to

3 mm s^{-1}) have been studied. A downflow of nutrients towards the roots of the plant in a castor bean seedling has been reported.[273] Since the pixel size in the NMR images is much larger than the wood tracheid diameters, reliable determination of the velocity in most cases was achieved using the dynamic MRI technique.[188, 270, 273, 291] This approach permits simultaneous measurements of the velocity distribution maps and the diffusion coefficient. For instance, the experimental diffusion coefficient of water in a wheat grain was found to be 8.3×10^{-6} cm^2 s^{-1}.[188] In studies of water flow in developing quail and bantam eggs the fluid flow was detected only after a four-day incubation period,[252] the maximum flow velocity being 1 mm s^{-1}. In addition, a pulsatile flow at a frequency of 0.4 Hz was detected in the quail egg after a 167 h incubation period.

Studies of other types of motion have been reported, *e.g.*, rotation of a gelatin sample in a tube at rates up to 60 rpm (see Ref. 300) and the transverse expansion of a gel cylinder at axial compression at a constant velocity.[286] A combination of static and quasi-static deformation of materials with phase encoding of the molecular displacements can be used for the determination of a material's response to mechanical strain followed by reconstruction of Young's modulus maps by solving the corresponding model equations.[312]

The distribution of dynamic deformations associated with the propagation of the compression and shear waves in a medium is studied by magnetic resonance elastography.[313, 314] The technique involves creation of transverse acoustic waves with frequencies ranging from 10 to 2000 Hz in tissues or materials. In this case, the wave attenuation in the medium is much smaller than the ultrasound damping, while the wave propagation velocity is low. In addition, the shear modulus varies over a range of several orders of magnitude.[315] The waves are created using mechanical or electromechanical (*e.g.*, piezoelectric) devices or a modulated ultrasonic beam. The modulated magnetic field gradients applied synchronously with the oscillations of the medium change the phase of the NMR signal, which is proportional to the spin displacement amplitude and to the amplitude, period and number of the field gradient cycles. This can be used for improving the sensitivity of the experiment to the small-amplitude oscillations of the medium.[313, 315] The technique allows the detection of displacements smaller than 100 nm. By processing the NMR images one can obtain the spatial molecular displacement amplitude maps, as well as the wave propagation velocity maps in the medium and the elastic modulus maps.[316] Observation of wave reflection from the boundaries and wave refraction at the interface between the soft and rigid regions of the medium, accompanied by variations of the wave propagation velocity, is also possible.[314, 315] The wave propagation dynamics can be visualised by combining variation of the phase shift between the magnetic field gradient and the wave with animation.[315, 317] The possibility of studying single waves or short deformation wave trains in the media [315] and observing the interference pattern for two point sources have been demonstrated.[314] Wave propagation velocity and wave attenuation measurements at different temperatures were carried out for phantoms as well as animal and human tissues.[317]

4. Filtration

Fluid flow in porous materials (filtration) often occurs in nature and technology (*e.g.*, in perfusion in biological tissues, petroleum recovery and in catalysis). Dispersive character of the flow is critical to filtration. Flow velocity dispersion is due to several mechanisms.[157, 318] For a laminar fluid flow in a tube the flow velocity dispersion is due to different particle velocities [see formula (25)]. In this case, the dispersion is to some extent reversible (this can be achieved by reversal of the flow direction). Taylor dispersion is due to random velocity modulation as a result of lateral diffusion. Mechanical dispersion is due to the velocity modulation when moving through a complex system of channels in the pore space. The presence of stagnant regions (*e.g.*, dead-ended pores) causes dispersion due to partial fluid retention.

Application of the MRI technique to studies of filtration processes has some advantages over other methods, since it allows characterisation of not only the flow properties, but also the medium structure, porosity and saturation level, which can be used for, *e.g.*, estimating the medium permeability and the capillary pressure.[319] The NMR-porosimetry technique [1] permits the pore size distribution to be determined and even the structure of the pore space to be visualised by recording the 3D images if the pores are relatively large.[318, 320, 321] The results obtained can then be used in simulation of the fluid flow. Selective detection of the NMR signals of different fluids [1] allows studies of the processes occurring in multicomponent systems.

The MRI techniques employed in the flow studies in porous media have some salient features. When determining the content of a fluid in a porous sample using the NMR imaging technique, one should take into account the fact that the T_1 and T_2 relaxation times of the fluid inside the pores are usually much shorter than those of the bulk liquids, which affects the amplitude of the NMR signal. In addition, the relaxation times depend on the saturation level of the sample.[322, 323] The relaxation behaviour is complicated in the presence of fluid mixtures. For instance, a surface film of the wetting fluid (water) prevents the T_1 time of oil (in contrast to the T_1 time of water) from 'sensing' the surface, while the transverse relaxation rate can decrease with a decrease in the oil content due to concentration of oil inside larger pores.[324] Therefore, quantitative measurements require analysis of the relaxation behaviour [322–324] and/or using the calibration curves for the signal amplitude.[324]

Placing a sample with numerous interfaces between phases with different magnetic susceptibilities in a magnetic field produces strong local field gradients, which can affect the accuracy of the results obtained, especially if the flow velocities to be measured are low.[325] Fluid flow in an inhomogeneous magnetic field causes further shortening of the decay time of the transverse magnetisation, T_2^*. Therefore, the pulse sequences based on the spin echo or stimulated echo are most often employed, which include the 180 °-pulses for refocussing of the transverse magnetisation in the local field gradients.[326, 327] Usually the condition $T_1 \gg T_2^*$ is met; hence, the stimulated echo technique is preferable. It allows one to perform measurements at the longest observation times, Δ, since in this case the NMR signal decay is determined by the T_1 rather than T_2^* time.

In most cases the pore size of the medium is less than or comparable with the spatial resolution of the NMR images.[326] This leads to a limited use of the imaging techniques involving the averaging of the fluid velocity over the volume element corresponding to a particular pixel of the NMR image.[318] In particular, calculations of the mass flow rate and the flow velocity distribution should be carried out with inclusion of partial-volume correction.[328] Therefore, often preference is given to the measurements based on the average propagator (corresponding to the number of the molecules with a given velocity, averaged over the measuring time rather than volume) [325] rather than the velocity histogram construction.[321, 325, 326, 329, 330]

By measuring the propagator one can study the molecular migrations over distances that either are shorter than the characteristic pore size or are of the order of several pore sizes.[331, 332] At short Δ, the propagator corresponds to the molecular motions inside individual pores [333] and characterises the instantaneous velocities of a random, steady-state fluid flow [331, 334] as well as diffusive molecular displacements.[182] In the short-time limit (at $\Delta \to 0$) the contribution of the diffusive displacements is predominant. In contrast to this, at long Δ, where the fluid flow causes the molecules to be displaced over distances of the order of several pore sizes, measurements of the propagator allow the determination of the average molecular displacements and studies of the hydrodynamic dispersion.[318]

The effective dispersion coefficient can also be defined at short Δ. For an exponential velocity correlation function of the form

$$R_u(t) = \langle u(0)u(t)\rangle = \langle u^2\rangle \exp\left(-\frac{t}{\tau}\right), \quad (30)$$

the effective dispersion coefficient, D', is given by the formula

$$D' = \frac{1}{2}\langle u^2\rangle\Delta \text{ at } \Delta \ll \tau, \quad (31)$$

$$D' = \langle u^2\rangle\tau \text{ at } \Delta \gg \tau. \quad (32)$$

Thus, the dispersion coefficient D' measured along the direction of the net flow ($D_{\|}$) initially increases and then reaches the asymptotic limit as Δ increases.[318] Generally, there is no need to assume a Gaussian shape of the propagator. The average molecular displacement and the dispersion coefficient only correspond to the two lowest moments of the displacement distribution, whereas the propagator provides a complete displacement distribution.[335]

By carrying out experiments with modulation of the field gradient one can determine the frequency spectrum of the fluid velocity autocorrelation function in the frequency range from 10 Hz to 100 kHz. This spectrum is defined as

$$D'(\omega) = \int_0^\infty \langle u(0)u(t)\rangle \exp(i\omega t)\mathrm{d}t \quad (33)$$

and describes the dependence of the hydrodynamic dispersion coefficient (tensor) on the fluid particle motion frequency, ω.[163, 255, 318, 336] The approach allows studies of the frequency spectrum of the particle motions and separation of the contributions of the motions corresponding to different time scales.[163]

The propagator is usually obtained by using the Fourier transform of the echo amplitude, $E(\mathbf{q},\Delta)$, measured at different $\mathbf{q}$ values [see expression (19)]. However, the dispersion coefficient can also be obtained in another manner, by analysing the $E(\mathbf{q})$ dependence in the small $\mathbf{q}$ region (analogously to the diffusion coefficient).[318] In contrast to other methods, dispersion measurements with NMR directly provide the necessary information and do not require solving model equations. They also permit the dispersion coefficient to be measured both along the net flow (pressure gradient) and in the transverse direction.

When measuring the propagator, there is no need of introducing any tracers into the flow since their role is played by the phase of the transverse magnetisation. Another approach to the dispersion studies involves the use of paramagnetic compounds (tracers) and recording the relaxation-weighted NMR images.[137, 337–340] The local concentration of the paramagnetic tracer can be determined from the nuclear spin relaxation time of the fluid.[337, 339]

The most widely used model of filtration is water flow through a cylindrical bead pack. If the beads are sufficiently large, the NMR images of stagnant water in the bead make it possible to visualise individual pores and the inter-pore channels and to analyse the structure of the pore space.[320, 321] Mapping different velocity components allowed one to establish the character of the correlation between the average flow rate (F) through the pore 'neck' and the 'neck' surface area (S). All experimental dependences were found to be intermediate between linear $F \sim S$ (plug flow) and quadratic $F \sim S^2$ (viscous flow).[321] The maximum flow velocities in bead packs much exceed the average velocity,[321, 328] while a large fraction of the fluid flow is confined within a small region of the pore space.[320] Transition to a diffuse fluid flow inside the bead pack occurs at a distance of the order of the bead diameter from the inlet edge.[328] Some indications of reverse flows have been reported.[321] Peculiarities of water flow in a tube in the regions upstream and downstream the plastic bead pack have been studied.[328]

At $d_c/d < 10-15$ (d_c is the diameter of the bead pack and d is the bead diameter), the edge effects play a significant role.[331] The dependences of the average bed porosity and the average flow velocity on the distance from the cylinder wall have been plotted based on the experimental data. The porosity is maximum on the cylinder walls (due to ordering of beads), whereas the flow velocity is maximum at a distance approximately one particle radius thick.[318, 320] Capillary electrochromatography and pressure-driven filtration experiments with bead packs with a small d_c/d ratio confirmed the higher velocity in the near-wall region.[341] Bead packing inhomogeneities were found to affect the fluid flow.

Both versions of measurements of the average propagator (with or without spatial resolution) are widely used in studies of water flow through bead packs. Judicious choice of the field gradient allows one to obtain the propagator for both longitudinal and transverse molecular displacements, while variation of the observation time permits flow studies in different characteristic length scales. If the average molecular displacements are smaller than the characteristic pore size, the longitudinal propagator is asymmetric, centred at zero displacement [187, 331] and exhibits an exponentially decaying wing towards larger displacements.[182, 331] As the observation time increases, the amplitudes of the near-zero peak [187] and of the exponential wing [331] decrease; this is accompanied by the formation of a Gaussian propagator centred at the average longitudinal molecular displacement (see Fig. 4 *b*).[182, 187, 318, 331] At the same time, the average transverse molecular displacements are equal to zero; therefore, the corresponding transverse propagator is centred at zero at any observation time [331] and usually has a Gaussian shape, though a propagator represented by the sum of two Gaussians was observed for an bed of glass beads 290 μm in diameter at small molecular displacements.[331] The first Gaussian curve corresponded to the hydrodynamic dispersion coefficient, which is four-fold greater than the self-diffusion coefficient of water. The amplitude of this curve decreased with an increase in the observation time. The second curve continuously broadened with increase in the average longitudinal displacement.[331] The longitudinal and transverse propagators were also represented as the sums of three curves corresponding to diffusion/dispersion in different length scales and characterised by different diffusion/dispersion coefficients (and different average displacements for axial propagator) and by the observation time dependent relative contributions.[160]

The longitudinal ($D_{\|}$) and transverse ($D_{\perp}$) dispersion coefficients are much larger [342] than the self-diffusion coefficient of the bulk fluid, D_0, with $D_{\|}$ being more than an order of magnitude larger than $D_{\perp}$.[182] For instance, water flow through a pack of glass beads 3 mm in diameter at Pe = 1570 (Pe = vl/D_0 is the Peclet number, where v is the average velocity and l is the characteristic pore size) and Re = 3 is characterised by $D_{\|} = 3000\,D_0$ and $D_{\perp} = 80\,D_0$.[187]

The experimentally measured values were found to be dependent on the time [331] and spatial [343] averaging scales. The average molecular velocity and $D_{\|}$ reach the limiting values at $\Delta \sim 20\,d/v_z$, while for $D_{\perp}$ this occurs [160] at $\Delta \sim (5-10)\,d/v_z$, the D' value increasing with the average velocity.[125, 318] As the volume (layer thickness) included in the averaging increases, a predicted fluctuation of $D_{\|}$ occurs.[343] The calculations also predict a decrease in $D_{\|}$ on further increase in the layer thickness. Spatially resolved measurements of the propagator for inhomogeneous samples exhibit the spatial inhomogeneity of the velocity and dispersion distribution.[318] A number of models for the description of the propagators measured in the filtration experiments have been proposed.[333, 343, 344]

Slowing down the net mass transfer due to diffusive mass transfer inside porous granules is an important dispersion mechanism for the beds comprised of porous beads.[182] Here, the longitudinal and transverse propagators are described by the sum of two Gaussian curves. One curve is centred at zero displacement and corresponds to diffusion in the bead pores, which allows the determination of the tortuosity factor of the pore

space.[182, 342, 345] The other curve corresponds to the fluid moving in the intergranular space,[342, 345] which makes it possible to calculate the average flow velocity (for the longitudinal propagator). With the known fluid flow rate one can find the porosity of the bed if the observation time is not too long.[182, 345]

In the experiments with beds comprised of porous beads the variations of the average flow velocity and observation time affect variations of the propagator in different manners. An increase in the flow velocity has virtually no effect on the contribution of the fluid confined inside the pores.[331, 342, 345] At the same time, an increase in the observation time causes the amplitude of the first Gaussian curve to decrease due to water exchange between the pore volume and the intergranular space, thus allowing the exchange dynamics to be studied.[182, 331, 342, 345, 346] In the long-time limit, the average longitudinal and transverse propagators characterise only the flow contribution; which allows the determination of the overall porosity of the system (layer + beads).[182]

Sometimes, an analogous picture was also observed for water flowing through a non-porous bead (granule) pack (see Fig. 4 *b*).[318] The component of the propagator centred at zero molecular displacement is thought to correspond to stagnant water present at intergranular contacts. For smaller granules, the characteristic size of these 'pools' is also smaller and the contribution of the immobile fluid decreases faster with increasing the observation time.

Studies of the frequency spectrum $D(\omega)$ of transverse molecular motions for a fluid flowing through a bead pack revealed the presence of three components of the molecular displacements: (i) Brownian motion, (ii) coherent oscillatory motion relative to the bead pack axis due to curvilinear flow around the beads and (iii) random perfusive walks. The experimental spectra, $D(\omega)$, exhibit a characteristic maximum, which is shifted towards higher frequencies with increasing the flow velocity and corresponds to coherent oscillations. A high-frequency plateau $D(\omega) = D_0$ corresponds to diffusive motions, while the low-frequency plateau, which decreases with increasing the flow velocity, corresponds to random perfusive motions.[163]

Measurements of the propagators $P(\mathbf{R}_1,\Delta_1;\mathbf{R}_2,\Delta_2)$ characterising the mutual probability density of a molecular displacement over distance $\mathbf{R}_1$ over time Δ_1 and over distance $\mathbf{R}_2$ over time Δ_2 (including the VEXSY and SERPENT experiments) permit studies of the spatial and time correlations of flow velocity fluctuations.[283, 318, 347] In particular, this approach was employed in comparing fluid flows in disordered and ordered porous media.[347] In some instances the spatial velocity correlation can also be calculated from the spatial velocity distribution maps.[337]

Molecular motions in a periodic system of identical pores can be accompanied by the appearance of coherence effects. For instance, experiments with water flow through a bead pack revealed flow-dependent diffraction-like effects manifested as a maximum in the plot of the dependence of the echo amplitude, E, on q near $q = 1/d$ (d is the bead diameter). Simulation of the results obtained allowed the determination of the longitudinal hydrodynamic dispersion coefficient, average inter-pore distance and the pore sizes. The peak indicates that the molecular displacements are correlated in the bead-diameter length scale.[125, 318]

Interest in the flow of gases, fluids and suspensions through porous rocks is first of all related to the gas and oil recovery. For most of rocks mapping the pore space using the MRI technique is impossible. At the same time, the amplitude of the NMR signal from a fluid-filled core depends on the local porosity of the core.[325] The Darcy relation connects the flow velocity to the medium permeability, thus allowing establishment of a correlation between the local porosity and permeability.[330]

The flow velocity distribution maps obtained for water, brine[326, 329, 330] or a mixture of aliphatic hydrocarbons[325] in sandstone cores were converted into corresponding velocity histograms and it was found that the flow velocity increases almost linearly with the medium porosity.[330] The velocity distribution obtained for a layered core with bimodal pore size distribution was found to be nearly Gaussian.[330] A correlation between the hydrodynamic dispersion coefficient and the average flow velocity has been observed.[329]

The flow velocity maps obtained for identical flow rates were shown to be different if the flow rate was altered in between the measurements.[329] To explain this, a stochastic theory of flow through a porous medium has been proposed.[329]

Similarly to model bead packs, at short observation times the longitudinal (along the pressure gradient) propagator obtained for the fluid in the sandstone core is centred at zero displacements and exhibits a wing decaying towards larger displacements; as the observation time increases, the propagator approaches a Gaussian curve.[333, 334] The transverse propagator has a Gaussian shape, is centred at zero displacement and broadens with the delay time.[333] Measurements of the 2D propagator revealed correlations between the longitudinal and transverse molecular displacements.[334]

Filtration of colloidal suspensions are of great practical value for borehole drilling. When using drilling fluids, clay permeates the pores of the surrounding rock, which affects the drilling efficiency and the operating performance of the borehole. Large surface area of suspended clay causes substantial variations of the T_1 time of the fluid, which allows one to follow the clay accumulation in the pores.[348–350] The maximum penetration depth of clay into the core is less for the cores with lower permeability[348, 350] and is reached after relatively short times. Further injection of clay suspension has no effect on the penetration depth.[348–350] For highly permeable limestone the process is accompanied by substantial porosity reduction.[350]

Filtration is accompanied by deposition of a layer of increased concentration of retained molecules, particles or droplets on the filter surface. Measuring the dependence of the spin relaxation time of the fluid on the pore size allowed the determination of the spatial porosity distribution in the dense deposit layer during pressure-driven filtration of aqueous clay suspension.[351]

Considerable attention has been given to the multicomponent flows and displacement of particular components. These processes occur when cleaning contaminated soils and are of interest from the standpoint of improving the extraction of petroleum content from rocks. By selecting the contribution of a particular component to the NMR signal one can obtain, *e.g.*, the distribution of water (brine) and oil in the sample throughout the displacement process.

A number of studies on the displacement of oil (hydrocarbon) by pumping water through oil-saturated cores[322, 323, 352–354] or granular beds[355] has been reported. Water ingress into cores occurs in the form of jets, the characteristic size of which is much less than the spatial resolution achieved in the experiments.[353] As a result, water rapidly permeates into the sample; however, the process is not accompanied by substantial displacement of oil and the formation of a sharp interface between the two fluids. As time passes, a gradual displacement of oil by water occurs uniformly throughout the sample. A fraction of oil is retained within the sample after pumping a large amount of water, which was confirmed by recording the water and residual oil distribution profiles.[352, 353, 355] Water poured in a cavity of a porous thimble-shaped ceramic sample pre-saturated with C_6F_6 causes the hydrocarbon to be displaced uniformly across the sample section,[49] which was confirmed by recording 2D NMR images using the ^{19}F NMR signals.

Displacement of water from various cores[323, 324, 353, 356] or a granular bed[355] by pumping oil has been studied. The process is accompanied by the formation of a clearly visible interface between the two liquids.[353, 355] The residual water content in the core strongly depends on the oil flow rate.[324] For a sample with the axial bedding planes different porosity and permeability of different layers led to different displacement rates.[323] Displacement of oil and water by isopropyl alcohol has been studied.[352]

The propagators for flowing water or oil at different residual content of oil (water) in the core [334] and for two-phase flow of water and dodecane [334, 357] have been measured.

The presence of a contaminant (residual content of a poorly soluble fluid) confined inside the pores of a medium can be responsible for prolonged poisoning of water pumped through the medium. Displacement of n-hexanol by water from a sand layer was studied by recording the n-hexanol distribution profiles.[358] The behaviour of individual octanol droplets during the displacement process was followed by using a pack of large beads (3 – 5 mm).[359] Recording the velocity distribution maps showed that a fraction of droplets distant from the fast jet flow is removed very slowly. An increase in the water pumping rate and a decrease in the droplet size led to faster removal of the contaminant. A number of numerical simulations of the process has also been reported.[358, 359]

Experiments on simultaneous filtration of water and air through a bead pack showed that their distribution in the layer remains inhomogeneous for a rather long time after starting the flow (2 h). It was also found that a nine-fold increase in the water flow rate after establishing the steady-state flow leads to a redistribution of the fluid and gas in the layer, whereas an eight-fold increase in the gas flow rate causes only insignificant changes.[320, 360]

Filtration induced dispersion can also be studied by introducing paramagnetic tracers into the flow and following the movement of the tracer concentration front in the porous medium. The presence of inhomogeneities in the bead pack or core cause a significant increase in dispersion of the tracer concentration front.[137, 337, 338] A study of the dispersion coefficient in a pack comprised of large beads showed that the tracer concentration front oscillates with a spatial period equal to the bead size due to the flow velocity fluctuations occurring with the same spatial period. This behaviour was confirmed by model calculations using a 2D grid of cylindrical pores with variable cross-sections.[339]

Secondary convective flows due to the gravity force are of significant importance if the bead pack is arranged vertically and the fluids to be mixed have different densities.[344] Bottom feed of a more concentrated Mn_2(EDTA) solution (EDTA is ethylenediaminetetraacetic acid) causes a uniform movement of the concentration front along the flow direction. The injection of the solution from the top leads to a parabolic front accompanied by its convective spreading. Flow direction reversal experiments showed that dispersive spreading of the concentration front is fully irreversible in the former case and partially reversible in the latter (a pack of 2 mm beads was studied). When 8 mm beads were used, a flow instability was observed, accompanied by fast dispersion of the concentration front along the full length of the bead (22 cm).[344] It was found that a density gradient causes convection in stagnant fluid. A study of inhomogeneous bead pack with the top part filled with brine and the bottom part filled with water showed that advective fingering is observed first in the region with a higher permeability and later — in the rest of the bead pack.[338]

The movement and transformations of the concentration front in chromatographic and ion-exchange columns have been studied.[340, 361, 362] Because of the high velocity of movement of the concentration bands, investigations of high-pressure chromatography processes require the use of fast NMR imaging techniques. This allowed visualisation [340, 361] of the movement of Gd(DTPA) solution (DTPA is diethylenetriaminepentaacetic acid) with a velocity of up to 1 mm s^{-1} at an external pressure of nearly 55 atm. At pH 6 of the liquid phase, a compact concentration band was found to move through a column filled with silica gel without changes in its shape with time. However, an analogous process at pH 7 was accompanied by appreciable band broadening and a change in the shape. NMR images also allow one to assess the packing character of the stationary phase in the column. In particular, in columns with the slurry packed stationary phase the packing gradient of the solid phase induced a gradient of the spin relaxation times of the fluid throughout the height of the column.

Experiments with a chromatographic column in the form of the bed of polystyrene beads swollen in THF (bead diameter: 100 μm) showed [49] that a fluoro derivative of glycine poured onto the bead pack surface moves down the column right to the bottom without retention in the polystyrene microcavities.

Processes in a column loaded with ion-exchange resin (Na^+ form) were studied by recording the NMR images using the ^{23}Na NMR signal. The movement of the free Na^+ ion concentration front down the column during successive elution with aqueous HCl solution, aqueous NaCl solution and water was followed.[340, 361]

5. Motion of granulated materials

The NMR imaging technique is also used in the investigations of the motion of solid granulated materials, when optical methods are inapplicable because of opaqueness of the objects under study. Experiments are carried out with liquid-containing solid particles, such as liquid-containing pharmaceutical pills, mustard and poppy seeds and porous granules partially saturated with liquid. Segregation of granulated materials can be studied using their mixtures with solid particles that are 'invisible' to NMR.

The motion of solid particles in rotating cylinders is widely used in grinding, granulation, mixing and drying of solid granulated materials and in coating processes. When the cylinder is full, rotation of the entire sample allows estimation of the accuracy of the particle concentration and particle velocity distributions obtained in the experiments.[253] The NMR images of a half-filled horizontal cylinder show different regimes of the particle motion depending on the rotation rate.[253] The oblique surface of the granular bed exhibits a clearly visible layer with a reduced average density of the 'flowing' particles, the layer thickness being dependent on the rotation rate. A density gradient due to the dynamic particle packing effects was also observed in other regions of the granular bed.[253] The dynamic angle of repose at different rotation rates was measured [254] and the spatial particle velocity distribution maps in the cylinder were obtained.[253, 254, 265]

Experiments aimed at determining the correlation time of the particle motion, τ, the autocorrelation velocity function [expressions (20) and (21)] and the diffusion coefficient D for the axial motion of particles in a rotating cylinder have been carried out.[265, 279] It was found that the effective axial diffusivity is maximum near the foot of the sliding particle layer [254, 279] and is different at different distances from the surface.[279] The characteristic τ values lie in the millisecond range, the D are three orders of magnitude higher than the self-diffusion coefficient of water [265] and the mean square of velocity fluctuations, $\langle u^2 \rangle$, exceeds 10^{-3} m^2 s^{-2} (see Ref. 279). The experimental values of the dynamic angles of repose, and the spatial maps of concentration, velocity and diffusivity values obtained for solid granules are in good agreement with the results of calculations.[254]

Often, relative motion of particles with different properties (size, density, shape) causes spontaneous segregation of mixtures. Nearly immediately after a cylinder filled with a well-mixed mixture of particles of different sizes starts to rotate, radial segregation occurs, accompanied by an increase in the concentration of smaller particles near the axis of rotation.[363] As the cylinder continues to rotate, radial segregation evolves into an axial segregation until complete segregation of the mixture into several layers comprised of the particles of different size, which follow one another in the axial direction.[363] For a binary mixture the trends to segregation due to different particle size and density can be mutually compensated.[364] If the system is described in the 'particle size' – 'particle density' coordinates, there is a boundary corresponding to good mixing, whereas moving away from the boundary causes greater segregation.

To intensify the motion of solid particles, vibration is often used. For instance, a study has been reported of the motion of beads 2 mm in diameter placed in a container attached to a lever,

the long arm of which was connected to a loudspeaker.[365] The amplitude of the oscillations of a specified frequency (20 – 25 Hz) supplied to the loudspeaker increased until a value at which arching was observed using a stroboscope. The amplitude of container displacements was ~ 0.5 cm. Alternating left-right arching has been studied. The 2D NMR images of the vibrating layer at different instants of the oscillation period exhibited the effect of doubling the oscillation period. The layer edges execute an out-of-phase motion: when one edge is at the top, the other is at the bottom, and *vice versa*. The largest shear deformation was observed in the middle region of the layer, which always moves from the elevated towards the lowered edge of the layer.

Convection in a particle layer placed in a periodically shaken cylindrical container has been studied by recording the NMR images.[366] Transformation of the shape of spatial tags illustrated an upward motion of the particles near the axis of the cylinder and a downward motion near the walls, the velocity on the walls being maximum in absolute value. Except for the near-surface region, the velocity of the motion exponentially decreases with increase in the depth.[366] The propagators for the vertical particle displacement at different shaking frequencies and amplitudes have been obtained.[335]

The gravity driven filtration of a fine-grained granulated material through a pack of larger beads, simulating a catalytic reactor, has been studied.[8] The 2D NMR flow velocity maps of the material exhibited a flow not only near the walls, but also in the bulk of the bead pack. The propagators characterising the flow velocity distribution of small granules have also been obtained.

6. Gas flow

Gases have large diffusion coefficients as compared to liquids. Because of this, one can expect that the diffusive displacements of gas molecules contribute largely to the net displacement over the observation time. This seems to be the reason for weak interest in the application of the MRI technique to gas flow studies until recently. However, recent advances in this field [93, 217, 367, 368] are thought to give an impetus to intensive research on gas flow. In particular, visualisation of the flow of gaseous hydrocarbons [93, 367] can be useful in the MRI studies of heterogeneous catalytic processes.

The potentialities of the NMR imaging technique in the studies of the flow of gases with equilibrium spin polarisation in moderately strong magnetic fields (7 T) have been illustrated taking acetylene, propane and butane flowing in a circular cross-section tube or in transport channels of a monolithic catalyst as examples.[93, 367] The longitudinal velocity distribution maps obtained for a developed laminar butane flow in a tube exhibit a parabolic radial velocity distribution (Fig. 5 *a*). The propagator measured under the same conditions virtually coincides with the velocity histogram constructed based on the velocity distribution maps. As the observation time becomes sufficiently long for diffusive molecular displacements over a distance of the order of the tube diameter to occur, the rectangular propagator changes into a Gaussian one due to the Taylor dispersion.

It was also found that laminar gas flow can be visualised using the spatial tag technique, which exhibits transformation of a linear tag created normal to the flow direction into a parabolic tag. At the same time, as the Reynolds number approaches the critical value, the NMR signal amplitude rapidly attenuates below the noise level, which precludes investigations of the transition to turbulent flow and a developed gas turbulence.

Nevertheless, the MRI technique can be applied to studies of not only developed laminar flows, but also establishment of a developed gas flow through the entrance region of a tube or channel. The MRI velocity distribution maps for the gases flowing through a tube into a cylinder of a larger diameter, containing a fragment of a monolithic catalyst, at Re = 190 – 570 have been obtained (see Fig. 5 *b*). In this case the velocity distribution across the transport channels is significantly different from analogous

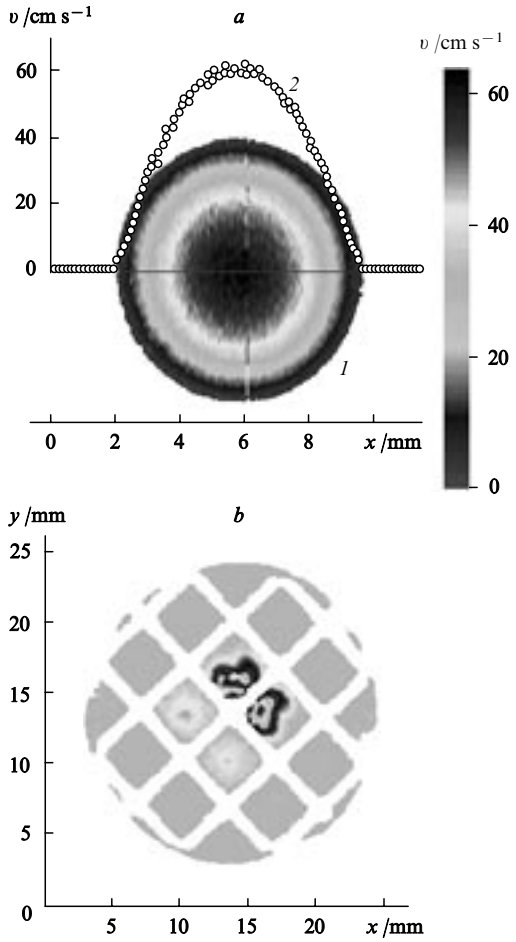


Figure 5. Visualisation of butane flow by the phase contrast technique.[2] Two-dimensional velocity map (*1*) and its one-dimensional cross-section (*2*) for a laminar gas flow in a tube with a circular cross-section; the velocities for the two-dimensional map are given at the right, those for the one-dimensional cross-section are given at the left (*a*); velocity map for butane flowing into a cell of a monolithic catalyst (cell diameter: 21 mm) with 4 mm square channels (*b*).

distribution for a completely developed laminar flow. In particular, inhomogeneous shear rate distributions across the channel cross-sections are observed. This is in agreement with the estimates of the entrance length, which exceeded the distance from the inflow edge of the monolith to the NMR image plane.[93, 367]

Studies of gas filtration through porous materials are of considerable interest. As mentioned above, spatially resolved MRI techniques are of limited use even for liquids. Typical of gases with equilibrium polarisation is a low signal-to-noise ratio, which makes this approach of little promise. In this connection, it is of interest to use the average propagator approach in gas filtration studies. For instance, the propagators for longitudinal and transverse displacements of gas molecules in a porous medium have been obtained for a cylindrical glass bead pack (Fig. 6). By and large, transformation of the propagators with increasing Δ is similar to those observed for the filtration of liquids. At short Δ, a broad (due to high gas diffusion coefficient) Gaussian propagator centred at zero displacement is observed. As Δ increases, a wing appears in the large displacement region and then a Gaussian propagator is formed, which is centred at the average molecular displacement. The width of the propagator is determined by the gasodynamic dispersion coefficient. Despite high gas diffusion rates, the experimental longitudinal and transverse dispersion coefficients are much larger than the self-diffusion coefficient D_0 ($D_0 = 0.03$ cm^2 s^{-1} for butane at a pressure of

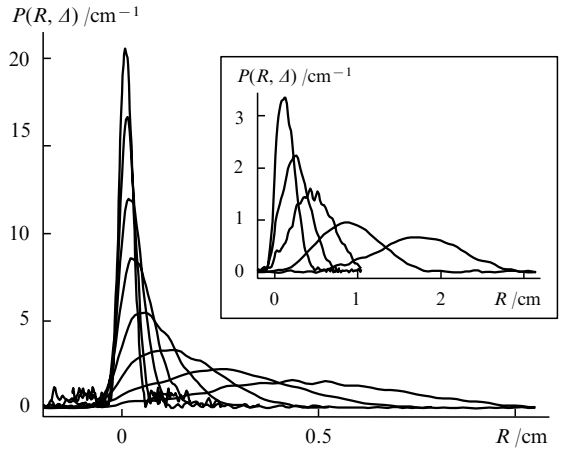


Figure 6. Averaged propagator for axial displacement of butane molecules flowing through a cylindrical glass bead pack (bead diameter: 3.2 mm; bead pack diameter: 21 mm). Observation time: Δ = 1, 2, 5, 10, 20, 40, 80, 150 ms (the corresponding curves are plotted from top to bottom).
The inset presents the data for Δ = 40, 80, 150, 300 and 600 ms.

1 atm and room temperature). The dependence of the dispersion coefficient on the observation time, flow velocity and bead size has been studied. The VEXSY experiments were also carried out, which allowed one to follow the loss of molecular velocity correlation in the pack with increasing the observation time in spite of a rather large diffusive contribution.

Experiments with hyperpolarised gases [369–372] permit substantial improvement of the signal-to-noise ratio compared to that obtained for gases with equilibrium polarisation. In particular, this makes it possible to achieve a rather high spatial resolution when recording the NMR images using the NMR signal from the gas molecules in macroporous materials. However, acceleration of the spin relaxation of the gas in the pores of the medium can sacrifice the advantages of using hyperpolarised gases in the studies of filtration through many materials.

Xenon flow was investigated using a system with continuous circulation of polarised ^{129}Xe, which allowed enhancement of the magnetisation by more than three orders of magnitude compared to the equilibrium ^{129}Xe polarisation at the same magnetic field (4.2 T).[217, 368] The 2D images in the mixed k, q-space (propagator with spatial resolution along one coordinate) were obtained in dynamic MRI experiments. Studies of xenon flow in a round tube [217] at different observation times Δ revealed that Taylor dispersion due to lateral molecular diffusion causes the gasodynamic dispersion coefficient initially to increase with increase in the delay time and then to reach a plateau at delay times that are longer than the characteristic time of molecular diffusion over a distance of the order of tube diameter.

A feature of xenon flow in a tube with a diaphragm having a small opening at the centre is flow acceleration at the tube axis and the reverse flow in the near-wall regions as a result of flow turbulence.[368] Analogous studies were also carried out for parallel xenon flow through two polyurethane foam samples with pores 400 and 200 μm in diameter. The velocity distribution maximum was found to be shifted towards higher velocities for the material with a lower density and larger pores.

Application of MRI to gas filtration studies allows the local permeability of porous samples to be determined. If the porous material does not adsorb a gas, the signal amplitude in the NMR image is proportional to the local gas pressure, whereas the viscosity of an ideal gas is pressure independent. Knowledge of the velocity field permits calculations of the spatial distribution of material permeability using the Darcy equation. In this case, carrying out the 1D experiments does not require gas velocity measurements.[373]

* * *

When studying various mass transfer processes, a detailed picture of a particular process can be obtained only when using modern physicochemical methods that allow spatially resolved measurements. Numerous examples presented in this review demonstrate that MRI is an efficient tool for studying such processes. The authors hope that this information will be of use to those dealing with mass transfer problems in various fields of science and technology.

This review has been written with the financial support by the Russian Foundation for Basic Research (Project Nos. 02-03-32770 and 00-15-97450) and the Siberian Branch of the Russian Academy of Sciences (the 'Integration' Programme Project No. 46).

VII. Supplement

In Table. S.1 we present additional information on the MRI studies of mass transfer processes.

Table S.1. Applications of the MRI techniques.

Field /T	Object, process	Technique	Dimension	Spatial resolution characteristics	Recording time	Nucleus	Ref.
0.78	water in fired clay	spin echo	1D	0.17–1 mm, a cylinder 20 mm in diameter	–	^{1}H	2–4
4.7	H_2O or D_2O in concrete of various composition	spin echo or SPI	2D	64 × 128; a slice 25 mm thick (spin echo)	6 min (SPI)	^{1}H (SPI), ^{2}H (echo)	5
5.5	5% methanolic solution of alkylalkoxysilane in hardened mortar	STRAFI + dipolar (solid-state) echo	1D	100 μm	–	^{1}H	6
0.7	water in gypsum, limestone and mortar	–	1D	< 2 mm	5 min	^{1}H	9
2	water in limestone	spin echo	2D	128 × 128	40 s	^{1}H	10
0.8	water in hardened mortar prepared from Portland cement and silica sand	the same	1D	0.9 mm, a cylinder 20 mm in diameter	–	^{1}H	11

Table S.1 (continued).

Field /T	Object, process	Technique	Dimen-sion	Spatial resolution characteristics	Recording time	Nucleus	Ref.
0.78	aqueous NaCl solution in a calcium silicate brick	spin echo	1D	0.25 mm (2 mm), a cylinder 20 mm in diameter	–	^{1}H, ^{23}Na	12
2.35	water in hardened cement with clay additive (sodium aluminosilicate) and PVA	–	2D	40 μm, a slice 0.35 mm thick	–	^{1}H	13
0.7	water in sandstone cores	gradient echo with oscillating gradients	1D	0.4 mm, a cylinder 25 mm in diameter	5.5 s	^{1}H	14
0.5	decane in peroxide vulcanised natural rubber	the same	2D	250 (400) μm for decane, 600 μm for rubber, a slice 5 mm thick	20 min	^{1}H	21
2.4	water in zeolite 4A	SPRITE	1D	64 points, 0.55 mm	< 2 min	^{1}H	22
0.7	the same	gradient echo with oscillating gradients	1D	–	few seconds	^{1}H	23
2.0	n-hexane in zeolite NaX	stimulated echo	1D	0.3 mm	2 min	^{1}H	24
1.4	butane in zeolites NaCaA, water in zeolite NaX	FID	1D	0.5 mm	–	^{1}H	25
2.0	n-Hexane in zeolite NaX	stimulated echo	1D	0.3 mm	2 min	^{1}H	26
2.35	water in soil (humus)	spin echo	2D	128 × 128 or 256 × 256, $(0.47\ mm)^2$ or $(0.35\ mm)^2$, a slice 20 mm thick	–	^{1}H	27
7.05	acetonitrile, benzene, dichloromethane and CCl_4 in carbonaceous adsorbent	FID	–	WSR	–	^{1}H	28
7.05	water in copolymer of 2-hydroxyethyl methacrylate and tetrahydrofurfuryl methacrylate	spin echo	3D	128 × 128 × 8, 78 μm × 78 μm × 3.75 mm	35 min	^{1}H	29
7.05	vulcanised *cis*-1,4-poly-butadiene + cyclohexane-d_{12}	the same	2D	256 × 256, $(37\ \mu m)^2$ or $(58\ \mu m)^2$, a slice 1 mm thick	–	–	30
7.05	vulcanised polybutadiene rubber + deuterocyclo-hexane or cyclo-hexane-d_{12}	"	2D	256 × 256, $(39\ \mu m)^2$ or $(32\ \mu m)^2$	–	–	31
2	acetone in vulcanised rubber	"	1D	128 points, 100 μm a slice of 0.5 cm^2 surface area	32 s	^{1}H	32
–	hot water (100 °C) in nylon-6,6	steady-state free spin precession (SSFP)	1D	240 μm	–	^{1}H	33
9.4	1,4-dioxane in PVC	spin echo with inversion – recovery	2D	$(70\ \mu m)^2$, a slice 4 mm thick	–	^{1}H	35
9.4	acetone or acetone + methanol in bisphenol A polycarbonate	the same	2D	$(70\ \mu m)^2$, a slice 4 mm thick	–	^{1}H	35
2.35	toluene in butadiene rubber, hexafluoro-benzene in methylsil-oxane rubber, methanol in PEMA, pyridine in bituminuous coal	spin echo	2D	128 × 128, $(70\ \mu m)^2$	10 min (^{1}H), 30 min (^{19}F)	^{1}H, ^{19}F	36

Table S.1 (continued).

Field /T	Object, process	Technique	Dimen-sion	Spatial resolution characteristics	Recording time	Nucleus	Ref.
2.35	pyridine in bituminous coal, methanol in PEMA, toluene in isobutyl rubber	–	2D	128 × 128, $(40\ \mu m)^2$	10 min	^1H	37
7	CH_3OD in PMMA	gradient echo (FLASH)	2D, 3D	200 μm	–	^1H	38
7	acetone or CH_3OD in PMMA	spin echo	2D	256 × 256, a slice 2 mm thick	–	^1H	39
7	CH_3OD in water-soaked PMMA	gradient echo (FLASH)	2D	256 × 256, $(100\ \mu m)^2$, a slice 1 mm thick	10 min	^1H	40
–	toluene or trichloro-ethylene in PVC; n-pentane in high-density polyethylene	B_1-imaging	–	–	–	^1H	41
4.7	toluene in PVC, acetic acid in cellulose, n-pentane in polystyrene	the same	2D	256 × 128 points (512 × 512)	2 h	^1H	42
7	acetone or methanol (CH_3OD) in PMMA	spin echo or gradient echo (FLASH)	2D	256 × 256, $(140\ \mu m)^2$, a slice 500 μm thick	–	^1H	43
9.4	methanol in PMMA	spin echo	2D	$(70\ \mu m)^2$, a slice 4 mm thick	–	^1H	44
4.7	dioxane in polystyrene–divinylbenzene copolymer	gradient echo (FLASH)	2D	256 × 256, $(115\ \mu m)^2$, a slice 1.5 mm thick	2 min	^1H	45
4.7	rubber + benzene-d_6, cross-linked nematic liquid-crystalline prepolymer + CD_2Cl_2, poly(*N*-isopropylacrylamide) + H_2O/D_2O + CH_3OD	spin echo	1D, 2D	a slice 500 μm thick (2D)	–	^1H	46
7	acetone-d_6 + CH_3OD or acetone + CD_3OD in bisphenol A polycarbonate	gradient echo (FLASH)	2D	256 × 256, $(100\ \mu m)^2$, a slice 1 mm thick	25 min	^1H	47
2	acetone + benzene in vulcanised rubber	chemical shift selective spin echo	2D	a slice 4 mm thick	2 min	^1H	48
2	isooctane in vulcanised rubber saturated with cyclohexane	gradient echo for two-quantum coherence	2D	a slice 8 mm thick	8 min	^1H	48
4.7	C_6F_6 or C_6F_6 + C_6H_6 in polystyrene	gradient echo (FLASH)	2D	256 × 256, $(120\ \mu m)^2$, a slice 1.7 mm thick	310 s	^{19}F	49
4.7	C_6F_6 + water in porous ceramics	spin echo	2D	256 × 256, $(80\ \mu m)^2$, a slice 2.8 mm thick	34 min	^{19}F	49
4.7	fluoro derivative of glycine + THF in cross-linked polystyrene bead pack	the same	2D	256 × 128, 135 × 270 μm	70 s	^{19}F	49
0.5	decane in peroxide vulcanised natural rubber	gradient echo with oscillating field gradients	2D	250 (400) μm for decane, 600 μm for rubber, a slice 5 mm thick	20 min	^1H	50
4.7	H_2O and/or D_2O in PEO	spin echo	1D	512 points, 29.3 μm	–	^1H	51

Table S.1 (continued).

Field /T	Object, process	Technique	Dimension	Spatial resolution characteristics	Recording time	Nucleus	Ref.
0.1, 2.9	water in sodium polyacrylate	spin echo + STRAFI	1D	–	16 s or 12 min (STRAFI)	^{1}H	52
9.4	adsorption of water vapours into $M(CF_3SO_3)_2(PEO)_n$ films (M = Pb, Zn; n = 9, 16, 24)	spin echo	1D, 2D	40 μm (50 – 200 μm), a slice of 400 μm × 9 mm surface area (1D), (40 μm)^2, a slice 400 μm thick	1 min (1D), 20 min (2D)	^{1}H	53
9.4	adsorption of acetone vapours into poly(vinyl chloride)	dipolar echo + STRAFI	1D	78 μm, a slice of (10 mm)^2 surface area	–	^{1}H	54
2	adsorption of $CDCl_3$ or CCl_4 vapours into PMMA or polystyrene	recording FID amplitude after selective pulse	1D	0.5 mm	–	^{1}H	56
	sorption of water or water vapours into corn starch amylose	STRAFI	1D	80 points, 50 μm	20 min	^{1}H	57
9.4	pyridine-d_5 or acetone-d_6 in coal	spin echo	2D	128 × 128, (78 μm)^2	7 min	^{1}H	58
0.83	water at 93 °C in glass fibre reinforced epoxy resin based on bisphenol – acetone	PRI	2D	256 × 256, a sample 5 – 7 cm thick	15 min	^{1}H	59
7	1,4-dioxane in polybutadiene rubber	spin echo	2D	a slice 2 mm thick	–	^{1}H	60
2	water in natural rubber or in partially epoxidised rubber, cyclohexane in vulcanised rubber	the same	3D	128 × 128 × 8, a slice 2 mm thick	–	^{1}H	61
4.7	acetone, DMSO or pyridine in coal	"	2D, 3D	256 × 256, (500 μm)^2, a slice 1 mm thick (2D); 128 × 64 × 64, (200 μm)^3 (3D)	2 min (2D), 15 min (3D)	^{1}H	62
2.35	pyridine or pyridine-d_6 in coal	gradient echo or PRI	3D	128 × 128 × 128, (40 μm)^3 (echo); (80 μm)^3 (PRI)	16 or 42 h (echo); 22 h (PRI)	^{1}H	63
7	CH_3OD in PMMA	spin echo	2D	256 × 256, (68 μm)^2, a slice 2 mm thick	51 min	^{1}H	64
11.7	PVA pellet in water	the same	1D	256, 29 μm	40 s	^{1}H	65
9.4	water in hydroxypropylmethylcellulose	"	1D	128, 156 μm	3 min	^{1}H	66
4.7	water in silicone matrix + NH_4F	"	2D	(0.25 mm)^2, a slice 0.6 mm thick	3 h	^{1}H	68
9.4	polyhydroxyalkanoate film	"	2D	256 × 256, (117 μm)^2	15.5 h	^{1}H	69
2.4	water in Portland cement	SPI	–	128 points, 0.7 mm	13 min	^{1}H	70
4.7	vulcanised rubber impregnated with aluminium and sodium sulfate crystals, filled phenolic resin or a 72-h tobacco horn worm	spin echo, PRI	–	180 FID, (35 μm)^2 (PRI); 128 × 128, a slice 1 mm thick or without slice selection	2 – 17 h	^{1}H	71
2.9	water in Portland cement with gypsum and lime additives	dipolar echo + STRAFI	1D	100 μm	–	^{1}H	78

Table S.1 (continued).

Field /T	Object, process	Technique	Dimen-sion	Spatial resolution characteristics	Recording time	Nucleus	Ref.
2.4	water in concrete	SPI	–	128 points, 0.95 mm	12 min	^{1}H	79
0.7	layered polymer composite model sample or alkyd resin film with cobalt catalyst	spin echo	1D	256 or 512, 13 or 6.5 μm	17 min	^{1}H	80
0.7	alkyd resin-in-water emulsion	spin echo	1D	128, 8.7 μm	–	^{1}H	81
2	water in sodium silicate film	dipolar echo + STRAFI	1D	100 μm	1 – 2 h	^{1}H	82
2.4	water in Portland cement	SPI	1D	0.95 mm	–	^{1}H	83
2.35	water in concrete	SPRITE	1D	64; 1.6 mm	–	^{1}H	84
2.35	agar gel doped with Mn(II), mortar, concrete or polyethylene	SPRITE	2D	64 × 64, (1.25 mm)^2 – (1.5 mm)^2	–	^{1}H	85
7.05	water in Portland cement with or without superplastifier	SPI	2D	64 × 64 or 124 × 64, 101 μm × 140 μm	–	^{1}H	86
0.75	water in clay brick, lime-and-sand brick or gypsum	spin echo	1D	0.15 mm	40 min	^{1}H	87
0.1	water in limestone	gradient echo	3D, 1D	128 × 128 × 16, 2 × 2 × 8 mm (3D); 2 mm, a slice of surface area 10 × 10 cm (1D)	26 min (3D)	^{1}H	88
4.7	water in alumina or silica	the same	2D	a slice 1 mm thick	–	^{1}H	89
4.7	water in glass bead pack	spin echo (Hahn echo, EPI or PEPI)	2D, 3D	128 × 128; (94 μm)^2, a slice 0.5 mm thick (2D); 128 × 128 × 128, (117 μm)^3 (3D)	51 min or 24 s (2D); 9 h or 15 min (3D)	^{1}H	94
2	water or aqueous solution of sodium dodecylsulfate in glass bead pack, sand, silica gel, potato starch	spin echo	1D	a slice 5 mm thick	–	^{1}H	95
9.4	dispersion of acryl or polystyrene latex in water	the same	2D	512 × 512, (43 μm)^2, a slice 2 mm thick	8.5 min	^{1}H	97
9.4	emulsion of alkyd resin in water, aqueous dipersion of acryl latex	"	2D	512 × 512, (20 μm)^2, a slice 0.5 – 1 mm thick	7 – 51 min	^{1}H	98
9.4	water in composite liquid packaging cardboard	"	1D, 2D	128, 15.6 μm, a slice 2 mm thick (1D); 128 × 16, 15.6 × 500 μm, a slice 8 mm thick	24 s (1D); 2 min (2D)	^{1}H	100
0.5	water in white oak wood	"	2D	256 × 256, (1.2 mm)^2, a slice 8 mm thick	12.8 min	^{1}H	101
4.7	water in corn grains	"	2D	(234 μm)^2, a slice 1.3 mm thick	640 s	^{1}H	105
2	brine in sandstone or limestone	stimulated echo	–	WSR	7 h	^{1}H	117
2	water in glass bead pack, in limestone, chalk and sandstone cores	inversion – recovery signal or stimulated echo	–	WSR	–	^{1}H	118

Table S.1 (continued).

Field /T	Object, process	Technique	Dimen-sion	Spatial resolution characteristics	Recording time	Nucleus	Ref.
2	brine in carbonate rocks and sandstone	stimulated echo	–	WSR	–	^{1}H	121
1.9	C_2F_6 or C_4F_8 in ceramics (yttrium-stabilised zirconia)	spin echo	3D	–	2 h	^{19}F	122
4.7	^{129}Xe (3 atm) in glass cylinder	stimulated echo	–	WSR	–	^{129}Xe	123
8.5	N_2 in zeolites NaCaA and NaX	spin echo	–	WSR	–	^{15}N	124
–	water in polystyrene bead pack	the same	2D, WSR	$(31.5\ \mu m)^2$, a slice 200 μm thick or WSR	–	^{1}H	125
1.5	human brain, rat brain *in vivo*	intermolecular two-quantum coherence + EPI	2D	64×64; $(3.8\ mm)^2$, a slice 15 mm thick (*Homo*) or $(0.48\ mm)^2$, a slice 4 mm thick (rat)	–	^{1}H	133
2	copper ions or 4-amino-TEMPO in water-contain- ing gels	spin echo with inversion – recovery	1D	0.1 – 0.2 mm	–	^{1}H	135
0.2	Fe(II) and Fe(III) ions in agar gel	the same	1D	512, 0.11 mm	28 – 112 s	^{1}H	136
2	copper ions in water-containing polyacryl-amide gel	"	2D	256×256 (128×256), $(0.15\ mm)^2$	150 s	^{1}H	137
2	copper in water-saturated limestone core	"	2D	256×128, $(0.47\ mm)^2$	2.3 min	^{1}H	137
2.35	D_2O in lyotropic liquid crystal	spin echo	–	WSR	–	^{2}H	140
1.4	0.1% $CuSO_4$ + water in capillary	spin echo + PRI	2D	$(20\ \mu m)^2$, a slice 1 mm thick	–	^{1}H	141
5.9	5% polyacrylamide gel in D_2O	stimulated echo	–	WSR	–	^{1}H	145
2	water, acetonitrile, DMSO and n-butanol in ampoules; celery stalk	spin echo	2D	128×128; $(0.34\ mm)^2$, a slice 5 mm thick	–	^{1}H	147
7.05, 11.7	H_2O/D_2O or ethanol/H_2O/D_2O in ampoule	spin echo or stimulated echo	1D, WSR	–	–	^{1}H	148
4.7	water in glass or polystyrene bead pack	stimulated echo	–	WSR	–	^{1}H	149
4.7	water or polyacrylamide gel	spin echo	2D	64×64; $(0.63\ mm)^2$, a slice 4 mm thick (water) or $(1\ mm)^2$, a slice 10 mm thick (gel)	–	^{1}H	152
4.7	water, pork loin *in vitro*	the same	–	WSR	–	^{1}H	153
2.0	water between glass plates	"	–	WSR	–	^{1}H	155
–	various liquids in rocks or alumina	stimulated echo	–	WSR	–	^{1}H	156
14.1	yeast cells	the same	–	WSR	–	^{1}H	159

Table S.1 (continued).

Field /T	Object, process	Technique	Dimen-sion	Spatial resolution characteristics	Recording time	Nucleus	Ref.
2	water + $CuSO_4$ in glass bead pack	stimulated echo	–	WSR, a slice 3.6 cm thick	1040 – 2080 s	^1H	160
2	water in a polystyrene bead pack or brine in calcium carbonate	the same	–	WSR	–	^1H	161
4.7, 7	water in kraft cellulose	"	–	WSR	–	^1H	162
7	water in ampoule or in granular ion-exchange resin pack	spin echo	–	WSR	–	^1H	163
2	1 mM $CuSO_4$ + water in a tube	gradient echo	2D	128 × 64, a slice 5 mm thick	–	^1H	164
4.7	water or H_2O/D_2O in alumina or silica	spin echo	2D	128 × 128, $(40\ \mu m)^2$, a slice 0.3 – 1 mm thick	–	^1H	167
1.89	H_2O/D_2O in zirconia	the same	1D	128 points, 184 μm	17 s	^1H	174
2.35	H_2O/D_2O in laponite gel	–	1D	–	–	^1H	175
–	water in porous polystyrene, natural sponge, pumice stone or glass bead pack	spin echo or gradient echo	3D	–	–	^1H	176
5	DMSO + NaCl + H_2O + D_2O in artificial dermal replacement	gradient echo	2D	128 × 128, $(67\ \mu m)^2$, a slice 2 mm thick	20 or 40 s	^1H	177
8.5	DMSO, propylene glycol, methanol in fish embryo	spin echo	2D	128 × 128, $(40\ \mu m)^2 - (17\ \mu m)^2$, a slice 100 – 600 μm thick	–	^1H	178
6.3	4-hydroxy-TEMPO in water-containing silk fibroin gel	the same	2D	$(0.2\ mm)^2$, a slice 2 mm thick	5 min	^1H	180
4.7	Ni^{2+} ions in water-saturated sand pack	–	2D	–	2 min	^1H	181
4.7	Na^+ ions in water-saturated sand pack	spin echo	1D	256 points, 0.5 mm without slice selection	7 min	^{23}Na	181
0.5	water in porous silica bead pack	stimulated echo	–	WSR	–	^1H	182
4.7	water in alumina or silica	the same	–	WSR	–	^1H	183
9.4	hexadecane in silica bead pack or MgO/n-octanol paste with or without Fe_2O_3 additive	"	–	WSR	–	^1H	186
2	water or aqueous NaCl solution in glass bead pack or sandstone	"	–	WSR	–	^1H	187
1.4	water in wheat grain	stimulated echo + PRI	2D	64 × 64, $(100\ \mu m)^2$	1.6 h	^1H	188
3	white matter of human brain	spin echo	2D	128 × 128, $(2\ mm)^2$, a slice 5 mm thick	–	^1H	189
7.5	xylene (or toluene) + non-ionic detergent + water	stimulated echo	–	WSR	–	^1H	190

Table S.1 (continued).

Field /T	Object, process	Technique	Dimen-sion	Spatial resolution characteristics	Recording time	Nucleus	Ref.
7.05	suspension of human blood erythrocytes	spin or stimulated echo	–	WSR	25 min	^{1}H	193
7.05	water in glass bead pack	stimulated echo	–	WSR	–	^{1}H	194
4.7	water and 20% gelatin solution; cat brain *in vivo*	spin echo	2D	128 × 128, $(0.55\ mm)^2$	–	^{1}H	195
0.5	water + $CuSO_4$, poly-ethylene glycol, cyclo-hexane; apple, seedling of a plant	the same	–	WSR	–	^{1}H	196
1.5	Xe (0.78 atm) + O_2 (0.15 atm) in glass sphere	FID after selective inversion	1D	1024 points, 0.5 mm (2 mm)	–	^{129}Xe	197
2	^{3}He (9 atm) + O_2 (2 atm) in glass sphere	spin echo	1D	1024; 0.1 mm, a slice 16 mm thick	–	^{3}He	198
1.9	^{3}He (7 atm) in cylinder	gradient echo	1D	0.8 mm	–	^{3}He*	199
9.4	Xe (30 atm) and O_2 in aerogel	chemical shift selective spin echo	3D	$(420\ \mu m)^2$, a slice 1 mm thick	–	^{129}Xe	200
7	C_2F_6 (5 atm) in ceramic composite	spin echo	2D	$(100\ \mu m)^2$, a slice 0.5 mm thick	12 h	^{19}F	201
4.7	Xe (1 – 3 atm, 90% ^{129}Xe) + O_2 or Xe* (3 atm) in a glass cell or glass bead pack	gradient echo, spin echo or stimulated echo	–	WSR	–	^{129}Xe*, ^{129}Xe	202
1.4, 9.4	propane, propene, water, acetone or isopropanol in CsNaX zeolites	spin echo	–	WSR	–	^{1}H	203
1.4	ethane in NaX and NaCaA zeolites	stimulated echo	–	WSR	–	^{1}H	204
4.7, 9.4	ethane in zeolite H-ZSM-5	spin echo	–	WSR	–	^{1}H	205
9.4	n-butane or methane in zeolites	stimulated echo	–	WSR	–	^{1}H	206
7.05, 9.4	benzene (+ Xe) in zeolite powder, 2,3-dimethyl-pentane or Xe in zeolite with coke	spin echo	1D, 2D	–	–	^{1}H, ^{129}Xe	207
2.1	ethane and ethene in zeolite NaX	the same	–	WSR	–	^{1}H	208
2.1	cyclopropane and propene in zeolite NaCdX under reaction conditions	"	–	WSR	–	^{1}H	209
9.4	ethene + CF_4 in silicalite or H-ZSM-5	"	–	WSR	15 min	^{1}H, ^{13}C or ^{19}F	210
–	ethane or methane in $AlPO_4^{5-}$ molecular sieves	stimulated echo	–	WSR	–	^{1}H	211
9.4	CH_4 or CF_4 in zeolites	spin echo	–	WSR	–	^{1}H	212
11.75	Xe + He in tris-(*o*-phenylenedioxy)cyclo-phosphazene crystallites	broad-line NMR	–	WSR	–	^{129}Xe*	213

Table S.1 (continued).

Field /T	Object, process	Technique	Dimen-sion	Spatial resolution characteristics	Recording time	Nucleus	Ref.
2.1	water + $CuSO_4$ and octanol in glass capillaries	B_1-tomography with recording of pseudo-echo and PRI	2D	60 projections, $(11\ \mu m)^2$	–	^1H	214
8.5	water in capillaries	spin echo + gradient echo	1D, 2D	128, 9.4 μm, a slice 0.6 mm thick or without slice selection (1D); 128 × 128, $(9.4\ \mu m)^2$ (2D)	2 s (1D)	^1H	215
3	water in a narrow slit (plastic)	spin echo	1D	512, 25 μm	–	^1H	216
4.3	Xe flow at 0.8 – 1.3 atm in a tube 4 mm in diameter	dynamic NMR micro-scopy (PGSE, PGSTE)	2D in mixed $k-q$-space	512 × 256(q) (256 × 32) or 1024 × 32(q) (512 × 16), 100 μm, without slice selection	–	^{129}Xe*	217
4.3	Xe (2 atm, 80% ^{129}Xe) in an ampoule with rectangular cross-section	FID gradient echo	1D, 2D 1D	– –	– –	^{129}Xe* ^{129}Xe*	218
0.0031	Rb (10 – 100 mg) + N_2 (10 – 200 Torr) + ^3He (0.2 – 2.5 atm) an ampoule with rectangular cross-section	FID	1D	–	–	^3He*	219
–	water in a bent tube with square cross-section	–	–	–	–	–	221
1.5	water in a tube with a cylindrical flow obstruction	gradient echo (EPI)	2D	1.9 × 1.8 mm, a slice 2 mm thick	64 ms	^1H	224
4.7	water in gap between two coaxial cylinders	gradient echo (FLASH)	2D	512 × 512, 195 × 117 μm or $(107\ \mu m)^2$, a slice 2 mm thick	0.5 s	^1H	226
1.4	water + $CuSO_4$ in a capillary, water in a plant stem *in vivo*	stimulated echo + PRI	2D	128 × 128; $(12\ \mu m)^2$, a slice 1 mm thick (capillary), $(75\ \mu m)^2$, a slice 3 mm thick (plant)	–	^1H	227
–	water + 1 mM $CuSO_4$ in a tube	gradient echo (FEER)	–	–	–	^1H	228
–	1.5% solution of carboxy-methylcellulose in extruder	spin echo	2D	128 × 128, $(0.39\ mm)^2$, a slice 10 mm thick	–	^1H	230
2.1	water + $CuCl_2$ in mem-brane bioreactor	the same	2D	–	–	^1H	231
1.4	water + 0.1% $CuSO_4$ in a tube with abrupt contr-action (expansion)	spin echo + PRI	2D	64 × 64, a slice 0.33 mm thick	–	^1H	232
4.7	water + $CuSO_4$ in a tube with contraction	spin echo + gradient echo (EPI)	2D	64 × 64, 1.25 × 0.625 mm or 1.5 × 0.5 mm, a slice 2 mm thick	105 – 115 ms	^1H	233
1.5	water + glycerol in a tube with branching	gradient echo	2D	256 × 256, $(0.5\ mm)^2$, a slice 4 mm thick	–	^1H	234
11.9, 14.1	1 mM KCl + water in a tube filled with glass spheres or without glass spheres	spin echo	2D	128 × 128, $(78\ \mu m)^2$, a slice 100 μm thick	–	^1H	235
1.5	water in U-shaped tube	gradient echo	2D, 3D	128 × 256 (2D); 192 × 256 × 16, 1 × 0.8 × 1.2 mm (3D)	2 or 10 min (2D)	^1H	236

Table S.1 (continued).

Field /T	Object, process	Technique	Dimen-sion	Spatial resolution characteristics	Recording time	Nucleus	Ref.
0.6, 2	polyalkylene glycol (PG) or PMMA microspheres in PG	–	2D	128 × 128 or 256 × 256, a sample 1 cm thick	–	^{1}H	237
7, 1.4	water, water + 0.1% $CuSO_4$, or water + 0.5% high-molecular mass PEO	stimulated + spin echo (VEXSY)	–	WSR	140 min or 4.5 h	^{1}H	238
0.5	water + $CuSO_4$ in U-shaped tube	–	2D	256 × 256, (0.78 mm)^2, a slice 2 or 3 mm thick	36 min	^{1}H	239
1.9	fluid in tube	gradient echo	2D	256 × 256, (0.5 mm)^2, a slice 4.2 mm thick	–	^{1}H	240
2.35	water in a tube with contraction/expansion	FID + PRI or spin echo	2D	256 × 256, (118 μm)^2, a slice 2 mm thick (echo); 128 × 32 or 256 × 64, 0.7, 0.8 or 1.6 mm, a slice 0.5 cm thick (FID)	8 or 23 ms (FID)	^{1}H	244
0.5	blood in thoracic aorta	spin echo or gradient echo	2D	256 × 256, (1.6 mm)^2, a slice 10 mm thick	15 – 20 min	^{1}H	245
1.5	water + $MnCl_2$ or water + human albumin in tube	spiral trajectories	2D	(1.46 mm)^2 – (2.4 mm)^2, a slice 5 – 7 mm thick	180 ms (60 ms)	^{1}H	246
7.05	water + $CuSO_4$ in a tube or cylinder	spin echo	2D	256 × 128, (0.27 mm)^2, a slice 2 mm thick or 1024 × 64, 0.078 mm × 0.23 mm, a slice 0.4 mm thick	17 or 2 min	^{1}H	249
2	water in a tube with partitions	the same	2D, 3D	128 × 64 × 64 (3D)	137 min	^{1}H	250
1.0	water + $CuSO_4$ in a tube	gradient (EPI) or spin echo	2D	64 × 64, (375 μm)^2 (EPI) or 256 × 256, (94 μm)^2 (spin echo); a slice 2.5 mm thick	21.12 ms (EPI)	^{1}H	251
4.7	fertilised bird eggs	gradient echo	1D, 2D	(200 μm)^2 or (300 μm)^2, a slice 2.7 mm thick	–	^{1}H	252
1.9	mustard seeds in horizontal rotating cylinder	spin echo	2D	128 × 128; (0.8 mm)^2, a slice 8 mm thick	15 min	^{1}H	253
1.9	the same	the same	2D	a slice 8 mm thick	–	^{1}H	254
1.9	water in straight tube or a tube with branching	gradient echo or spin echo	1D, 2D	–	–	^{1}H	256
4.7	water in a tube	spin echo	2D	256 × 256, (78 μm)^2 or (65 μm)^2, a slice 1 mm or 3 mm thick	6.5, 13 or 80 min	^{1}H	261
7.05, 14.1	DMSO or water in an ampoule 5 mm in diameter	stimulated echo	2D	32 × 256; a slice 1.4 mm thick	10 min	^{1}H	262
2.35	water in a tube with U-shaped bend	FID, radial trajectories (RUFIS); spin echo	2D	0.6 – 1.2 mm (RUFIS)	8 – 11 ms (RUFIS)	^{1}H	263
2	water + $CuSO_4$, turbulent flow in a tube	spin echo (EPI)	2D	64 × 64, (1.2 mm)^2, a slice 3 mm thick	33 ms	^{1}H	264
1.9	oil-filled plastic beads in horizontal rotating cylinder	spin echo	2D	(1 mm)^2, a slice 20 mm thick	–	^{1}H	265

Table S.1 (continued).

Field /T	Object, process	Technique	Dimen-sion	Spatial resolution characteristics	Recording time	Nucleus	Ref.
1.9	water + glycerol in a tube with diaphragm (stenosis)	spin echo	2D	128 × 256, (0.39 mm)^2	–	^{1}H	266
1.5	intracardiac blood flow	gradient echo	3D, 2D	256 × 256 × 16, 1.2 × 1.2 × 8 mm (3D); 256 × 128, 1.25 × 2.5 mm, a slice 7 mm thick	29 min (3D), 2 min/a slice (2D)	^{1}H	267
0.47	water + $CuSO_4$ in a tube, water in tomato stem	spin echo (turbo)	2D	128 × 128, (315 μm)^2 or (117 μm)^2, a slice 3 mm thick	31 or 64 s	^{1}H	270
7	water + glycerol + $CuSO_4$ or pig blood in tube	spin echo	1D	78 μm or 23 μm, a slice 1 mm thick or WSR	20 min (1D)	^{1}H	272
7.05	0.1% aqueous solution of PEO in tube, water and nutrients in castor-oil plant stem	the same	2D	128 × 128, (54.7 μm)^2; 64 × 64, (469 μm)^2 or (1.4 mm)^2 (tube); 128 × 128, (47 μm)^2 (stem)	–	^{1}H	273
–	water + $CuSO_4$ in a coiled tube	gradient echo	2D	64 × 64	1 min	^{1}H	274
1	water in a tube	spin echo + gradient echo	2D	32 × 32, (0.75 mm)^2, a slice 4 mm thick	20.5 ms	^{1}H	276
2	water + $CuSO_4$ in a tube with grid-generated turbulence or without it	gradient echo	1D	256 or 128, 0.29 or 0.58 mm, a slice 3 mm thick	–	^{1}H	277
1.5	water + $MnCl_2$ in a tube with contraction – expansion	the same	2D	256 × 256, (590 μm)^2, a slice 5 mm thick	–	^{1}H	278
1.9	oil-filled plastic beads in horizontal rotating cylinder	spin echo	2D	(1 mm)^2, a slice 20 mm thick	–	^{1}H	279
7	water in a tube or in a dialysis cell	spin echo or stimulated echo	–	WSR	–	^{1}H	280
7.05	water + $CuSO_4$ in a tube or conical converging tube	spin echo	–	WSR	–	^{1}H	281
7	$C_6D_5NO_2$	the same	1D	90 μm	–	^{2}H	282
2	water + $CuSO_4$ in glass bead pack	spin echo + stimulated echo	–	a slice 10 mm thick	–	^{1}H	283
11.75	water in a tube	spin echo	2D	128 × 128, (39 μm)^2, a slice 500 μm	–	^{1}H	285
7	water in a tube, gel during compression	spin echo (PEPI)	2D	32 × 32, 125 × 250 μm	80 ms	^{1}H	286
7	0.1% $CuSO_4$ + water in a tube or hemodialysis cell	spin echo	2D	128 × 64, 94 × 190 μm a slice 1.6 mm thick	–	^{1}H	287
2	flow of water, sunflower oil or oil-in-water emulsion in a tube	gradient echo	2D, 3D	64 × 64, (850 μm)^2 or (780 μm)^2, a slice 2 or 2.5 mm thick; 64 × 64 × 64, (710 μm)^3 (3D)	20 – 60 s (2D); 23 min (3D)	;^{1}H	288
0.47	water + $MnCl_2$ on walls of a monolithic catalyst	–	–	128 × 128, (0.4 mm)^2 or 192 × 192, (78 μm)^2, a slice 4 mm thick	13 – 17 min	^{1}H	289
4.7	polydimethylsiloxane film on vertical surface	spin echo	2D	–	–	^{1}H	290
0.7	water + $MnCl_2$ in a tube, corn stem, tomato pedicel	stimulated echo + (turbo) spin echo	2D	128 × 128, (0.16 mm)^2 or (0.12 mm)^2, a slice 3 or 4 mm thick	17 – 19 min	^{1}H	291

Table S.1 (continued).

Field /T	Object, process	Technique	Dimen-sion	Spatial resolution characteristics	Recording time	Nucleus	Ref.
1.5	water + $MnCl_2$ in a tube, blood in human femoral artery	gradient echo or spiral trajectories	2D	256 × 256, $(0.63\ mm)^2$ or 205 × 205, $(0.88\ mm)^2$, a slice 10 mm thick	–	^1H	292
1.5	water in a tube placed in agar gel	gradient echo	2D	256 × 256, $(2.44\ mm)^2$, a slice 5 mm thick	–	^1H	293
7, 11.7	convection in DMSO, water or chloroform	stimulated echo	–	WSR	–	^1H	294
7, 11.7	DMSO, water or chloroform	FID	1D	170 μm	–	^1H	294
2	convection in silicon oil	spin echo	2D	256 × 256, a slice 1 cm thick	4 min	^1H	295
7.05	5% polystyrene in cyclohexane	the same	2D, WSR	–	–	^1H	296
4.7	falling droplet of water or water + surfactant	–	2D, 3D	–	10 h (3D)	^1H	297
7	1 mM KCl + water in a tube	stimulated echo	2D	128 × 128, $(78\ \mu m)^2$, a slice 4 mm thick	–	^1H	298
2	water + $CuSO_4$ in U-shaped tube	spin echo	2D	256, a slice 5 mm thick	–	^1H	299
1	gelatin in a rotating tube, water in a tube	gradient echo + spin echo	2D	32 × 32, $(0.75\ mm)^2$	20.48 ms	^1H	300
2.35	water in a tube with contraction	FID + PRI or spin echo	2D	24 mm FOV (32 projections per 180° sector), a slice 5 mm thick (FID); a slice 2 mm thick (echo)	11 ms (FID)	^1H	301
1.5	water + $GdCl_3$ (EDTA) in a tube or in a tube with expansion	gradient echo	2D	256 × 256, $(1.25\ mm)^2$ or $(0.94\ mm)^2$, a slice 1 cm thick	263 s	^1H	302
2	5 mM $CuSO_4$ + water in gap between two coaxial cylinders	gradient echo, spin echo	2D 1D	512 × 512, $(50\ \mu m)^2$, a slice 5 mm thick (2D); 512, 50 μm, a slice of surface area 1 mm × 1 cm	2 min (2D); 3.2 s (1D)	^1H	303
4.7	50% H_3PO_4/D_2O in gap between two coaxial cylinders	spin echo	1D	–	–	^{31}P	304
4.7	oil-in-water emulsion (5% or 20%) + detergent and $CuSO_4$ in a tube or hollow-fibre membrane filter	spin or stimulated echo	2D	128 × 128, $(94\ \mu m)^2$ or 256 × 256, $(47\ \mu m)^2$, a slice 1 mm thick	–	^1H	305
0.6	1% solution of carboxy-methylcellulose in a tube	spin echo	1D	147 μm	192 s	^1H	306
0.6	low-density polyethylene melt in a tube	the same	1D	256; 0.25 mm	–	^1H	307
7.05	water or polydimethyl-siloxane in NMR rheometers of different design	"	2D	128 × 128, $(20\ \mu m)^2$, 35 × 78 μm or 96 × 32 μm, a slice 2 mm thick or without slice selection	30 min	^1H	308
7.05	aqueous solution of cetyl-pyridinium chloride + sodium salicylate, tomato sauce, CTAB/D_2O micellar solution, polyacryl-amide/D_2O	"	2D	–	–	^1H, ^2H	309

Table S.1 (continued).

Field /T	Object, process	Technique	Dimen-sion	Spatial resolution characteristics	Recording time	Nucleus	Ref.
1.9	PMMA beads + a mixture of fluids in a tube with contraction and expansion	spin echo	2D	128 × 128 or 256 × 128, (200 μm)^2, a slice 0.5 cm thick	2 or 4 min	^{1}H	311
2	urethane rubber based composite or dog kidney in gelatin	stimulated echo	2D	128 × 128 or 256 × 256; (0.8 mm)^2 or (0.6 mm)^2, a slice 5 or 10 mm thick	–	^{1}H	312
1.5	agar gel	gradient echo (FLASH)	2D	256 × 256; (0.55 mm)^2	12 s	^{1}H	313
1.5	agar gel or pig kidney in gel	gradient echo or spin echo	2D	128 × 128 or 256 × 256, a slice 10 mm thick	10 – 120 s	^{1}H	314
1.5	agar gel	gradient echo (FLASH)	2D	128 × 128 or 256 × 256	20 – 120 s	^{1}H	315
1.5	tissues *ex vivo*, agar gel, female breast	gradient echo or spin echo	2D	256 × 128; 0.63 × 1.25 mm, a slice 10 mm thick	–	^{1}H	317
7	water in latex microsphere pack	spin echo	2D	128 × 128, (31.5 μm)^2, a slice 200 μm thick or 64 × 64, (63.5 μm)^2, a slice 1 mm thick	–	^{1}H	318
2	D_2O + hexadecane in limestone	–	1D	–	–	^{1}H	319
4.7	water or water + air in granular alumina pack	spin echo	3D	256 × 256 × 32, (156 μm)^3	–	^{1}H	320
4.7	water in glass bead pack	the same	2D, 3D	256 × 256, (195 μm)^2, a slice 1 mm thick; 256 × 256 × 256, (195 μm)^3 (3D)	–	^{1}H	321
2	water or n-hexadecane + D_2O in sandstone or limestone	"	1D	0.6 mm	–	^{1}H	322
2	water or D_2O + n-octadecane or n-hexadecane in sandstone or limestone	"	1D	0.42 or 0.19 mm, a slice 4 mm thick	2 min or 16 s	^{1}H	323
2	D_2O and n-dodecane in limestone	"	1D, 2D	128 points, 783 μm (1D)	–	^{1}H	324
1.9	mixture of aliphatic hydrocarbons in sandstone	stimulated echo	2D	(1.2 mm)^2, a slice 14 mm thick	–	^{1}H	325
0.5	water in a tube, water or 3% brine in sandstone	spin echo	2D	(1 mm)^2 or (3 mm)^2, a slice 1 cm thick	–	^{1}H	326
0.5	water in a tube or water in glass bead pack	stimulated echo	–	WSR	–	^{1}H	327
1.9	water + contrast agent in plastic bead pack	spin echo	2D	128 × 128 or 128 × 256, (0.4 mm)^2, a slice 5 or 20 mm thick	4 min	^{1}H	328
–	water in sandstone	spin echo (PEPI)	2D	a slice 18 mm thick	–	^{1}H	329
2	1% KCl + water in sandstone	spin echo	3D	64 × 64 × 16, 1 × 1 × 8 mm	–	^{1}H	330
0.5	water in bead pack	spin echo or stimulated echo	–	WSR	–	^{1}H	331

Table S.1 (continued).

Field /T	Object, process	Technique	Dimen-sion	Spatial resolution characteristics	Recording time	Nucleus	Ref.
2	3% aqueous NaCl solution in sandstone	stimulated echo	–	WSR	–	^{1}H	333
2	water or 3% NaCl + dodecane solution in sandstone	the same	–	WSR	–	^{1}H	334
–	water in polystyrene bead pack	spin echo	–	WSR	–	^{1}H	336
1.89	water + Gd-based contrast agent in glass bead pack	spin echo, modified stimulated echo	1D 2D	128 (1D), 1.39 mm; 128 × 128, 0.91 mm × 1.16 mm, a slice 5 mm thick	300 ms (1D)	^{1}H	337
1.5	water + $CuSO_4$ or water + $CuSO_4$ + NaCl in fused quartz bead pack	spin echo	2D	128 × 128, $(2.36\ mm)^2$, a slice 5 or 10 mm thick	0.5 – 3 min	^{1}H	338
5	$GdCl_3$ in glass bead pack filled with water	spin echo, stimulated echo	2D	128 × 16, 1 × 3 mm, a slice 4 mm thick	–	^{1}H	339
1.5, 4.7	aqueous Gd(DTPA) solution in chromato-graphic column (^{1}H); free Na^+ ions in ion-exchange column	gradient echo (FLASH)	2D (^{1}H), 3D (^{23}Na)	256 × 256 or 128 × 128, (300 – 1000) × (300 – 1000) μm, a slice 2 – 5 mm thick (^{1}H)	0.4 – 6 s (^{1}H), 4 min (^{23}Na)	^{1}H, ^{23}Na	340
0.5	water in porous silica bead pack	stimulated echo	–	WSR	–	^{1}H	342
–	water in glass bead pack	spin echo (PEPI)	2D	16 × 32, a slice 10 – 50 mm thick	–	^{1}H	343
0.1	Mn_2(EDTA) complex in glass bead pack filled with water	spin echo	3D, 1D	256 × 128 × 32, 1 × 2 × 3 mm (3D); 256 points, 1 mm (1D)	13 min (3D), 9 s (1D)	^{1}H	344
0.5	water in porous silica bead pack	–		WSR	–	^{1}H	345
2	3% brine or water + $CuSO_4$ in glass bead pack, glass or polyamide fibres or in sandstone	stimulated echo	–	WSR	–	^{1}H	347
348	drilling fluid (suspension of bentonite in water with additives) in limestone or sandstone	spin echo	1D	128; 0.48 – 2.4 mm	–	^{1}H	2
2	aqueous clay suspension (bentonite) in limestone	gradient echo (FLASH) or spin echo	2D	128 × 64 or 128 × 128, a slice 5 or 10 mm thick	1.9 s (FLASH)	^{1}H	349
2	bentonite + water + NaOH + lignosulfonate dispersant (+ barite) in sandstone or limestone	spin echo	1D	128	–	^{1}H	350
2	clay suspension in water	spin echo with inversion – recovery	1D	0.54 mm	–	^{1}H	351
1.5	oil + aqueous $CaCl_2$ solution + isopropan-ol-d_8 in sandstone, oil + aqueous NaI solution in dolomite	chemical shift selective spin echo	2D	128 × 256, $(0.5\ mm)^2$, a slice 5 mm thick	20 min	^{1}H	352

Table S.1 (continued).

Field /T	Object, process	Technique	Dimen-sion	Spatial resolution characteristics	Recording time	Nucleus	Ref.
1.89	oil + water in dolomite	chemical shift selective spin echo	1D, 2D	128 points, 0.8 mm (1D), 128 × 128, 0.3 × 0.8 mm (2D)	5 min (1D), 2.5 h (2D)	^{1}H	353
2	n-octadecane + D_2O in limestone	spin echo	1D	–	7.5 s	^{1}H	354
1.9	water + $NiSO_4$ or mixture of hydrocarbons in crushed glass pack	the same	2D	256 × 256, $(0.45\ mm)^2$, a slice 1.7 mm thick	26.5 min	^{1}H	355
–	hexadecane and D_2O in sandstone	–	1D	–	–	^{1}H	356
4.7	n-hexanol and water in sand	spin echo	1D	400 μm	–	^{1}H	358
4.7	octanol and water in glass bead pack	the same	2D, 3D	256 × 256 × 256, 195 × 195 × 195 μm or 128 × 128 × 128, $(390\ \mu m)^3$ (3D), 256 × 256, $(195\ \mu m)^2$, a slice 1 mm thick	–	^{1}H	359
1.9	water + Cu(II) in ion-exchange column	gradient echo	3D	16 × 16 × 512, a slice 0.13 mm thick	20 min	^{1}H	362
1.9	pharmaceutical granules in horizontal rotating cylinder	spin echo	2D	$(0.8\ mm)^2$, a slice 8 mm thick	–	^{1}H	363
2	mustard seeds + glass or sugar beads in rotating cylinder or narrow cylinder	–	3D	128 × 128 × 128	–	^{1}H	364
1.9	oil-filled plastic beads rotated in a container	gradient echo	1D (2D)	a slice 4 × 2.5 mm	–	^{1}H	365
2	poppy grains in shaken vertical cylinder	–	2D	a slice 1 or 2 mm thick	–	^{1}H	366
4.2	Xe (0.4 atm) + N_2 (0.27 atm) + He (total pressure of the gas mixture 4 atm) in capillaries, in a tube, flow through a tube with diaphragm or polyurethane foam	gradient echo (PGSE)	2D	256 × 128, 110 × 340 μm, a slice 5 mm thick	51 min	^{129}Xe*	368
			2D in mixed $k-q$-space	256 × 32, a slice 4 mm thick	–	^{129}Xe*	368
4.3	Xe (1–3 atm, 80% ^{129}Xe) in coaxial tubes or in capillary bundle	gradient echo (FLASH)	2D	128 × 64, 0.1 mm	–	^{129}Xe*	370
4.3	Xe (1–3 atm, 80% ^{129}Xe) in aerogel	the same	1D	0.1 mm	–	^{129}Xe*	370
9.4	Xe ($10^{19}\ cm^{-3}$, 70% ^{129}Xe) in mice lungs *in vitro* in an ampoule	"	2D	128 × 128, $(0.37\ mm)^2$	600 ms	^{129}Xe*	371
2.35	C_3F_7H (2 atm) in phantom or sandstone	gradient echo	1D	0.5 mm	21 min	–	373

Notes: PVA is poly(vinyl alcohol), PVC is poly(vinyl chloride), PEMA is poly(ethyl methacrylate), PMMA is poly(methyl methacrylate), PEO is poly(ethylene oxide), DMSO is dimethyl sulfoxide; PRI is projection reconstructed imaging, WSR is without spatial resolution, FID is free induction decay; EPI is echo-planar imaging, PEPI is echo-planar imaging with PI-pulses, STRAFI is stray field imaging and FLASH is fast low-angle shot.

References

1. I V Koptyug, R Z Sagdeev *Usp. Khim.* **71** 672 (2002) [*Russ. Chem. Rev.* **71** 593 (2002)]
2. L Pel, K Kopinga, H Brocken *Magn. Reson. Imaging* **14** 931 (1996)
3. K Kopinga, L Pel *Rev. Sci. Instrum.* **65** 3673 (1994)
4. L Pel, K Kopinga, G Bertram, G Lang *J. Phys. D* **28** 675 (1995)
5. J Kaufmann, W Studer, J Link, K Schenker *Mag. Concr. Res.* **49** 157 (1997)
6. S Black, D M Lane, P J McDonald, D J Hannant, M Mulheron, G Hunter, M R Jones *J. Mater. Sci. Lett.* **14** 1175 (1995)
7. I V Koptyug, R Z Sagdeev, L Yu Khitrina, V N Parmon *Appl. Magn. Reson.* **18** 13 (2000)
8. I V Koptyug, L Yu Il'ina, A V Matveev, V N Parmon, R Z Sagdeev *Khim. Fiz.* **21** 68 (2002) [a]
9. R J Gummerson, C Hall, W D Hoff, R Hawkes, G N Holland, W S Moore *Nature (London)* **281** 56 (1979)
10. T A Carpenter, E S Davies, C Hall, L D Hall, W D Hoff, M A Wilson *Mater. Struct.* **26** 286 (1993)
11. L Pel, K Hazrati, K Kopinga, J Marchand *Magn. Reson. Imaging* **16** 525 (1998)
12. L Pel, K Kopinga, E F Kaasschieter *J. Phys. D* **33** 1380 (2000)
13. G Papavassiliou, F Milia, M Fardis, R Rumm, E Laganas, O Jarh, A Sepe, R Blinc, M M Pintar *J. Am. Ceram. Soc.* **76** 2109 (1993)
14. P J McDonald, T Pritchard, S P Roberts *J. Colloid Interface Sci.* **177** 439 (1996)
15. Yu I Aristov, G Restuccia, M M Tokarev, G Cacciola *React. Kinet. Catal. Lett.* **69** 345 (2000)
16. M M Tokarev, S G Kozlova, S P Gabuda, Yu I Aristov *Zh. Strukt. Khim.* **39** 259 (1998) [b]
17. Yu I Aristov, M M Tokarev, G DiMarko, G Kachchiola, D Restuchcha, V N Parmon *Zh. Fiz. Khim.* **71** 253 (1997) [c]
18. I V Koptyug, L Yu Khitrina, Yu I Aristov, M M Tokarev, K T Iskakov, V N Parmon, R Z Sagdeev *J. Phys. Chem. B* **104** 1695 (2000)
19. S I Kabanikhin, I V Koptyug, K T Iskakov, R Z Sagdeev *Int. J. Nonlinear Sci. Numer. Simul.* **1** 29 (2000)
20. I V Koptyug, L Yu Khitrina, V N Parmon, R Z Sagdeev *Magn. Reson. Imaging* **19** 531 (2001)
21. M R Halse *Magn. Reson. Imaging* **14** 745 (1996)
22. P J Prado, B J Balcom, M Jama *J. Magn. Reson.* **137** 59 (1999)
23. P D M Hughes, P J McDonald, E G Smith *J. Magn. Reson. A* **121** 147 (1996)
24. J Karger, G Seiffert, F Stallmach *J. Magn. Reson. A* **102** 327 (1993)
25. W Heink, J Karger, H Pfeifer *Chem. Eng. Sci.* **33** 1019 (1978)
26. J Karger, H Pfeifer *Magn. Reson. Imaging* **12** 235 (1994)
27. S M Belliveau, T L Henselwood, C H Langford *Environ. Sci. Technol.* **34** 2439 (2000)
28. R S Drago, D C Ferris, D S Burns *J. Am. Chem. Soc.* **117** 6914 (1995)
29. P Y Ghi, D J T Hill, A K Whittaker *Biomacromolecules* **2** 504 (2001)
30. S R Smith, J L Koenig *Macromolecules* **24** 3496 (1991)
31. M A Rana, J L Koenig *Macromolecules* **27** 3727 (1994)
32. A G Webb, L D Hall *Polym. Commun.* **31** 422 (1990)
33. S Blackband, P Mansfield *J. Phys. C* **19** L49 (1986)
34. P Mansfield, R Bowtell, S Blackband *J. Magn. Reson.* **99** 507 (1992)
35. M Ercken, P Adriaensens, D Vanderzande, J Gelan *Macromolecules* **28** 8541 (1995)
36. G D Cody, R E Botto *Macromolecules* **27** 2607 (1994)
37. G D Cody, R E Botto *Energy Fuels* **7** 561 (1993)
38. L A Weisenberger, J L Koenig *J. Polym. Sci. C* **27** 55 (1989)
39. L A Weisenberger, J L Koenig *Macromolecules* **23** 2445 (1990)
40. R A Grinsted, L Clark, J L Koenig *Macromolecules* **25** 1235 (1992)
41. M Valtier, P Tekely, L Kiene, D Canet *Macromolecules* **28** 4075 (1995)
42. P Maffei, L Kiene, D Canet *Macromolecules* **25** 7114 (1992)
43. L A Weisenberger, J L Koenig *Appl. Spectrosc.* **43** 1117 (1989)
44. M Ercken, P Adriaensens, G Reggers, R Carleer, D Vanderzande, J Gelan *Macromolecules* **29** 5671 (1996)
45. M Ilg, B Pfleiderer, K Albert, W Rapp, E Bayer *Macromolecules* **27** 2778 (1994)
46. M Knorgen, K-F Arndt, S Richter, D Kuckling, H Schneider *J. Mol. Struct.* **554** 69 (2000)
47. R A Grinsted, J L Koenig *Macromolecules* **25** 1229 (1992)
48. A G Webb, L D Hall *Polym. Commun.* **31** 425 (1990)
49. M Ilg, K Albert, W Rapp, E Bayer *J. Magn. Reson.* **90** 370 (1990)
50. M R Halse, H J Rahman, J H Strange *Physica B* **203** 169 (1994)
51. T M Hyde, L F Gladden *Polymer* **39** 811 (1998)
52. T G Nunes, G Guillot, J M Bordado *Polymer* **41** 4643 (2000)
53. A Lauenstein, J Tegenfeldt, W Kuhn *Macromolecules* **31** 3886 (1998)
54. K L Perry, P J McDonald, E W Randall, K Zick *Polymer* **35** 2744 (1994)
55. R E Gerald, R J Klinger, J W Rathke, G Sandi, K Woelk, in *Spatially Resolved Magnetic Resonance. Methods, Materials, Medicine, Biology, Rheology, Geology, Ecology, Hardware* (Eds B Blümich, P Blümler, R Botto, E Fukushima) (Weinheim: VCH-Wiley, 1998) p. 109
56. F Tabak, M Corti *J. Chem. Phys.* **92** 2673 (1990)
57. I Hopkinson, R A L Jones, S Black, D M Lane, P J McDonald *Carbohyd. Polym.* **34** 39 (1997)
58. Z Ma, P Zhang, G Ding, L Li, C Ye *Fuel Sci. Technol. Int.* **14** 1391 (1996)
59. W P Rothwell, D R Holecek, J A Kershaw *J. Polym. Sci. Polym. Lett. Ed.* **22** 241 (1984)
60. R S Clough, J L Koenig *J. Polym. Sci. C, Polym. Lett.* **27** 451 (1989)
61. A G Webb, P Jezzard, L D Hall, S Ng *Polym. Commun.* **30** 363 (1989)
62. A G Webb, K Motsegood, R B Clarkson *Fuel* **72** 1235 (1993)
63. D C French, S L Dieckman, R E Botto *Energy Fuels* **7** 90 (1993)
64. L A Weisenberger, J L Koenig *Macromolecules* **23** 2454 (1990)
65. B Narasimhan, J E M Snaar, R W Bowtell, S Morgan, C D Melia, N A Peppas *Macromolecules* **32** 704 (1999)
66. C A Fyfe, A I Blazek *Macromolecules* **30** 6230 (1997)
67. B J Balcom, in *Spatially Resolved Magnetic Resonance. Methods, Materials, Medicine, Biology, Rheology, Geology, Ecology, Hardware* (Eds B Blümich, P Blümler, R Botto, E Fukushima) (Weinheim: VCH-Wiley, 1998) p. 75
68. P D Riggs, P Kinchesh, M Braden, M P Patel *Biomaterials* **22** 419 (2001)
69. A Spyros, R Kimmich, B H Briese, D Jendrossek *Macromolecules* **30** 8218 (1997)
70. M Bogdan, B J Balcom, T W Bremner, R L Armstrong *J. Magn. Reson. A* **116** 266 (1995)
71. J M Listerud, S W Sinton, G P Drobny *Anal. Chem.* **61** 23A (1989)
72. B Blumich *Concepts Magn. Reson.* **10** 19 (1998)
73. B Blumich, P Blümler, L Gasper, A Guthausen, V Gobbels, S Laukemper-Ostendorf, K Unseld, G Zimmer *Macromol. Symp.* **141** 83 (1999)
74. P Blümler, B Blümich *NMR Basic Principles Prog.* **30** 209 (1994)
75. P Blümler, B Blümich *Rubber Chem. Technol.* **70** 468 (1997)
76. P Jezzard, J J Attard, T A Carpenter, L D Hall *Prog. NMR Spectrosc.* **23** 1 (1991)
77. J B Miller *Prog. NMR Spectrosc.* **33** 273 (1998)
78. T Nunes, E W Randall, A A Samoilenko, P Bodart, G Feio *J. Phys.* **29** 805 (1996)
79. S D Beyea, B J Balcom, T W Bremner, P J Prado, D P Green, R L Armstrong, P E Grattan-Bellew *Cement Concrete Res.* **28** 453 (1998)
80. P M Glover, P S Aptaker, J R Bowler, E Ciampi, P J McDonald *J. Magn. Reson.* **139** 90 (1999)
81. J-P Gorce, J L Keddie, P J McDonald *MR Profiling of Drying in Alkyd Emulsions: Origins of Skin Formation* (St Petersburg, Russia: NATO Advanced Studies Institute, 2001)
82. P D M Hughes, P J McDonald, N P Rhodes, J W Rockliffe, E G Smith, J Wills *J. Colloid Interface Sci.* **177** 208 (1996)
83. S D Beyea, B J Balcom, T W Bremner, P J Prado, A R Cross, R L Armstrong, P E Grattan-Bellew *Solid State NMR* **13** 93 (1998)
84. C Choi, B J Balcom, S D Beyea, T W Bremner, P E Grattan-Bellew, R L Armstrong *J. Appl. Phys.* **88** 3578 (2000)
85. S D Beyea, B J Balcom, P J Prado, A R Cross, C B Kennedy, R L Armstrong, T W Bremner *J. Magn. Reson.* **135** 156 (1998)

86. J Tritt-Goc, N Pislewski, S Koscielski, F Milia *Cement Concrete Res.* **30** 931 (2000)
87. L Pel, H Brocken, K Kopinga *Int. J. Heat Mass Transf.* **39** 1273 (1996)
88. G Guillot, A Trokiner, L Darrasse, H Saint-Jalmes *J. Phys. D* **22** 1646 (1989)
89. M P Hollewand, L F Gladden *Magn. Reson. Imaging* **12** 291 (1994)
90. I V Koptyug, V B Fenelonov, L Yu Khitrina, R Z Sagdeev, V N Parmon *J. Phys. Chem. B* **102** 3090 (1998)
91. I V Koptyug, S I Kabanikhin, K T Iskakov, V B Fenelonov, L Yu Khitrina, R Z Sagdeev, V N Parmon *Chem. Eng. Sci.* **55** 1559 (2000)
92. S I Kabanikhin, I V Koptyug, K T Iskakov, R Z Sagdeev *J. Inv. Ill-Posed Problems* **6** 335 (1998)
93. I V Koptyug, L Yu Ilyina, A V Matveev, R Z Sagdeev, V N Parmon, S A Altobelli *Catal. Today* **69** 385 (2001)
94. B Manz, P S Chow, L F Gladden *J. Magn. Reson.* **136** 226 (1999)
95. B P Hills, K M Wright, J J Wright, T A Carpenter, L D Hall *Magn. Reson. Imaging* **12** 1053 (1994)
96. I V Koptyug, L Yu Il'ina, V B Fenelonov, A Yu Derevyankin, R Z Sagdeev, V N Parmon *Dokl. Akad. Nauk* **376** 1 (2001) [d]
97. J M Salamanca, E Ciampi, D A Faux, P M Glover, P J McDonald, A F Routh, A C I A Peters, R Satguru, J L Keddie *Langmuir* **17** 3202 (2001)
98. E Ciampi, U Goerke, J L Keddie, P J McDonald *Langmuir* **16** 1057 (2000)
99. M Wallin, P M Glover, A-C Hellgren, J L Keddie, P J McDonald *Macromolecules* **33** 8443 (2000)
100. S G Harding, D Wessman, S Stenstrom, L Kenne *Chem. Eng. Sci.* **56** 5269 (2001)
101. J R Olson, S J Chang, P C Wang *Can. J. Forest Res.* **20** 586 (1990)
102. R S Menon, A L Mackay, J R T Hailey, M Bloom, A E Burgess, J S Swanson *J. Appl. Polym. Sci.* **33** 1141 (1987)
103. V N Glaznev, I V Koptyug, Yu G Korobeinikov *Inzhenerno-Fiz. Zh.* **72** 437 (1999)
104. V N Glaznev, I V Koptyug, Yu G Korobeinikov *J. Eng. Phys. Thermophys.* **72** 409 (1999)
105. H Song, J R Litchfield *Trans. ASAE* **33** 1286 (1990)
106. A J Kovacs, M Nemenyi *Magn. Reson. Imaging* **17** 1077 (1999)
107. J Leisen, L Hou, H W Beckham, W W Carr, in *Spatially Resolved Magnetic Resonance. Methods, Materials, Medicine, Biology, Rheology, Geology, Ecology, Hardware* (Eds B Blümich, P Blümler, R Botto, E Fukushima) (Weinheim: VCH-Wiley, 1998) p. 265
108. E L Hahn *Phys. Rev.* **80** 580 (1950)
109. E O Stejskal, J E Tanner *J. Chem. Phys.* **42** 288 (1965)
110. C S Johnson *Prog. NMR Spectrosc.* **34** 203 (1999)
111. K F Morris, C S Johnson *J. Am. Chem. Soc.* **115** 4291 (1993)
112. D Wu, A Chen, C S Johnson *J. Magn. Reson. A* **115** 260 (1995)
113. H Barjat, G A Morris, S Smart, A Swanson, S C R Williams *J. Magn. Reson. B* **108** 170 (1995)
114. D P Hinton, C P Johnson *J. Phys. Chem.* **97** 9064 (1993)
115. J Körger, D M Ruthven *Diffusion in Zeolites and Other Microporous Solids* (New York: Wiley, 1992)
116. P T Callaghan *Principles of Nuclear Magnetic Resonance Microscopy* (Oxford: Clarendon Press, 1991)
117. M D Hurlimann, K G Helmer, L L Latour, C H Sotak *J. Magn. Reson. A* **111** 169 (1994)
118. H-K Liaw, R Kulkarni, S Shen, A A Watson *AIChE J.* **42** 538 (1996)
119. P P Mitra, P N Sen, L M Schwartz *Phys. Rev. B* **47** 8565 (1993)
120. L L Latour, P P Mitra, R L Kleinberg, C H Sotak *J. Magn. Reson. A* **101** 342 (1993)
121. L L Latour, R L Kleinberg, P P Mitra, C H Sotak *J. Magn. Reson. A* **112** 83 (1995)
122. A Caprihan, C F M Clewett, D O Kuethe, E Fukushima, S J Glass *Magn. Reson. Imaging* **19** 311 (2001)
123. S Peled, C-H Tseng, A A Sodickson, R W Mair, R L Walsworth, D G Cory *J. Magn. Reson.* **140** 320 (1999)
124. P L McDaniel, C G Coe, J Karger, J D Moyer *J. Phys. Chem.* **100** 16263 (1996)
125. J D Seymour, P T Callaghan *J. Magn. Reson. A* **122** 90 (1996)
126. X Gong, A Bandis, A Tao, G Meresi, Y Wang, P T Inglefield, A A Jones, W-Y Wen *Polymer* **42** 6485 (2001)
127. R L Kleinberg *Magn. Reson. Imaging* **12** 271 (1994)
128. A Bax *Two-Dimensional Nuclear Magnetic Resonance in Liquids* (Delft: Delft University Press, 1982)
129. P Mutzenhardt, D Canet *J. Chem. Phys.* **105** 4405 (1996)
130. L van Dam, B Andreasson, L Nordenskiold *Chem. Phys. Lett.* **262** 737 (1996)
131. R R Ernst *Angew. Chem., Int. Ed. Engl.* **31** 805 (1992)
132. I Ardelean, R Kimmich *J. Magn. Reson.* **143** 101 (2000)
133. J Zhong, Z Chen, E Kwok, S Kennedy *Magn. Reson. Imaging* **19** 33 (2001)
134. P T Callaghan, D MacGowan, K J Packer, F O Zelaya *J. Magn. Reson.* **90** 177 (1990)
135. B J Balcom, A E Fischer, T A Carpenter, L D Hall *J. Am. Chem. Soc.* **115** 3300 (1993)
136. B J Balcom, T J Lees, A R Sharp, N S Kulkarni, G S Wagner *Phys. Med. Biol.* **40** 1665 (1995)
137. A E Fischer, B J Balcom, E J Fordham, T A Carpenter, L D Hall *J. Phys. D* **28** 384 (1995)
138. N-K Bar, J Karger, H Pfeifer, H Schafer, W Schmitz *Microporous Mesoporous Mater.* **22** 289 (1998)
139. W Heink, J Karger, G Seiffert, G Fleischer, J Rauchfuss *J. Magn. Reson. A* **114** 101 (1995)
140. I Furo, H Johannesson *J. Magn. Reson. A* **119** 15 (1996)
141. P T Callaghan, Y Xia *J. Magn. Reson.* **91** 326 (1991)
142. M H Blees *J. Magn. Reson. A* **109** 203 (1994)
143. L Z Wang, A Caprihan, E Fukushima *J. Magn. Reson. A* **117** 209 (1995)
144. P P Mitra, B I Halperin *J. Magn. Reson. A* **113** 94 (1995)
145. S J Gibbs, C S Johnson *J. Magn. Reson.* **93** 395 (1991)
146. G Wider, V Dotsch, K Wuthrich *J. Magn. Reson. A* **108** 255 (1994)
147. S J Gibbs, A Carpenter, L D Hall *J. Magn. Reson.* **98** 183 (1992)
148. W S Price, P Stilbs, B Jonsson, O Soderman *J. Magn. Reson.* **150** 49 (2001)
149. J G Seland, G H Sorland, K Zick, B Hafskjold *J. Magn. Reson.* **146** 14 (2000)
150. R M Cotts, M J R Hoch, T Sun, J T Markert *J. Magn. Reson.* **83** 252 (1989)
151. L L Latour, L Li, C H Sotak *J. Magn. Reson. B* **101** 72 (1993)
152. J Mattiello, P J Basser, D LeBihan *J. Magn. Reson. A* **108** 131 (1994)
153. P J Basser, J Mattiello, D LeBihan *J. Magn. Reson. B* **103** 247 (1994)
154. R I Shrager, P J Basser *Magn. Reson. Med.* **40** 160 (1998)
155. M D Hurlimann, K G Helmer, T M de Swiet, P N Sen, C H Sotak *J. Magn. Reson. A* **113** 260 (1995)
156. P Callaghan, D MacGowan, K J Packer, F O Zelaya *Magn. Reson. Imaging* **9** 663 (1991)
157. P T Callaghan, S L Codd, J D Seymour *Concepts Magn. Reson.* **11** 181 (1999)
158. O Soderman, B Jonsson *J. Magn. Reson. A* **117** 94 (1995)
159. Y Cheng, D Cory *J. Am. Chem. Soc.* **121** 7935 (1999)
160. M H G Amin, S J Gibbs, R J Chorley, K S Richards, T A Carpenter, L D Hall *Proc. R. Soc. London A* **453** 489 (1997)
161. P P Mitra, L L Latour, R L Kleinberg, C H Sotak *J. Magn. Reson. A* **114** 47 (1995)
162. T-Q Li, M Haggkvist, L Odberg *Langmuir* **13** 3570 (1997)
163. P T Callaghan, J Stepisnik *J. Magn. Reson. A* **117** 118 (1995)
164. D Xing, S J Gibbs, J A Derbyshire, E J Fordham, T A Carpenter, L D Hall *J. Magn. Reson. B* **106** 1 (1995)
165. K Raghavan, J C Park, G E Pavlovskaya, S J Gibbs *Magn. Reson. Imaging* **19** 697 (2001)
166. J Stepisnik *J. Magn. Reson.* **131** 339 (1998)
167. S P Rigby, L F Gladden *J. Catal.* **173** 484 (1998)
168. M J D Mallett, J H Strange *Appl. Magn. Reson.* **12** 193 (1997)
169. P Robyr, R Bowtell *J. Magn. Reson. A* **121** 206 (1996)
170. E Mischler, F Humbert, B Diter, D Canet *J. Magn. Reson. B* **106** 32 (1995)
171. K Woelk, R E Gerald II, R J Klinger, J W Rathke *J. Magn. Reson. A* **121** 74 (1996)
172. Y-Q Song *J. Magn. Reson.* **143** 397 (2000)

173. Y-Q Song *Magn. Reson. Imaging* **19** 417 (2001)
174. P D Majors, D M Smith, P J Davis *Chem. Eng. Sci.* **46** 3037 (1991)
175. F P Duval, P Porion, H Van Damme *J. Phys. Chem. B* **103** 5730 (1999)
176. A Klemm, H-P Muller, R Kimmich *Physica A* **266** 242 (1999)
177. N P Bidault, B E Hammer, A Hubel *Biotechnol. Prog.* **17** 530 (2001)
178. M Hagedorn, E W Hsu, U Pilatus, D E Wildt, W F Rall, S J Blackband *Proc. Natl. Acad. Sci. USA* **93** 7454 (1996)
179. H Van As, D van Dusschoten *Geoderma* **80** 389 (1997)
180. T Asakura, M Demura, H Ogawa, K Matsushita, M Imanari *Macromolecules* **24** 620 (1991)
181. Z Pearl, M Magaritz, P Bendel *J. Magn. Reson.* **95** 597 (1991)
182. U Tallarek, D van Dusschoten, H Van As, E Bayer, G Guiochon *J. Phys. Chem. B* **102** 3486 (1998)
183. M P Hollewand, L F Gladden *Chem. Eng. Sci.* **50** 309 (1995)
184. F Junker, W S Veeman *Chem. Phys. Lett.* **305** 39 (1999)
185. A Noda, K Hayamizu, M Watanabe *J. Phys. Chem. B* **105** 4603 (2001)
186. S Vasenkov, P Galvosas, O Geier, N Nestle, F Stallmach, J Karger *J. Magn. Reson.* **149** 228 (2001)
187. J J Tessier, K J Packer, J-F Thovert, P M Adler *AIChE J.* **43** 1653 (1997)
188. C F Jenner, Y Xia, C D Eccles, P T Callaghan *Nature (London)* **336** 399 (1988)
189. J H Gillard, N G Papadakis, K Martin, C J S Price, E A Warburton, N M Antoun, C L-H Huang, T A Carpenter, J D Pickard *Br. J. Radiol.* **74** 642 (2001)
190. M L Johns, K Hollingsworth, G M Davies, L F Gladden *Robust Characterisation of Flowing Emulsions Using Regularisation and Velocity-Compensating Pulsed Field Gradient (PFG)* (St Petersburg, Russia: NATO Advanced Studies Institute, 2001)
191. M L Johns, L F Gladden *J. Magn. Reson.* **154** 142 (2002)
192. P T Callaghan, A Coy, D MacGowan, K J Packer, F O Zelaya *Nature (London)* **351** 467 (1991)
193. P W Kuchel, A Coy, P Stilbs *Magn. Reson. Med.* **37** 637 (1997)
194. J E M Snaar, B P Hills *Magn. Reson. Imaging* **15** 983 (1997)
195. D van Dusschoten, C T W Moonen, P A de Jager, H Van As *Magn. Reson. Med.* **36** 907 (1996)
196. D van Dusschoten, P A de Jager, H Van As *J. Magn. Reson. A* **116** 22 (1995)
197. M Pfeffer, O Lutz *J. Magn. Reson. A* **113** 108 (1995)
198. I E Dimitrov, S R Charagundla, R Rizi, R Reddy, J S Leigh *Magn. Reson. Imaging* **17** 267 (1999)
199. D M Schmidt, J S George, S I Penttila, A Caprihan, E Fukushima *J. Magn. Reson.* **129** 184 (1997)
200. D M Gregory, R E Gerald II, R E Botto *J. Magn. Reson.* **131** 327 (1998)
201. M J Lizak, M S Conradi, C G Fry *J. Magn. Reson.* **95** 548 (1991)
202. R W Mair, D G Cory, S Peled, C-H Tseng, S Patz, R L Walsworth *J. Magn. Reson.* **135** 478 (1998)
203. H B Schwarz, H Ernst, S Ernst, J Karger, T Roser, R Q Snurr, J Weitkamp *Appl. Catal. A* **130** 227 (1995)
204. J Karger, W Heink *J. Magn. Reson.* **51** 1 (1983)
205. G H Sorland, D Aksnes, L Gjerdaker *J. Magn. Reson.* **137** 397 (1999)
206. S Vasenkov, W Bohlmann, P Galvosas, O Geier, H Liu, J Karger *J. Phys. Chem. B* **105** 5922 (2001)
207. J-L Bonardet, T Domeniconi, P N'Gokoli-Kekele, M-A Springuel-Huet, J Fraissard *Langmuir* **15** 5836 (1999)
208. U Hong, J Karger, H Pfeifer *J. Am. Chem. Soc.* **113** 4812 (1991)
209. U Hong, J Karger, B Hunger, N N Feoktistova, S P Zhdanov *J. Catal.* **137** 243 (1992)
210. R Q Snurr, A Hagen, H Ernst, H B Schwarz, S Ernst, J Weitkamp, J Karger *J. Catal.* **163** 130 (1996)
211. V Gupta, S S Nivarthi, A V McCormick, H T Davis *Chem. Phys. Lett.* **247** 596 (1995)
212. V Kukla, J Kornatowski, D Demuth, I Girnus, H Pfeifer, L V C Rees, S Schunk, K K Unger, J Karger *Science* **272** 702 (1996)
213. T Meersmann, J W Logan, R Simonutti, S Caldarelli, A Comotti, P Sozzani, L G Kaiser, A Pines *J. Phys. Chem. A* **104** 11665 (2000)
214. F Humbert, M Valtier, D Canet *Chem. Phys. Lett.* **302** 1 (1999)
215. D Barsky, B Putz, K Schulten, J Schoeniger, E W Hsu, S Blackband *Chem. Phys. Lett.* **200** 88 (1992)
216. J Stepisnik, A Duh, A Mohoric, I Sersa *J. Magn. Reson.* **137** 154 (1999)
217. L G Kaiser, J W Logan, T Meersmann, A Pines *J. Magn. Reson.* **149** 144 (2001)
218. Y-Q Song, B M Goodson, B Sheridan, T M de Swiet, A Pines *J. Chem. Phys.* **108** 6233 (1998)
219. B Saam, N Drukker, W Happer *Chem. Phys. Lett.* **263** 481 (1996)
220. B Putz, D Barsky, K Schulten *J. Magn. Reson.* **97** 27 (1992)
221. E Fukushima *Annu. Rev. Fluid Mech.* **31** 95 (1999)
222. J M Pope, S Yao *Concepts Magn. Reson.* **5** 281 (1993)
223. A Caprihan, E Fukushima *Phys. Rep.* **198** 195 (1990)
224. M Paley, R Hose, I Marzouqa, J Fenner, I Wilkinson, Y Noguchi, P Griffiths *Magn. Reson. Imaging* **18** 473 (2000)
225. *Chem. Eng. Sci. (Special Issue on Process Tomography)* **52** 13 (1997)
226. K W Moser, L G Raguin, A Harris, H D Morris, J Georgiadis, M Shannon, M Philpott *Magn. Reson. Imaging* **18** 199 (2000)
227. Y Xia, P T Callaghan *Magn. Reson. Med.* **23** 138 (1992)
228. D N Firmin, G L Nayler, P J Kilner, D B Longmore *Magn. Reson. Med.* **14** 230 (1990)
229. J Ding, R W Lyczkowski, W T Sha, S A Altobelli, E Fukushima *Powder Technol.* **77** 301 (1993)
230. C K Agemura, R J Kauten, K L McCarthy *J. Food Eng.* **25** 55 (1995)
231. C A Heath, G Belfort, B E Hammer, S D Mirer, J M Pimbley *AIChE J.* **36** 547 (1990)
232. Y Xia, P T Callaghan, K R Jeffrey *AIChE J.* **38** 1408 (1992)
233. K W Moser, J G Georgiadis, R O Buckius *Magn. Reson. Imaging* **18** 1115 (2000)
234. R Botnar, G Rappitsch, M B Scheidegger, D Liepsch, K Perktold, P Boesiger *J. Biomech.* **33** 137 (2000)
235. B R Locke, M Acton, S J Gibbs *Langmuir* **17** 6771 (2001)
236. A Franck, L-D Jou, R van Tyen, D Saloner *Magn. Reson. Imaging* **18** 1097 (2000)
237. A L Corbett, R J Philips, R J Kauten, K L McCarthy *J. Rheol.* **39** 907 (1995)
238. P T Callaghan, B Manz *J. Magn. Reson. A* **106** 260 (1994)
239. S J Weston, N B Wood, G Tabor, A D Gosman, D N Firmin *J. Magn. Reson. Imaging* **8** 1158 (1998)
240. M B Robertson, U Kohler, P R Hoskins, I Marshall *Magn. Reson. Imaging* **19** 685 (2001)
241. M J Graves *Br. J. Radiol.* **70** 6 (1997)
242. J R Singer *Science* **130** 1652 (1959)
243. J R Singer, L E Crooks *Science* **221** 654 (1983)
244. H M Gach, I J Lowe *Magn. Reson. Med.* **40** 559 (1998)
245. H G Bogren, R H Mohiaddin, P J Kilner, L J Jimenez-Borreguero, G Z Yang, D N Firmin *J. Magn. Reson. Imaging* **7** 784 (1997)
246. K S Nayak, J M Pauly, A B Kerr, B S Hu, D G Nishimura *Magn. Reson. Med.* **43** 251 (2000)
247. D N Firmin, G L Nayler, R H Klipstein, S R Underwood, R S Rees, D B Longmore *J. Comput. Assist. Tomogr.* **11** 751 (1987)
248. M F Walker, S P Souza, C P Dumoulin *J. Comput. Assist. Tomogr.* **12** 304 (1988)
249. K Ogawa, M Tobo, N Iriguchi, S Hirai, K Okazaki *Magn. Reson. Imaging* **18** 209 (2000)
250. M Tyszka, R C Hawkes, L D Hall *J. Magn. Reson.* **97** 391 (1992)
251. K Kose *J. Magn. Reson.* **98** 599 (1992)
252. U Gorke, R Kimmich, J Weis *J. Magn. Reson. B* **111** 236 (1996)
253. M Nakagawa, S A Altobelli, A Caprihan, E Fukushima, E-K Jeong *Exp. Fluids* **16** 54 (1993)
254. K Yamane, M Nakagawa, S A Altobelli, T Tanaka, Y Tsuji *Exp. Fluids* **10** 1419 (1993)
255. J Stepisnik *Prog. NMR Spectrosc.* **17** 187 (1985)
256. A Caprihan, S A Altobelli, E Benitez-Read *J. Magn. Reson.* **90** 71 (1990)
257. N J Pelc, R J Herfkens, A Shimakawa, D R Enzmann *Magn. Reson. Q* **7** 229 (1991)
258. P Moran *Magn. Reson. Imaging* **1** 197 (1982)
259. A Caprihan, M V Icenogle *Magn. Reson. Med.* **29** 512 (1993)
260. D F Arola, G Barrall, R L Powell, M J McCarthy *J. Magn. Reson. A* **123** 26 (1997)
261. D Bourgeois, M Decorps *J. Magn. Reson.* **94** 20 (1991)

262. A Jerschow *J. Magn. Reson.* **145** 125 (2000)
263. H M Gach, I J Lowe *Magn. Reson. Med.* **41** 1258 (1999)
264. J C Gatenby, J C Gore *J. Magn. Reson. A* **121** 193 (1996)
265. A Caprihan, J D Seymour *J. Magn. Reson.* **144** 96 (2000)
266. M V Icenogle, A Caprihan, E Fukushima *J. Magn. Reson.* **100** 376 (1992)
267. L Wigstrom, T Ebbers, A Fyrenius, M Karlsson, J Engvall, B Wranne, A F Bolger *Magn. Reson. Med.* **41** 793 (1999)
268. C L Dumoulin, H R Hart *Radiology* **161** 717 (1986)
269. H Bosmans, G Wilms, S Dymarkowski, G Marchal *Eur. J. Radiol.* **38** 2 (2001)
270. T W J Scheenen, D van Dusschoten, P A de Jager, H Van As *J. Magn. Reson.* **142** 207 (2000)
271. R A Damion, K J Packer, K S Sorbie, S R McDougall *Chem. Eng. Sci.* **55** 5981 (2000)
272. S-I Han, O Marseille, C Gehlen, B Blumich *J. Magn. Reson.* **152** 87 (2001)
273. P T Callaghan, W Kockenberger, J M Pope *J. Magn. Reson. B* **104** 183 (1994)
274. T W Redpath, D G Norris, R A Jones, J M S Hutchison *Phys. Med. Biol.* **29** 891 (1984)
275. D O Kuethe, J-H Gao *Phys. Rev. E* **51** 3252 (1995)
276. K Kose *J. Magn. Reson.* **96** 596 (1992)
277. J C Gatenby, J C Gore *J. Magn. Reson. A* **110** 26 (1994)
278. J C Gatenby, J C Gore *J. Magn. Reson. B* **104** 119 (1994)
279. J D Seymour, A Caprihan, S A Altobelli, E Fukushima *Phys. Rev. Lett.* **84** 266 (2000)
280. S-I Han, B Blümich *Appl. Magn. Reson.* **18** 101 (2000)
281. S-I Han, S Stapf, B Blümich *J. Magn. Reson.* **146** 169 (2000)
282. S A Riley, M P Augustine *J. Magn. Reson.* **144** 288 (2000)
283. S Stapf, R A Damion, K J Packer *J. Magn. Reson.* **137** 316 (1999)
284. B Blümich, P T Callaghan, R A Damion, S Han, A A Khrapitchev, K J Packer, S Stapf *J. Magn. Reson.* **152** 162 (2001)
285. A Haase, M Brandl, E Kuchenbrod, A Link *J. Magn. Reson. A* **105** 230 (1993)
286. S-I Han, P T Callaghan *J. Magn. Reson.* **148** 349 (2001)
287. S Laukemper-Ostendorf, H D Lemke, P Blümler, B Blümich *J. Membr. Sci.* **138** 287 (1998)
288. B Newling, S J Gibbs, L D Hall, D E Haycock, W J Frith, S Ablett *Chem. Eng. Sci.* **52** 2059 (1997)
289. A K Heibel, T W J Scheenen, J J Heiszwolf, H Van As, F Kapteijn, J A Moulijn *Chem. Eng. Sci.* **56** 5935 (2001)
290. C Heine, K Kupferschlager, S Stapf, B Blümich *J. Magn. Reson.* **154** 311 (2002)
291. T W J Scheenen, F J Vergeldt, C W Windt, P A de Jager, H Van As *J. Magn. Reson.* **151** 94 (2001)
292. C-M Tsai, E W Olcott, D G Nishimura *Magn. Reson. Med.* **42** 682 (1999)
293. J A Polzin, M T Alley, F R Korosec, T M Grist, Y Wang, C A Mistretta *J. Magn. Reson. Imaging* **5** 129 (1995)
294. N M Loening, J Keeler *J. Magn. Reson.* **139** 334 (1999)
295. S J Gibbs, T A Carpenter, L D Hall *J. Magn. Reson. A* **105** 209 (1993)
296. B Manz, J D Seymour, P T Callaghan *J. Magn. Reson.* **125** 153 (1997)
297. S-I Han, S Stapf, B Blümich *Phys. Rev. Lett.* **87** 144 501 (2001)
298. B Manz, P Stilbs, B Jonsson, O Soderman, P T Callaghan *J. Phys. Chem.* **99** 11 297 (1995)
299. K Y Chung, G Belfort, W A Edelstein, X Li *AIChE J.* **39** 1592 (1993)
300. K Kose *J. Magn. Reson.* **92** 631 (1991)
301. D P Madio, H M Gach, I J Lowe *Magn. Reson. Med.* **39** 574 (1998)
302. D O Kuethe *Phys. Rev. A* **40** 4542 (1989)
303. A D Hanlon, S J Gibbs, L D Hall, D E ;Haycock, W J Frith, S Ablett *Magn. Reson. Imaging* **16** 953 (1998)
304. J A Hopkins, R E Santini, J B Grutzner *J. Magn. Reson. A* **117** 150 (1995)
305. S Yao, A G Fane, J M Pope *Magn. Reson. Imaging* **15** 235 (1997)
306. D F Arola, G A Barrall, R L Powell, K L McCarthy, M J McCarthy *Chem. Eng. Sci.* **52** 2049 (1997)
307. Y Uludag, M J McCarthy, G A Barrall, R L Powell *Macromolecules* **34** 5520 (2001)
308. M M Britton, P T Callaghan, M L Kilfoil, R W Mair, K M Owens *Appl. Magn. Reson.* **15** 287 (1998)
309. P T Callaghan, U Fischer *Bruker Rep.* **149** 34 (2001)
310. L Jossic, A Briguet, A Magnin *Chem. Eng. Sci.* **57** 409 (2002)
311. S A Altobelli, E Fukushima, L A Mondy *J. Rheol.* **41** 1105 (1997)
312. T L Chenevert, A R Skovoroda, M O'Donnell, S Y Emelianov *Magn. Reson. Med.* **39** 482 (1998)
313. J Braun, G Buntkowsky, J Bernarding, T Tolxdorff, I Sack *Magn. Reson. Imaging* **19** 703 (2001)
314. R Muthupillai, D J Lomas, P J Rossman, J F Greenleaf, A Manduca, R L Ehman *Science* **269** 1854 (1995)
315. R Muthupillai, P J Rossman, D J Lomas, J F Greenleaf, S J Reiderer, R L Ehman *Magn. Reson. Med.* **36** 266 (1996)
316. C J Lewa, J D de Certaines *J. Magn. Reson. Imaging* **5** 242 (1995)
317. J Bishop, G Poole, M Leitch, D B Plewes *J. Magn. Reson. Imaging* **8** 1257 (1998)
318. J D Seymour, P T Callaghan *AIChE J.* **43** 2096 (1997)
319. R Kulkarni, A T Watson, J-E Nordtvedt *Magn. Reson. Imaging* **16** 707 (1998)
320. M D Mantle, A J Sederman, L Gladden *Chem. Eng. Sci.* **56** 523 (2001)
321. A J Sederman, M L Johns, A S Bramley, P Alexander, L F Gladden *Chem. Eng. Sci.* **52** 2239 (1997)
322. S Chen, F Qin, A T Watson *AIChE J.* **40** 1238 (1994)
323. S Chen, F Qin, K-H Kim, A T Watson *AIChE J.* **39** 925 (1993)
324. E J Fordham, L D Hall, T S Ramakrishnan, M R Sharpe, C Hall *AIChE J.* **39** 1431 (1993)
325. R A Waggoner, E Fukushima *Magn. Reson. Imaging* **14** 1085 (1996)
326. D N Guilfoyle, P Mansfield, K J Packer *J. Magn. Reson.* **97** 342 (1992)
327. J E M Snaar, H Van As *J. Magn. Reson.* **87** 132 (1990)
328. A Feinauer, S A Altobelli, E Fukushima *Magn. Reson. Imaging* **15** 479 (1997)
329. P Mansfield, B Issa *J. Magn. Reson. A* **122** 137 (1996)
330. M R Merrill *AIChE J.* **40** 1262 (1994)
331. H Van As, W Palstra, U Tallarek, D Van Dusschoten *Magn. Reson. Imaging* **16** 569 (1998)
332. T J Schaafsma, H Van As, W D Palstra, J E M Snaar, P A de Jager *Magn. Reson. Imaging* **10** 827 (1992)
333. K J Packer, J J Tessier *Mol. Phys.* **87** 267 (1996)
334. K J Packer, S Stapf, J J Tessier, R A Damion *Magn. Reson. Imaging* **16** 463 (1998)
335. D Candela, A Ding, X Yang *Physica B* **279** 120 (2000)
336. J Stepisnik, P T Callaghan *Physica B* **292** 296 (2000)
337. N C Irwin, S A Altobelli, R A Greenkorn *Magn. Reson. Imaging* **17** 909 (1999)
338. S Oswald, W Kinzelbach, A Greiner, G Brix *Geoderma* **80** 417 (1997)
339. Y E Kutsovsky, V Alvarado, H T Davis, L E Scriven, B E Hammer *Magn. Reson. Imaging* **14** 833 (1996)
340. M Ilg, J Maier-Rosenkranz, W Muller, K Albert, E Bayer, D Hopfel *J. Magn. Reson.* **96** 335 (1992)
341. U Tallarek, T W J Scheenen, H Van As *J. Phys. Chem. B* **105** 8591 (2001)
342. U Tallarek, D van Dusschoten, H Van As, G Guiochon, E Bayer *Magn. Reson. Imaging* **16** 699 (1998)
343. P Mansfield, M Bencsik *Magn. Reson. Imaging* **16** 451 (1998)
344. G Guillot, G Kassab, J P Hulin, P Rigord *J. Phys. D* **24** 763 (1991)
345. U Tallarek, D van Dusschoten, H Van As, G Guiochon, E Bayer *Angew. Chem., Int. Ed.* **37** 1882 (1998)
346. U Tallarek, F J Vergeldt, H Van As *J. Phys. Chem. B* **103** 7654 (1999)
347. S Stapf, K J Packer *Appl. Magn. Reson.* **15** 303 (1998)
348. E J Fordham, M A Horsfield, L D Hall, G C Maitland *J. Colloid Interface Sci.* **156** 253 (1993)
349. E J Fordham, T P L Roberts, T A Carpenter, L D Hall, C Hall *AIChE J.* **37** 1900 (1991)
350. E J Fordham, A Sezginer, L D Hall *J. Magn. Reson. A* **113** 139 (1995)
351. M A Horsfield, E J Fordham, C Hall, L D Hall *J. Magn. Reson.* **81** 593 (1989)
352. J J Dechter, R A Komoroski, S Ramaprasad *J. Magn. Reson.* **93** 142 (1991)

353. P D Majors, J L Smith, F S Kovarik, E Fukushima *J. Magn. Reson.* **89** 470 (1990)
354. S S Mandava, A T Watson, C M Edwards *AIChE J.* **36** 1680 (1990)
355. J-D Chen, M M Dias, S Patz, L M Schwartz *Phys. Rev. Lett.* **61** 1489 (1988)
356. A T Watson, R Kulkarni, J-E Nordtvedt, A Sylte, H Urkedal *Meas. Sci. Technol.* **9** 898 (1998)
357. J J Tessier, K J Packer *Phys. Fluids* **10** 75 (1998)
358. C A Baldwin, L F Gladden *AIChE J.* **42** 1341 (1996)
359. M L Johns, L F Gladden *J. Colloid Interface Sci.* **210** 261 (1999)
360. A J Sederman, L F Gladden *Chem. Eng. Sci.* **56** 2615 (2001)
361. E Bayer, W Muller, M Ilg, K Albert *Angew. Chem., Int. Ed. Engl.* **28** 1029 (1989)
362. L D Hall, R Vasanthan *J. Chem. Soc., Chem. Commun.* 499 (1985)
363. M Nakagawa, S A Altobelli, A Caprihan, E Fukushima *Chem. Eng. Sci.* **52** 4423 (1997)
364. G Metcalf, M Shattuck *Physica A* **233** 709 (1996)
365. A Caprihan, E Fukushima, A D Rosato, M Kos *Rev. Sci. Instrum.* **68** 4217 (1997)
366. E E Ehrichs, H M Jaeger, G S Karczmar, J B Knight, V Yu Kuperman, S R Nagel *Science* **267** 1632 (1995)
367. I V Koptyug, S A Altobelli, E Fukushima, A V Matveev, R Z Sagdeev *J. Magn. Reson.* **147** 36 (2000)
368. E Brunner, M Haake, L Kaiser, A Pines, J A Reimer *J. Magn. Reson.* **138** 155 (1999)
369. W Happer, E Miron, S Schaefer, D Schreiber, W A van Wijngaarden, X Zeng *Phys. Rev. A* **29** 3092 (1984)
370. Y-Q Song, H C Gaede, T Pietrass, G A Barrall, G C Chingas, G C Ayers, A Pines *J. Magn. Reson. A* **115** 127 (1995)
371. M S Albert, G D Cates, B Driehuys, W Happer, B Saam, C S Springer, A Wishnia *Nature (London)* **370** 199 (1994)
372. M S Albert, D Balamore *Nucl. Instrum. Methods Phys. Res. A* **402** 441 (1998)
373. M Bencsik, C Ramanathan *Magn. Reson. Imaging* **19** 379 (2001)

[a] — *Chem. Phys. Rep. (Engl. Transl.)*
[b] — *Russ. J. Struct. Chem. (Engl. Transl.)*
[c] — *Russ. J. Phys. Chem. (Engl. Transl.)*
[d] — *Dokl. Chem. (Engl. Transl.)*